Charles University

Faculty of Science

Study program: Physical chemistry

Branch of study: Physical chemistry

Bc. Petr Golis

Study of active centers in zeolite catalysts for cascade Prins-Friedel-Crafts reaction

Studium aktivních center v zeolitových katalyzátorech
pro kaskádovou Prins-Friedel-Craftsovu reakci

Diploma thesis

Supervisor: Mariya Shamzhy, Ph.D.

Prague, 2022

Prohlášení

Prohlašuji, že jsem závěrečnou práci zpracoval/a samostatně a že jsem uvedl/a všechny použité informační zdroje a literaturu. Tato práce ani její podstatná část nebyla předložena k získání jiného nebo stejného akademického titulu.

V Praze dne:

Bc. Petr Golis

Podpis:

Acknowledgement

I express my gratitude to my supervisor Mariya Shamzhy, Ph.D., for her patience, guidance, and countless advice during my research. Likewise, I am grateful to my advisor, Maksym Opanasenko, Ph.D. and to Prof. Ing. Jiří Čejka, DrSc. for their valuable advice and useful instructions. I also thank all my colleagues for their help with different measurements and laboratory work, namely Ing. Martin Kubů, Ph.D. (nitrogen physisorption, ICP), Michal Mazur, Ph.D., and Ang Li, MSc. (electron microscopy), Yuyan Zhang, Ph.D. (synthesis). Also, I am grateful to Roman Barakov, Ph.D., Mgr. Kinga Maria Golabek, Ph.D., Ing. Jan Přech, Ph.D., Mgr. Ondřej Veselý, and Mgr. Milan Eliáš for their general advice for laboratory work. This work would not be possible without the people mentioned here, so once again, I want to thank everyone mentioned here.

Abstract

Conventional zeolites are important shape-selective heterogeneous acid catalysts due to the presence of acid sites accessible through uniform micropores. Recently designed hierarchical zeolites with combined micro-mesoporosity also contain acid sites on the external surface or in mesopores. These highly accessible acid sites are promising active centres for the transformation of bulky molecules, which cannot pass through the micropore openings of conventional zeolites. An example of a reaction that can benefit from the use of zeolites is the one-pot cascade Prins-Friedel-Crafts (PFC) reaction of an aldehyde, homoallylic alcohol, and aromatic compound, which yields valuable heterocyclic compounds containing 4-aryltetrahydropyran moieties.

In this work, the acidic characteristics of a series of hierarchical aluminium- and gallium-containing **MFI** and **MWW** zeolites were evaluated by FTIR-monitored thermodesorption of probe molecules and further related to the catalytic properties of zeolites in the PFC reaction of butyraldehyde, 3-buten-1-ol, and anisole.

The nature, strength, and total concentration of acid sites in the catalysts were evaluated using thermodesorption of pyridine (kinetic diameter 0.54 nm), while the characteristics of the external surface Brønsted acid sites were probed using 2,6-di-tertbutylpyridine (kinetic diameter 0.79 nm). The results revealed the crucial role of the strength of acid sites and their distribution between the internal and external surfaces of the crystals, as well as the important impact of zeolite structure on the butyraldehyde conversion and selectivity toward targeted products of the PFC reaction. Among the catalysts investigated, Al-containing **MWW** zeolites with high total concentration of acid sites (0.41 mmol/g), remarkable fraction of strong acid centers (66%) and notable fraction of highly accessible external acid sites showed the highest values of butyraldehyde conversion (90% after 24 h) and selectivity toward the targeted products of the PFC reaction (37% at 50% conversion).

Keywords: heterogeneous catalysis, zeolites, Prins-Friedel-Crafts reaction

Abstrakt

Konvenční zeolity jsou důležité tvarově selektivní heterogenní katalyzátory díky přítomnosti jejich kyselých center, která jsou přístupná skrze stejnoměrné mikropóry. Nově navržené hierarchické zeolity kombinující mikro a mezoporozitu obsahují tyto centra kyselosti také na svém vnějším povrchu, nebo v mezopórech. Tyto vysoce přístupná centra kyselosti se jeví jako slibná aktivní centra pro transformaci rozměrnějších molekul, která nejsou schopna vstoupit do mikropórů konvenčních zeolitů. Jako příklad reakce, pro kterou by použití zeolitů bylo prospěšné, je kaskádová Prins-Friedel-Craftsova reakce aldehydu, homoallylického alkoholu, a aromatické sloučeniny, která vede k cenným heterocyklickým sloučeninám obsahující 4-aryl tetrahydopyranovou skupinu.

Tato práce se zabývá analýzou kyselých vlastností série hierarchických **MFI** a **MWW** zeolitů obsahujících hliník, nebo galium metodou FTIR analyzované desorpce adsorbovaných molekul. Tyto vlastnosti byly následně uvedeny do souvislostí s katalytickými vlastnostmi těchto zeolitů v PFC reakci butyraldehydu, 3-buten-1-olu, a anisolu.

Typ, síla, a celková koncentrace kyselých center studovaných katalyzátorů byla vyhodnocena termodesorpcí pyridinu (kinetický průměr 0.54 nm), zatímco vlastnosti Brønstedových center kyselosti na vnějším povrchu byly vyhodnoceny termodesorpcí 2,6-di-tert-butylpyridinu (kinetický průměr 0.79 nm). Výsledky experimentů odhalily důležitost síly kyselých center, distribuce kyselých center mezi vnějším a vnitřním povrchem krystalů zeolitu, a také účinek struktury zeolitu na konverzi butyraldehydu a na selektivitu vůči cílovým produktům PFC reakce. Ze všech zkoumaných zeolitů, MWW zeolit s hliníkem s vysokou koncentrací kyselých center (0.41 mmol/g), s vysokým poměrem silných kyselých center (66%) a s také s vysokým poměrem velmi přístupných kyselých center na vnějším povrchu, dosahoval nejvyšších hodnot konverze butyraldehydu (90% za 24 hodin) a také nejvyšší selektivity vůči cílovým produktům (37% při 50% konverzi).

Klíčová slova: heterogenní katalýza, zeolity, Prins-Friedel-Craftsova reakce

Table of contents

1. Introduction 1

2. Theoretical Part 3

2.1. Zeolites 3
2.1.1. History 3
2.1.2. Structure and properties 3
2.1.3. Synthesis and post-synthesis of conventional and hierarchical zeolites 7
2.1.3.1. MFI 9
2.1.3.2. MWW 11

2.2. Methods for characterization and evaluation of zeolites 13
2.2.1. X-ray diffraction (XRD) 13
2.2.2. Gas physisorption 15
2.2.3. Electron microscopy 17
2.2.4. Optical emission spectroscopy (ICP-OES) 19
2.2.5. IR spectroscopy 20
2.2.5.1. Framework structure and composition 22
2.2.5.2. Concentration, strength, nature, and accessibility of acid sites 23
2.2.6. Gas Chromatography 25

2.3. Prins-Friedel-Crafts (PFC) reaction 26

3. Experimental part 29

3.1. List of Chemicals 29

3.2. Synthesis of MWW zeolites 29

3.3. Synthesis of MFI zeolites 30

3.4. Characterization of zeolite catalysts 31

3.5. FTIR experiment 32

3.6. Catalytic experiment 34

4. Results and discussion 36

4.1. Characteristics of MFI and MWW zeolites 36
4.1.1. Structural and textural properties 36
4.1.2. Acidic properties 43

4.2. Properties-function relationships of zeolite catalysts in the PFC reaction 51
4.2.1. The effect of the nature of acid sites 54
4.2.2. The effect of the chemical compositions 55
4.2.3. The effect of textural properties 56
4.2.4. The effect of the zeolite framework structure 57
4.2.5. Catalytic activity of zeolite catalysts in the PFC reaction 58

5. Conclusions 60

6. References 62

List of abbreviations

ADOR - assembly-disassembly-organisation-reassembly

AET - zeolite framework with 1-dimensional 14-ring pore channel system

AFI - zeolite framework with 1-dimensional 12-ring pore channel system

ALD - aldehyde

ArC - aromatic compound

BAS - Brønsted acid sites

BEA - zeolite framework with 3-dimensional 12-12-12-ring pore channel system

BET - Brunauer, Emmett and Teller theory

BSE - backscattered electrons

CAS - zeolite framework with 1-dimensional 8-ring pore channel system

c_B - concentration of Brønsted acid sites

CHA - zeolite framework with 3-dimensional 8-8-8-ring pore channel system

c_L - concentration of Lewis acid sites

CTAB - cetyltrimethylammonium bromide

DPE - deprotonation energy

DTBP - 2,6-di-tert-butylpyridine

$DTBP^+$ - cation of 2,6-di-tert-butylpyridine

DTGS - deuterated triglycine sulfate

Et_3N^+ - triethanolamine cation

FAU - zeolite framework with 3-dimensional 12-12-12-ring pore channel system

FID - flame ionization detector

FTIR - Fourier-transform infrared spectroscopy

GC - gas chromatography

HA - homoallylic alcohol

HMI - hexamethyleneimine

ICP-OES - inductively coupled plasma optical emission spectrometer

IR - infrared spectroscopy

ITV - zeolite framework with 3-dimensional 30-30-30-ring pore channel system

IZA - International Zeolite Association

LAS - Lewis acid sites

MC - microcrystalline

MCM-22 - Mobil catalytic material, three dimensional **MWW** zeolite

MCM-22P - Mobil catalytic material layered precursor of **MWW** zeolite

MCM-36 - Mobil catalytic material, pillared **MWW** zeolite

MCM-49 - Mobil catalytic material, three dimensional **MWW** zeolite

MCM-56 - Mobil catalytic material, disordered nanolayered **MWW** zeolite

Me_3N^+ - trimethylamine cation

MEL - zeolite framework with 3-dimensional 10-10-10-ring pore channel system

Meso - mesoporous zeolite

MFI - zeolite framework with 3-dimensional 10-10-10-ring pore channel system

MOR - zeolite framework with 2-dimensional 12-8-ring pore channel system

MWW - zeolite framework with 3-dimensional 10-10-10-ring pore channel system and 12-ring external cups

NL - nanolayered

NS - nanosponge

PFC - Prins-Friedel-Crafts

PI - pillared

Pr_3N^+ - tripropylamine cation

SDA - structure directing agent

SE - secondary electrons

SEM - scanning electron microscopy

S_{ext} - external surface

Si/Al - silicon to aluminium molar ration

Si/Ga - silicon to gallium molar ration

Si/T - silicon to T atom molar ration

Si/Ti - silicon to titanium molar ration

TEM - transmission electron microscopy

TEOS - tetraethyl orthosilicate

TPAOH - tetrapropylammonium hydroxide

TS-1 - titanosilicate zeolite with **MFI** structure

UTL - zeolite framework with 2-dimensional 14-12-ring pore channel system

V_{meso} - volume of mesopores

V_{mic} - volume of micropores

XRD - X-ray diffraction

ZSM-5 - Zeolite Socony Mobil-5, **MFI** zeolite

ν(OH) - stretching frequency of O-H bond

1D - one-dimensional

2D - two-dimensional

3D - three-dimensional

1. Introduction

Zeolites are defined as microporous crystalline aluminosilicates and they serve as important acid heterogeneous catalysts in today's industry due to their adsorption and exceptional catalytic properties, combined with environmental friendliness, tuneable acidity, and their thermal and chemical stability. In modern industry, conventional zeolites are predominantly used in crude oil upgrading and petrochemistry for their shape selectivity. Recently, the focus of zeolite science was changed towards enhancement of accessibility of active sites by designing zeolites with hierarchical porosity and improved diffusion characteristics. Hierarchical zeolites with high accessibility to acid centres can be used to catalyse chemical reactions involving bulky reagents or providing bulky products, while ensuring shape selectivity to influence the reaction pathway.

There are many reactions that use homogeneous acid catalysts, although such catalysts are often toxic, costly, and inconvenient for cyclic utilization. An introduction of zeolites as heterogeneous catalysts reduces the use of environmentally unfriendly materials, while providing shape-selective properties unattainable for homogeneous catalysts. An example of a reaction that can benefit from the use of zeolites is the one-pot three-component cascade acid catalysed Prins-Friedel-Crafts (PFC) reaction. The PFC reaction is an effective method for the synthesis of 4-aryltetrahydropyran moiety containing heterocycles, which act as a basis for biologically active compounds, such as polyether antibiotics, pheromones, and various pharmaceutical agents. Because the PFC reaction produces bulky products, conventional zeolites that possess exclusively micropores may fail in catalysing this cascade process. In turn, hierarchical zeolites containing either intracrystalline mesopores or advanced external surfaces are more promising catalysts for such reaction. However, the effects of external acid site features and properties-function relationships for different classes of hierarchical zeolites are not yet fully understood.

This master thesis aims at understanding and rationalization of the acid sites features (i.e., strength, nature, location) that are decisive for the catalytic activity and selectivity of advanced hierarchical zeolite materials in a one-pot three-component cascade Prins–Friedel–Crafts reaction of butyraldehyde, 3-buten-1-ol and anisole.

The main objectives of the master thesis are:

- to synthesize and comprehensively characterize Al- and Ga-substituted conventional and hierarchical zeolites having the same topology but different textural properties and crystal morphology;
- to probe the nature, strength and distribution of internal and external surface acid sites in **MWW** and **MFI** zeolites of different chemical composition using adsorption of pyridine and 2,6-ditertbutyl pyridine monitored by FTIR spectroscopy;
- to assess activity and selectivity of designed zeolite catalysts in a one-pot three-component cascade Prins–Friedel–Crafts reaction of butyraldehyde, 3-buten-1-ol, and anisole.

2. Theoretical Part

2.1. Zeolites

2.1.1. History

Zeolites were first described as specific minerals in 1756 by a Swedish mineralogist, Axel Fredrik Cronstedt.[1] However, zeolites were successfully utilized by mankind long before Cronstedt recognized them as a mineralogical species. For example, the construction of pyramids and temples in Mexico implied using zeolites as dimension stones, while the Romans used zeolites to produce pozzolanic cement.[2] The name "zeolites" was derived from the Greek words "Zeo" and "Lithos", which can be translated as "stones that boil" (a reference to their hydrating and dehydrating properties).[3] The first natural zeolite discovered by A.F. Cronstedt was stilbite and the family of known natural zeolites currently includes 67 members.[4] The intensive investigation of the physical, chemical and mineralogical characteristics of natural zeolites and the emergence of zeolite science as a specific field of research are related to the pioneering studies by R.M. Barrer on structural and textural properties of zeolites (discussed in Section 2.1.2) and the crystallization conditions of synthetic zeolites (discussed in Section 2.1.3) in the 1930s. In the 1950s, the first convincing scientific interpretations became available for the explanation of acidity in zeolites. Zeolites have also gained attention as catalysts for petroleum refining, which is their main use in the industry today (see Section 2.4). In the 1960s, Mobil Oil developed and commercialized faujasite (**FAU**), and mordenite (**MOR**) zeolites for catalytic application. Then, in the 1970s, zeolite ZSM-5 (**MFI**) followed as another Mobil's discovery. Since then, many more new zeolite frameworks have been discovered and assigned with a unique three-letter code by the International Zeolite Association, which approved 255 structural types of zeolites up to now.[5] Nowadays, the zeolite science is focused on the design, characterization and application of zeolites with non-typical crystal morphologies (nanocrystalline, 2D zeolites) and chemical composition beyond aluminosilicates.[6]

2.1.2. Structure and properties

Molecular sieves are especially important materials for modern heterogeneous catalysis. Molecular sieves can be defined as any material, crystalline or amorphous, that is composed of a pore system with pore diameter comparable to kinetic diameters of molecules. Zeolites belong to the group of crystalline metallosilicate molecular sieves (conventionally, aluminosilicates) with periodically ordered micropores.[7]

Conventional zeolite has a 3D structure composed of interlinked TO_4 tetrahedra, with framework-building T-elements coordinated by four oxygen atoms. Natural zeolites are defined as aluminosilicates composed of corner-sharing SiO_4 and AlO_4^- tetrahedra, while synthetic zeolites have variable chemical compositions, where the T atom can also be Ga, Ti, Ge, Sn, Zr and others. The TO_4 tetrahedra serve as the primary building units of a zeolite framework, which connect by sharing an oxygen atom to form the so-called secondary building units. The final zeolite framework is then formed by connecting these secondary building units (Figure 1). The framework obeys the Löwenstein rule, which means that two Al T atoms cannot be connected through an oxygen bridge. The Löwenstein rule limits the maximum Al concentration in a zeolite material to the Si/Al ratio of 1:1.[7]

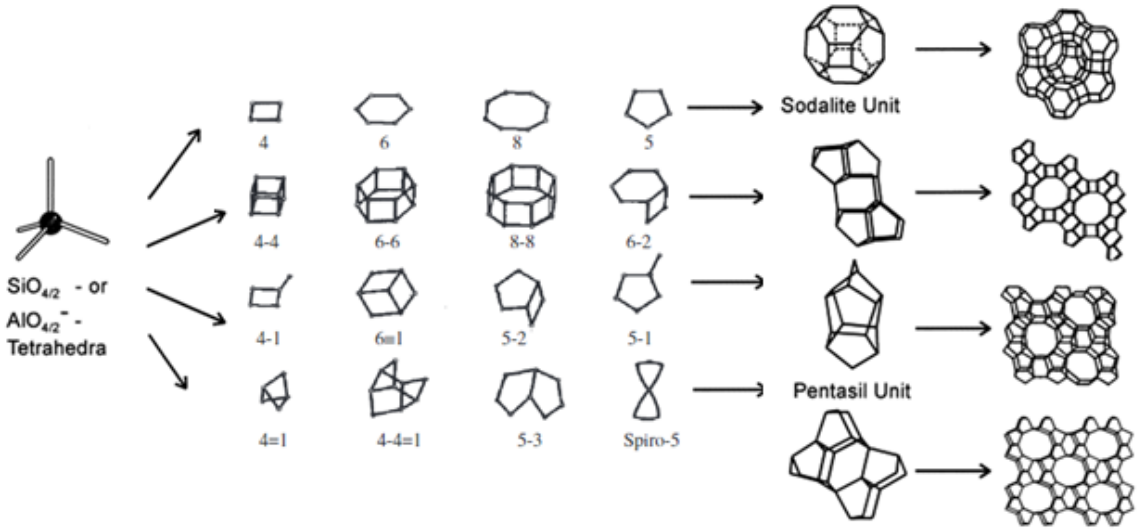

Figure 1: From left to right, a single tetrahedron, tetrahedra combined into primary building blocks, primary building blocks combined to form secondary building blocks, and zeolite structure forms from secondary building blocks. Adapted from Ref. [7-8]

One of the ways to classify zeolites is by the size of their pores, where the pore size is defined by the amount of tetrahedra (or T atoms) limiting the channel entrance. For zeolites, the number of pore ring T atoms ranges from 3 to 30.[5] Zeolites with 8-ring channels are referred to as small-pore zeolites with a pore diameter of up to 0.4 nm (e.g., **CHA**, **CAS**). Zeolites with 10-ring channels are referred to as medium-pore zeolites with pore diameter of up to 0.55 nm (e.g., **MFI**, **MWW**). Zeolites with 12-ring channels are referred to as large-pore zeolites with pore diameter of up to 0.7 nm (e.g., **MOR**, **BEA**), and zeolites with more than 12 T-atoms in the pore ring are referred to as extra-large pore zeolites (e.g., **UTL**, **AET**) with pore dimensions greater than 0.7 nm.[9] The highest reported number of T atoms in the pore ring is 30 in the **ITV** framework.[10] The size of pore rings formed by 3-7 tetrahedra is too

small for the adsorption/diffusion of a molecule. For this reason, such pores are excluded for this classification.

In addition to the pore size, the pore dimensionality is another important feature of the zeolite framework. Zeolites can have a 1D, 2D, or 3D pore channel system. 1D pore channel systems contain no intersections of their channels (e.g., **AFI**, **MTW**). 2D pore channel systems intersect in two dimensions (e.g., **MWW**, **UTL**), and finally, 3D pore channel systems contain intersections in three dimensions (e.g., **MFI**, **CHA**).

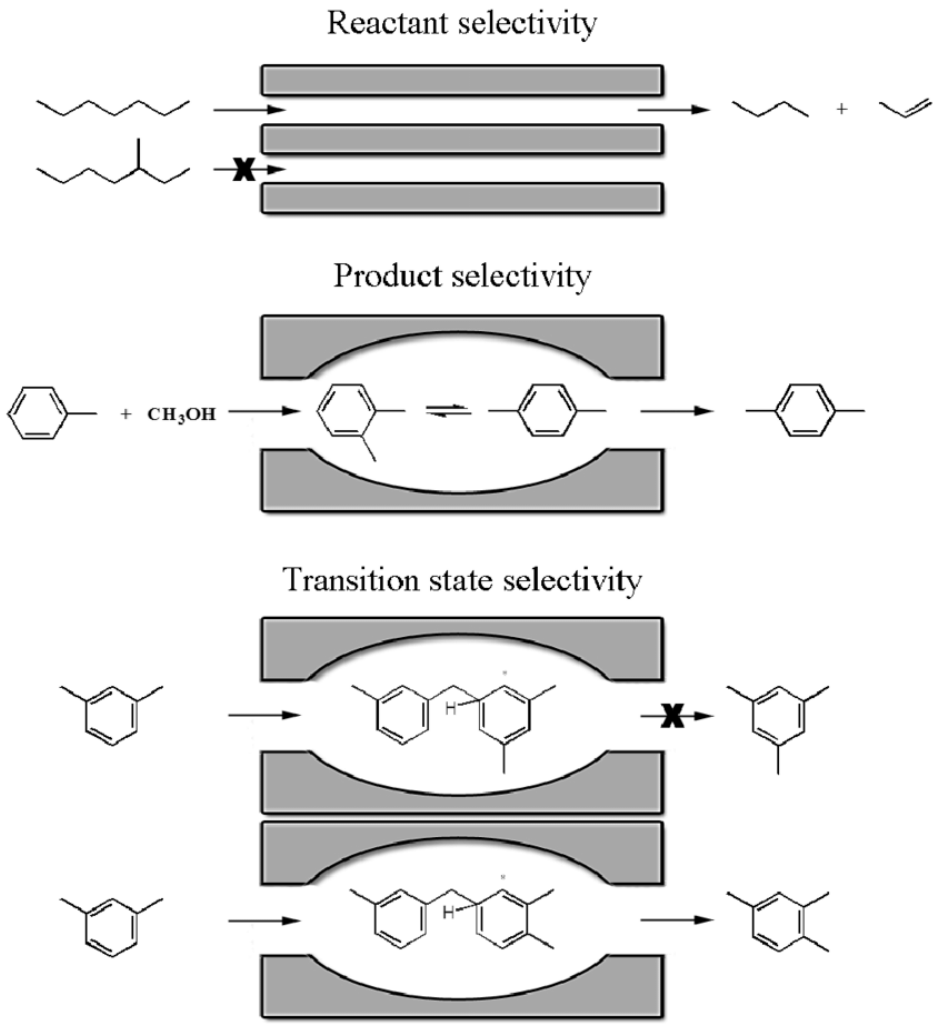

Figure 2: Different types of zeolites shape selectivity. Adapted from Ref.[11]

The diameter of the uniform pores and the pore systems dimensionality determine the performance of a zeolite as a shape selective catalyst (Figure 2).[3] Shape selectivity is the ability of a zeolite to discriminate against different molecules with different size or shape. This property manifests itself thank to the micropore sizes of zeolites being on the same scale as those of small organic molecules. Shape selectivity is a concept that was first revealed in the 1960s. Three types of shape selectivity were introduced at the time: reactant, product, and

transition state selectivity. The type of shape selectivity depends on the severity of steric restrictions on each species.

The silicon T atoms in a zeolite framework can be substituted by another element *via* isomorphous substitution, such as aluminium, gallium, germanium, or titanium. Aluminium has a lower oxidation number than silicon (Si^{4+}, Al^{3+}), and since the basic building block is a tetrahedron and the T atom is connected to four oxygen atoms, the introduction of a trivalent atom creates a negative charge in the framework. This negative charge needs to be compensated for by an extra-framework cation, for example, some alkaline earth metal, an alkali metal, quaternary ammonium, or a proton. In the case of the proton, a bridging hydroxyl group is formed, which is a Brønsted acid site (BAS, Figure 3). The introduction of a trivalent atom into the framework can also cause defects in the structure, which can result in an aluminium atom neighbouring only three oxygens instead of four. This aluminium atom has a free orbital which may accept the electron pair from the reactant, thus acting as a Lewis acid site (LAS, Figure 3). LASs are also formed by the introduction of different tetravalent atoms (e.g., Ti^{4+}, Sn^{4+}) into the framework. Being placed in the framework T-positions of zeolites, these coordinatively unsaturated metals bear free orbitals which accept an electron pair from reactants without inducing a charge imbalance in the framework and then activate substrates with electron rich groups.[12]

The aluminium content has a profound influence on the properties of the zeolites. Both BAS and LAS act as catalytically active centres in acid-catalysed reactions. The presence of the charge in the framework also gives zeolites their ion exchange capacity and tuneable hydrophilicity, which depend on the aluminium content. According to their aluminium content, zeolites can be classified into low-silica zeolites (Si/Al > 2), intermediate-silica zeolites (Si/Al = 2 – 10), and high-silica zeolites (Si/Al > 10).[13] With increasing silicon content, the structure becomes more thermally stable and hydrophobic, while the number of acid sites decreases, because silicon does not create the negative charge in the framework.[14] By substituting Al in the zeolite framework with other trivalent elements, one may vary the strength of acid centres. The deprotonation energy (DPE) is used for evaluation of the acid strength of the protonic sites. The increase in DPE suggested the decrease of the BAS strength in the sequence Al > Ga > B.[15] Thus, the acidic properties of zeolites can be changed by the variation of their Si/T ratio during synthesis and the introduction of a different heteroatom.

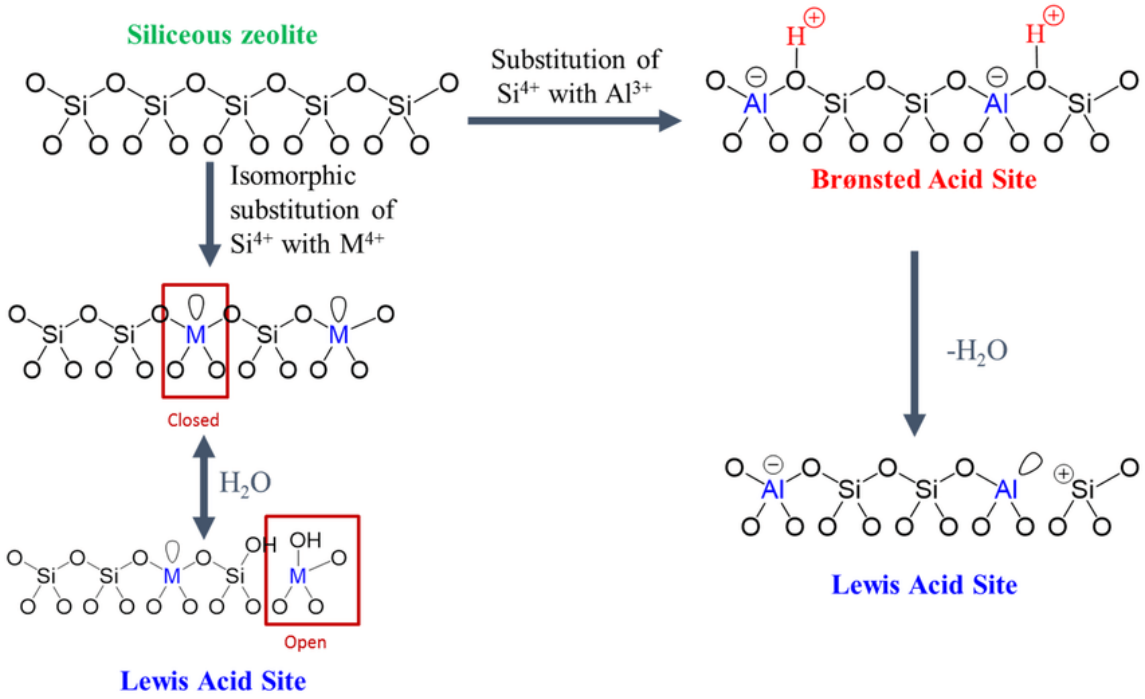

Figure 3: BAS and LAS generated by isomorphous substitution in zeolites. Adapted from Ref.[16]

2.1.3. Synthesis and post-synthesis of conventional and hierarchical zeolites

A typical way of synthesizing zeolites is crystallization from gels composed of water, the source of T atoms, mineralizing and a structure-directing agents (SDA) under hydrothermal conditions (usually at T = 80 – 200 °C and autogenous pressure). The ratio between framework-building elements (e.g., the Si/Al ratio) is one of the key parameters of the synthesis, since it determines the structure and chemical composition of a synthesized zeolite and influences the kinetics of the crystallization process. Water solubilizes the Si and Al precursors and serves as a medium for the transport of reacting species. The presence of a mineralization agent, such as OH^- or F^- promotes the formation of Si-O-Si and Si-O-Al bonds through condensation reactions. The stirring of the gel also has a strong influence on the crystallization of zeolite. An increase in the stirring rate leads to the formation of smaller crystals with a more narrow size distribution.[3] Different amines and quaternary ammonium cations (e.g., Me_3N^+, Et_3N^+, Pr_3N^+ or *N,N,N*-trimethyladamantammonium[17]) are used as a SDA in crystallization of zeolites.

Conventional zeolites with microporous channel systems synthesized in this way revolutionized the chemical industry by advancing different industrial processes, for example, fluid catalytic cracking, hydrocracking, naphtha reforming, upgrading of diesel fractions, and methanol to olefins and methanol to gasoline processes.[18] Most of acid sites in conventional

zeolites, however, are accessible only for the molecules with small enough kinetic diameter to fit into the micropores. Therefore, conventional zeolites do not favour the conversion or the formation of molecules with kinetic diameter > 1 nm due to their reagent/product/transition state shape selectivity. To produce zeolite catalysts for the transformation of bulkier molecules, new synthesis protocols and post-synthesis treatments were developed. This resulted in advanced zeolite materials with hierarchical micro-meso- or micro-macroporosity and highly accessible acid sites, such as mesoporous **MFI** with intracrystalline transport pores, 2D **MFI** with nanocrystals of lamellar shape or nanosponge **MFI** with randomly connected crystalline nanolayers both featuring intercrystalline mesoporosity (Figure 4).[3]

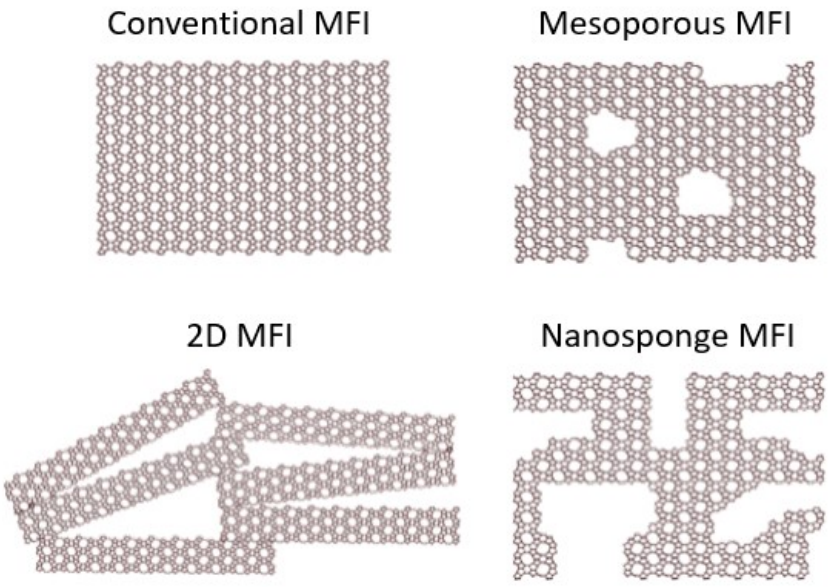

Figure 4: Model of conventional, mesoporous, 2D, and nanosponge **MFI** zeolites.

The most general and versatile approach for generating intracrystalline mesopores is the use of different types of porous carbon resins, organic aerogels, polymers as templates.[19] Non-templating methods include demetallation and controlled crystallization. Demetallation is performed by extracting framework atoms (such as Al or Si) from a prepared zeolite by steaming or acid leaching treatment, which introduces intracrystalline mesoporosity into the structure.[19] The controlled crystallization method is based on regulating the crystallization conditions to favour nucleation over crystal growth. It is a development of modified synthesis methods that leads to a decrease in the crystal size, for example by using growth inhibitors, by increasing supersaturation, or by quenched crystallization.[19] As a result, zeolite materials with intercrystalline mesoporosity are formed.

2D zeolites form a specific class of zeolites with an enhanced external surface and more accessible acid sites. Zeolite is considered 2D if one of its crystal dimensions is just a

few nanometres in length, which is about one- or two-unit cells. 2D zeolites feature inter-crystalline mesopores and contain a higher amount of accessible acid sites located on external surface per mass/volume than conventional 3D zeolites, which possess micrometre-sized crystals. This enhanced accessibility of external surface acid sites makes 2D zeolites advantageous for catalytic transformations of bulky molecules.[3] In addition, it is also possible to make some post-synthesis modifications for layer manipulation, such as swelling, pillaring and exfoliation, which will be discussed in detail *vide infra* when considering **MWW** zeolite. 2D zeolites can be synthesized using three different synthesis approaches. First, a few zeolites, such as **MWW**, were found to crystallize as lamellar precursors from conventional reaction mixtures, discussed *vide supra*. The second approach is the use of a specifically designed SDA containing a polyquaternary ammonium part and a long hydrophobic tail (e.g., $C_nH_{2n+1}–(N^+(R)_2–C_6H_{12})_m–N^+(CH_3)_2–\ C_nH_{2n+1}$ (n = 18, 22; m = 2; 3)) during synthesis to restrict crystal growth in one crystallographic dimension.[20] And the third method is a top-down modification of zeolites structure, such as ADOR[21] (assembly, disassembly, organization, reassembly), based on the possibility to selectively remove Ge atoms from germanosilicate zeolites, such as **UTL** (Figure 5).[3, 20]

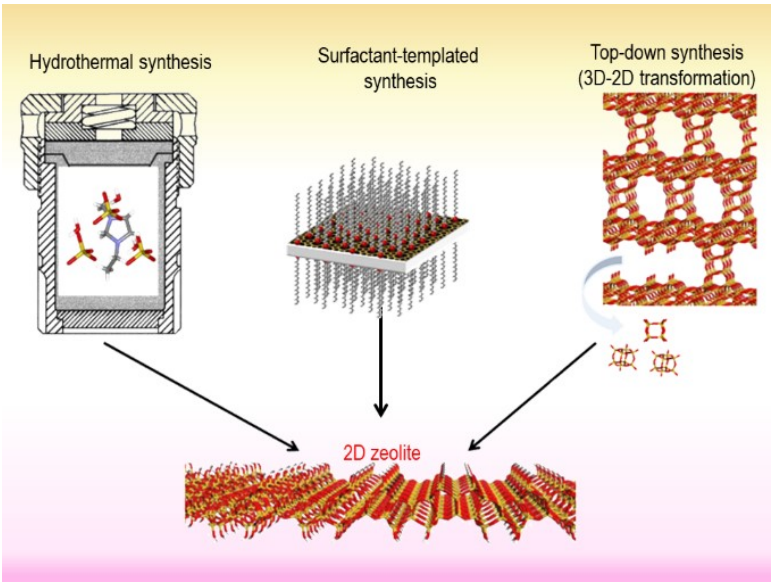

Figure 5: Approaches for synthesizing 2D zeolites. Reprinted from Ref.[20]

2.1.3.1. MFI

Zeolites with **MFI** structure are particularly important from an industrial point of view. This framework was discovered by Mobil in the 1970s in an aluminosilicate form named ZSM-5. ZSM-5 is used in petrochemistry, while **MFI** in titanosilicate form (TS-1) is used for oxidative reactions.[6] The **MFI** zeolite with 10-ring channels naturally offers different

selectivity, when used as additive in the fluid catalytic cracking, than the primary cracking catalyst faujasite (**FAU**, 12-ring channels). The 3D pore system of the **MFI** framework consists of 10-ring straight channels interlinked with 10-ring sinusoidal channels (Figure 6), providing increased yields of hydrocarbons with a short carbon chain, in particular ethylene and propylene.

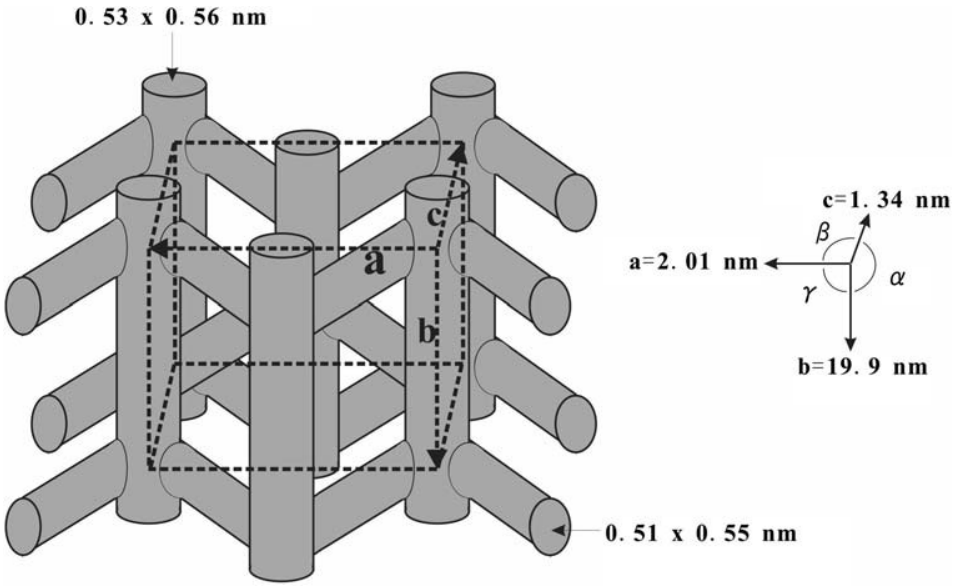

Figure 6: **MFI** zeolite channel system and unit cell parameters. Reprinted from Ref.[22]

Zeolites with the **MFI** framework act as an industrial standard for many catalytic processes and are among the most versatile and studied zeolites. **MFI** zeolites have been successfully prepared with many different heteroatoms, such as Ti, B, Fe, and Ga. According to Ref[23], the **MFI** zeolites containing different heteroatoms can be arranged according to their relative BAS strength in this order: Al > Ga > Fe > B. In addition to the tuneable acid strength, the concentration of acid sites can also be varied for **MFI** zeolites in a wide range by changing the Si/T ratios. **MFI** zeolites can be prepared with a Si/Al ratio ranging from 10 to 140, Si/Ga ratios of 20 – 120, and Si/Ti ratios of 20 – 50.

The most common SDA for **MFI** synthesis is tetrapropylammonium hydroxide, which is used for the preparation of conventional 3D **MFI** zeolites with different chemical compositions.[9, 24-26] **MFI** zeolites can also be synthesized as 2D materials. This can be done using different templates, such as $C_{22}H_{45}–N^+(CH_3)_2–C_6H_{12}–N^+(CH_3)_2–C_6H_{12}$, or $C_nH_{2n+1}–(N^+(R)_2–C_6H_{12})_m–N^+(CH_3)_2–\ C_nH_{2n+1}$ (n = 18, 22; m = 2; 3) (Figure 7).[27-29] The SDA for the synthesis of 2D structure needs to have a hydrophilic and hydrophobic group, so it acts like a surfactant. The hydrophilic group serves as a structure-directing moiety and the hydrophobic group blocks the growth of the zeolite crystals in one direction. [30]

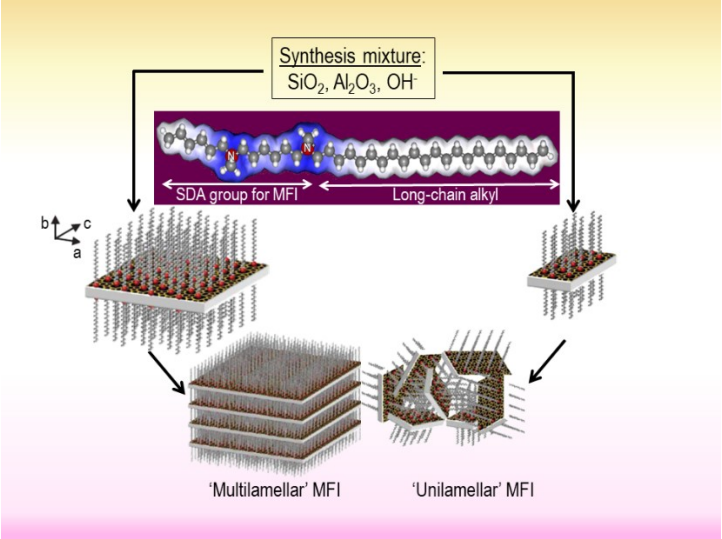

Figure 7: SDA for the preparation of 2D **MFI** of multilamellar and unilamellar arrangements. Adapted from Ref.27

2.1.3.2. MWW

The **MWW** framework has 10-ring pores with 12-ring cups on the external surface of the zeolite crystals (Figure 8). **MWW** zeolite was introduced into industrial use in the 1990s due to its ability to catalyse aromatic alkylation reactions.[6] At that time, it was discovered that a 2D layered precursor of **MWW** zeolite, denoted MCM-22P, forms after hydrothermal synthesis with hexamethylenediamine (HMI) as an SDA. By changing the synthesis conditions (such as using aniline as a structure-promoting agent), the synthesis can also yield MCM-49 (3D **MWW**, identical to calcined MCM-22) or MCM-56 (disordered **MWW** monolayers).[31] The MCM-22P precursor can be modified using various post-synthesis treatments to generate different layers arrangements (Figure 9).[32]

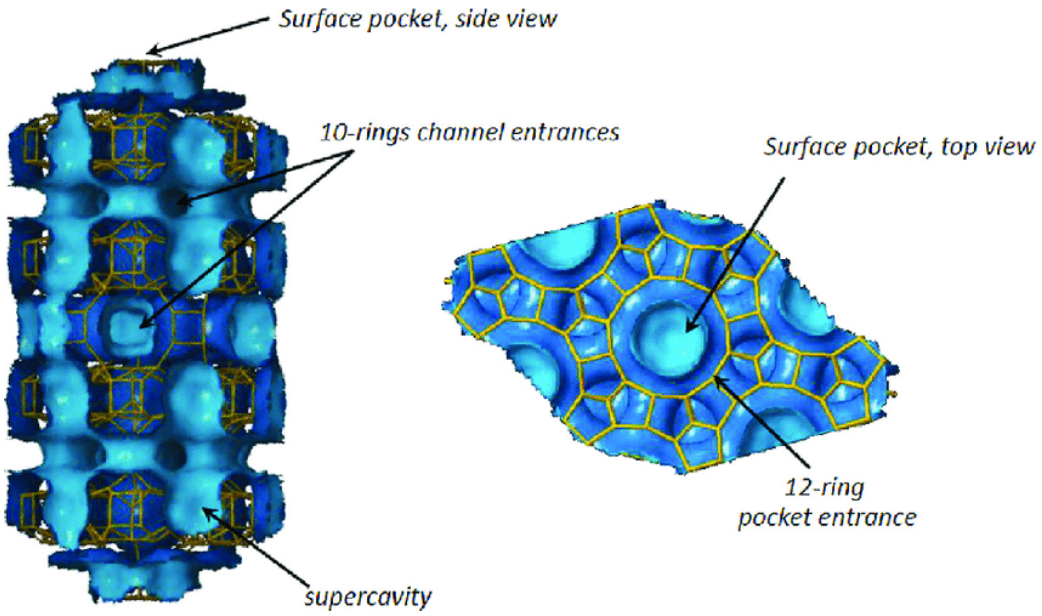

Figure 8: **MWW** framework with 10-ring sinusoidal channels and 12-ring external cups on the surface of zeolite crystals. Reprinted from Ref.[33]

The first option for post-synthesis treatment of the layered MCM-22P precursor is calcination. SDA is removed from the interlayer space during calcination, and Si-OH groups condense to form Si-O-Si interlayer connections. The result of a calcination is a 3D **MWW** or MCM-22 material. MCM-56 is a disordered monolayered material, which can be synthesized directly, or gained by controlled acid treatment of MCM-22P with HNO_3. The 2D precursor can also be swollen by incorporation of an organic cationic surfactant, such as cetyltrimethylammonium, between the layers to increase interlayer distance. Swelling of the sample allows further modification by pillaring or delamination. For pillaring, the sample is treated with an additional source of silica, most commonly TEOS. The sample is calcined to release the organics and form amorphous silica pillars by condensation of TEOS molecules, yielding the MCM-36 material. The delamination can be done either by liquid exfoliation or by ultrasonic treatment of the swollen sample. Liquid exfoliation is done by preparing a colloidal dispersion of MCM-56 zeolite monolayers by a treatment with a solution of tetrabutylammonium hydroxide, which favours delamination of the monolayers in the solution. These procedures create a delaminated material, changing the original ordered structure into a disordered one, which significantly increases the external surface area.[34-35]

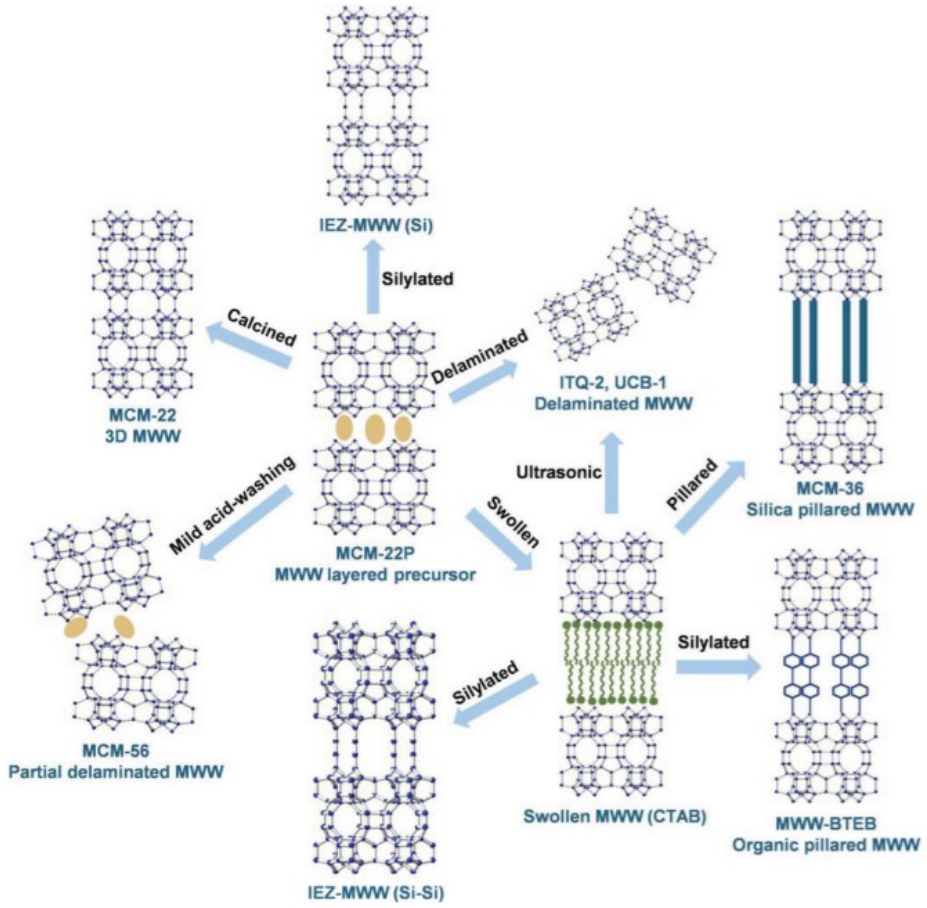

Figure 9: Post-synthesis modifications of MCM-22P. Reprinted from Ref.[36]

2.2. Methods for characterization and evaluation of zeolites

The most widely used characterization methods applied for aluminosilicate zeolite catalysts, such as X-ray diffraction, physisorption, electron microscopy, and spectroscopy, are discussed in this section with a special focus on the evaluation of acid site characteristics with FTIR spectroscopy.

2.2.1. X-ray diffraction (XRD)

XRD is a comprehensive tool for the characterization of different crystalline materials, for example zeolites, clays, and ceramics. In addition, XRD is also a favoured technique for the determination of the structure of proteins and biological macromolecules in biological science.[37-38] The principle of this method lies in the scattering of X-rays, roentgen radiation, by the atoms in a periodic structure of the crystalline material, which creates an interference effect. To produce diffraction, the spacing between the planes in a crystal and the wavelength of the used radiation must be of the same order of magnitude. The X-rays meet this condition since their wavelength (0.01 – 10 nm) and spacing of the atoms in the crystal lattice are comparable. The X-rays are also energetic enough to penetrate solids for probing their

internal structure. When the X-ray beam interacts with an atom, two processes may occur: the beam can be absorbed or scattered (Figure 10).[39] With the XRD method, the elastically scattered X-ray photons are detected and analysed. Different atoms in the solid occupy distinct positions in the crystal and therefore cause scattering with different phase shifts, interfering with each other.

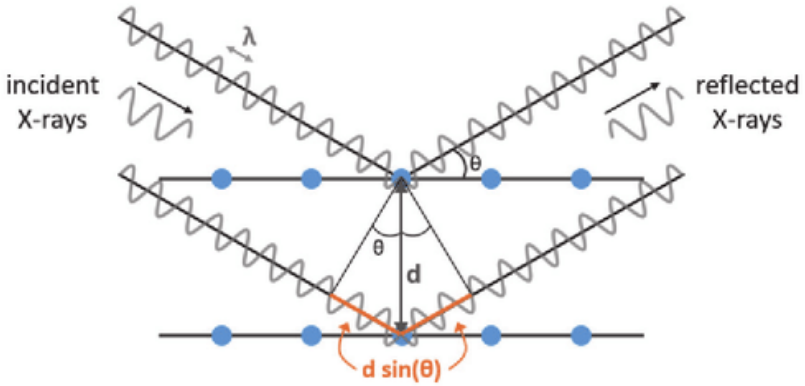

Figure 10: Schematic representation of X-ray scattering by the atoms. Reprinted from Ref.[40]

In crystalline materials, including zeolites, the X-ray radiation with wavelength λ is diffracted by atoms with characteristic spacing between the crystal planes d. If the difference in path length of two X-rays is equal to the integral number of wavelengths of these waves, then the waves are in phase, and they interfere constructively. The condition of this constructive interference is shown by the Bragg law (Equation 1), which relates the distance d between the planes of atoms that give rise to diffraction peaks in studied material with the angle between the incident beam and the lattice plane, θ:[39]

$$n\lambda = 2d \sin\theta \quad (1)$$

Principally, the XRD method uses two techniques to study crystalline materials: single-crystal and powder XRD. For single-crystal XRD, the diffraction pattern is collected in a form of characteristic diffraction spots (Figure 11a) and offers all the information needed to solve the structure of the studied material. However, using single-crystal XRD for the study of zeolites is problematic, since the zeolite crystals tend to be too small (few microns). For this reason, powder XRD is a common technique used to identify the zeolite's structure. The powder XRD method measures the X-ray diffraction of many crystals with random orientation. This random orientation of the crystals causes the transformation of the diffraction spots (seen with single-crystal XRD) into a set of circles (Figure 11b), from which the diffraction pattern can be gained as a dependency of the diffraction intensity on θ angle,

which is usually shown as 2θ angle. The measured diffractograms are unique for each material and, in case of zeolites, each structure shows a unique diffractogram. Usually, the zeolite structure is then identified by comparing the measured diffractogram with theoretical models or measured diffractograms of reference zeolites, collected in the database of the International Zeolite Association.[5] The diffractogram shows the peak positions (2θ angles), which are connected to the size and shape of a unit cell, peak widths that relate to crystallite size, and peak intensities related to atom arrangement in the unit cell and their nature.[41]

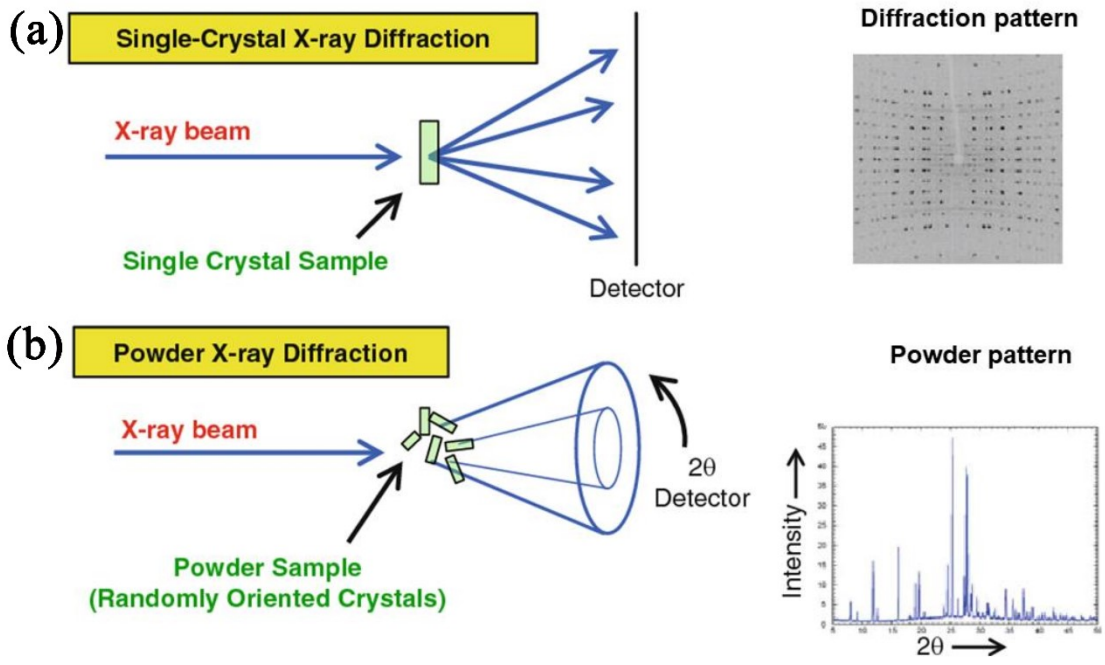

Figure 11: Comparison of a) single-crystal and b) powder XRD. Reprinted from Ref.[42]

2.2.2. Gas physisorption

The essential characteristics of zeolites are their pore volume and surface area. These characteristics are usually referred to as textural properties. The physisorption of gases, such as nitrogen and argon, is a common way of assessing the textural properties of zeolites. Physisorption takes place by adhering gas molecules to the solid surface *via* intermolecular forces at a pressure that is lower than saturated vapor pressure. The intermolecular forces upon physisorption include dipole-dipole moment attraction, dipole-induced dipole attraction, ionic-induced dipole attraction, London forces, and hydrogen bonding. The intermolecular forces are relatively weak, especially when compared to chemisorption, which refers to the chemical bonding of adsorptive molecules to the surface, including the formation of covalent and ionic bonds.[43]

N_2 and Ar are the adsorptives that are the most commonly used to characterize the textural properties of zeolites. They have a similar kinetic diameter of 0.36 and 0.34 nm but differ in atomicity. Nitrogen exists in a diatomic form which is not spherical; this causes a reduction in the measurement accuracy, especially for micropores due to the specific interactions. In contrast, Ar is a spherical particle and is inert towards specific interactions with functional groups of measured materials. Because of these advantages, argon is recommended as a preferential adsorptive for measuring the textural properties of microporous materials.[44]

The adsorption isotherm is measured as the amount of adsorbed gas against the pressure of an absorptive at a constant temperature (77.3 K and 87 K for nitrogen and argon, respectively). Pressure is usually plotted as a relative pressure, which is equal to the adsorbate pressure divided by the saturation vapor pressure. Adsorption isotherms are measured either volumetrically or gravimetrically. The measurement procedure for both methods is the same. Firstly, the entire system needs to be kept at constant temperature close to the boiling point of the used adsorptive during the whole experiment. Then, the pressure of the adsorptive is increased stepwise, while being held constant between each step until equilibrium is reached. With the volumetric method, the amount of adsorbed gas is measured by the detected pressure change and its comparison to the expected pressure change if the adsorbent was absent. With the gravimetric method, the amount of adsorbed gas is measured by mass gain.

According to the IUPAC classification, there are six types of adsorption isotherm denoted type I – VI (Figure 12).[45] Isotherm I is characteristic for either chemisorption or physisorption on purely microporous material. Isotherm II is characteristic for nonporous materials with high adsorption energy. Isotherm III is characteristic for nonporous materials with low adsorption energy. Isotherm IV is characteristic for mesoporous materials with high adsorption energy. The presence of a hysteresis loop in the type IV isotherm is caused by the difference in nucleation and evaporation in mesopores. Isotherm V is characteristic for mesoporous materials with low energy of adsorption. Isotherm VI is characteristic for materials containing multiple pore sizes or two or more types of adsorption sites with distinct adsorption energies.[45] After identification of the isotherm, one can use many different methods for acquiring the textural properties of the material depending on the type of isotherm.

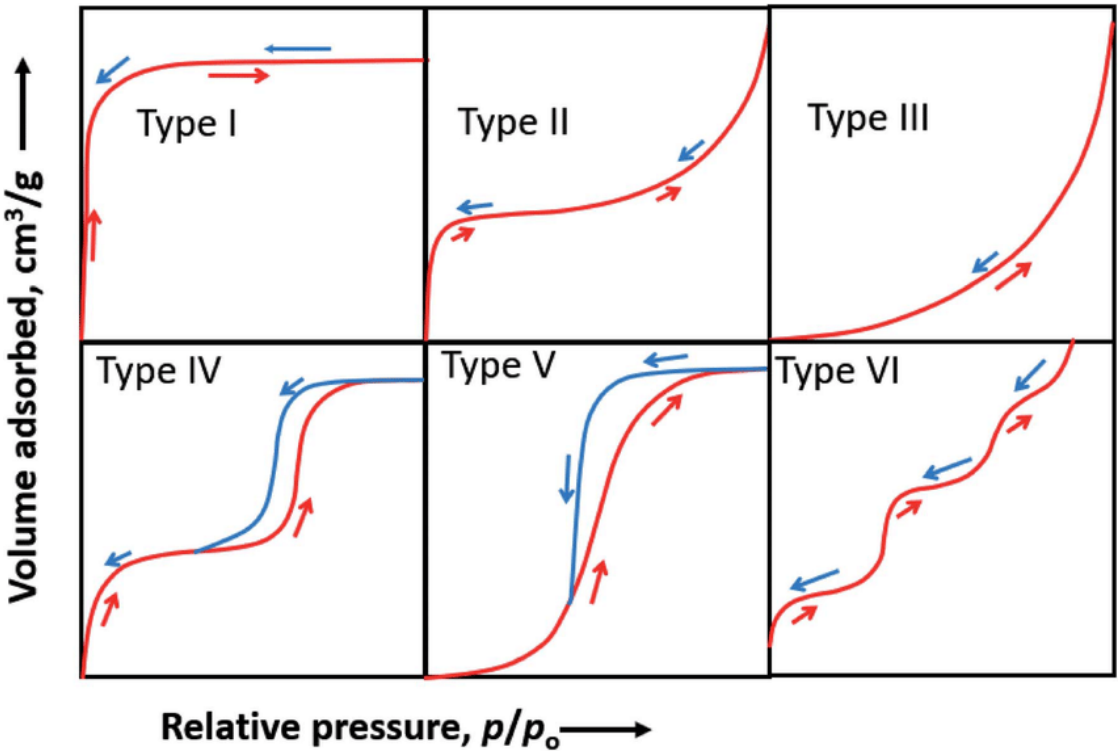

Figure 12: Isotherm types according to the IUPAC classification. Reprinted from Ref.[46]

2.2.3. Electron microscopy

Electron microscopy is an essential method for analysis of the morphology and textural properties of zeolites. This technique takes advantage of the much lower wavelength of electrons compared to visible light (380 to 700 nm for visible light, while electrons reach <1 pm at high accelerating voltage). This lower wavelength then offers a much higher resolution. Besides high resolution, another advantage of electron microscopes is the ability to change the electron wavelength by adjusting the acceleration voltage of the electrons. The formula for the wavelength of an electron is shown in Equation 2, where λ is the wavelength of the electrons, h is the Planck constant, m_e is the weight of an electron, e is the charge of an electron, and U is the acceleration voltage. With higher acceleration, modern electron microscopes can reach nanometre or even sub-nanometre scale. However, microscopy techniques have the disadvantage of providing information only about a local area, which might not be representative of the whole sample.[47]

$$\lambda = \frac{h}{\sqrt{2m_e eU}} \tag{2}$$

There are two main types of electron microscopes, differing in instrumentation and information provided. The first one is the scanning electron microscope (SEM) and the second one is transmission electron microscope (TEM). With SEM, the image is formed by

scanning the surface of a sample with a narrow-focused electron beam (Figure 13a). The interaction of the electron beam with the material creates various signals. These detected signals are backscattered electrons (BSE), characteristic X-rays, and secondary electrons (SE). BSEs are observed by elastic and inelastic scattering of the primary electrons. The intensity of BSE is dependent on the local average atomic number of the sample. Therefore, the observed BSE gives information about the local compositional difference in the sample. The SEs are produced by free and/or valence electrons in the sample surface. This signal provides information about the topography and morphology of the sample. Characteristic X-rays give information about the chemical composition of the observed microregion using X-ray spectrometers. One of the conditions for SEM measurement is the conductivity of the sample. Samples that are not conductive, such as zeolites, need to be covered with a thin layer of conductive metal (e.g., Au, Pt) before the measurement.[47]

The construction and principles of TEM are similar to those of optical microscopes, except for using an electron gun as a source of electrons and magnetic lenses to focus the electron beam. In TEM, the image is formed from electrons, which pass through a thin sample (0.5-1 μm) (Figure 13b). Usually, TEM requires a higher acceleration voltage than SEM because of the need for electrons to penetrate the sample. The use of a higher acceleration voltage offers a higher resolution, but it might be disadvantageous for working with samples that are more susceptible to radiation damage. TEM is suited for the study of nanometre-scale features, such as crystal structure defects, local intergrowths of distinct phases, porosity, and interlayer spacing in layered materials.[47-48]

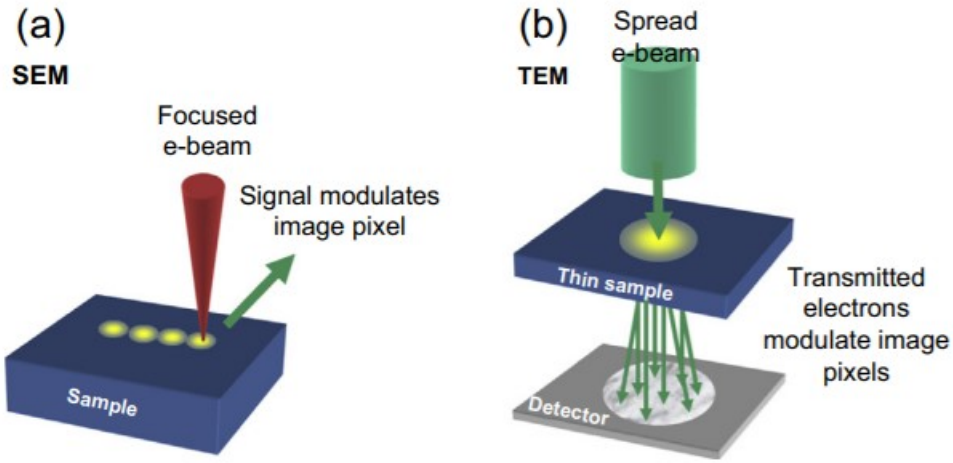

Figure 13: Schematic representation of SEM (a) and TEM (b) imaging. Reprinted from Ref.[49]

2.2.4. Optical emission spectroscopy (ICP-OES)

Inductively Coupled Plasma Optical Emission Spectroscopy (ICP-OES) has become a commonly used method for chemical analysis *via* optical spectroscopy since the introduction of the first commercial instruments in 1974. ICP-OES is used for bulk qualitative and quantitative analysis of samples in liquid form. But since the first uses of this method, diverse ways for measurement have been developed, such as spark discharge or laser ablation. With these methods, thin films and surfaces of solids can also be analysed. The main advantages of this method are its speed, wide linear dynamic range, low detection limits, and relatively small interference effects. The precision of this measurement is typically 0.2 – 0.5%.[50]

Because of its advantages, ICP-OES is a commonly used method for analysing elemental composition (Si/T ratio) of zeolites. Because ICP-OES requires a liquid sample for measurement, zeolites must first be dissolved. The common approach is dissolution in concentrated hydrochloric, nitric, and hydrofluoric acid mixtures at elevated temperature. However, the use of hydrofluoric acid is problematic for technical reasons. The ICP-OES instrument is composed of a sample introduction system, a plasma torch, a plasma power supply, an impedance matcher, and an optical measurement system (Figure 14).[50]

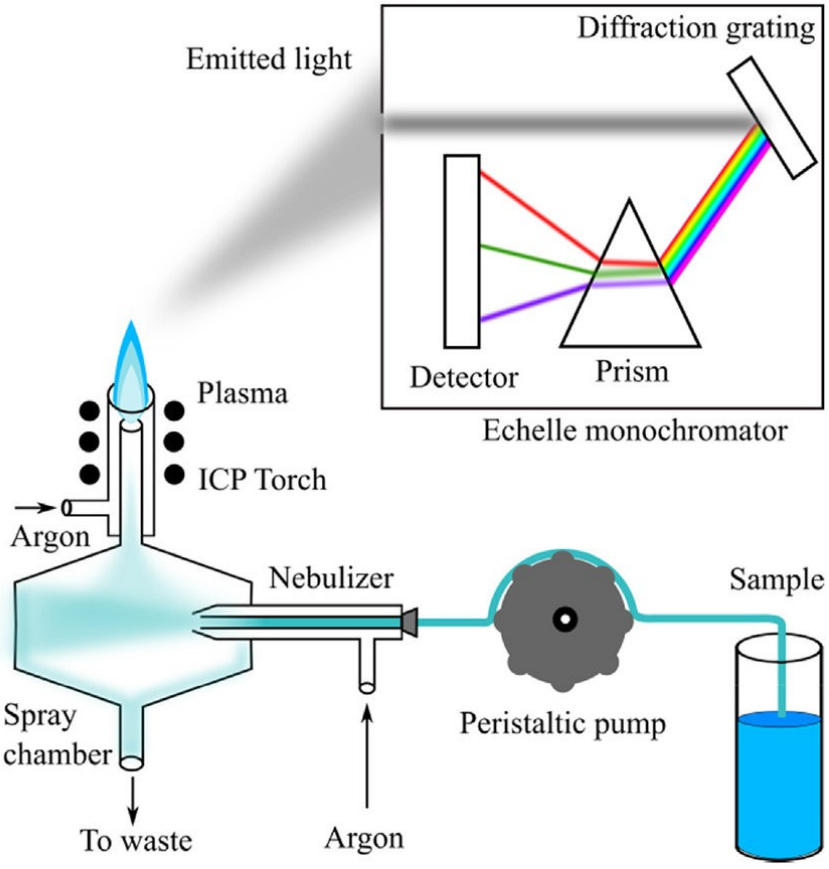

Figure 14: ICP-OES instrumentation. Reprinted from Ref.[52]

Fluoride damages the sample transport system made of quartz or glass. For this reason, boric acid or another commercially available complexing agent is utilized to bind the hydrofluoric acid. This liquid sample is then converted to aerosol form and introduced into the plasma for atomization. This atomization process generates different excited atoms and ions that generate a radiation with a characteristic wavelength. This wavelength of the emitted radiation is used to identify the elements in the sample, and the elemental concentration of this sample is calculated based on the intensity of the radiation. [50-51]

2.2.5. IR spectroscopy

Infrared (IR) spectroscopy is a powerful tool for characterization of the local structure and surface chemistry of zeolite. The infrared region of the electromagnetic spectrum was first discovered at the beginning of the 19th century by the astronomer Sir William Herschel. Following this discovery, the phenomenon of Raman scattering was discovered by C. V. Raman in the year 1928. These two discoveries were the beginning of vibrational spectroscopy. Since then, vibrational spectroscopy has become a prevalent technique for molecular scale characterization of the structure of matter. Vibrational transitions measured by these methods are dependent on the chemical composition and bonding arrangement of the studied material; therefore, vibrational spectra are considered the molecular 'fingerprint' of a material.[53]

Vibrational spectroscopy is based on interaction of low-energy infrared radiation with the studied material. Part of the radiation with low energy is absorbed, stimulating perturbations of molecular bonds, i.e., stretching (change in the length of the bonds) and bending (change in angle between bonds) vibrations. Vibration stimulation can cause a change in the dipole moment (visible by infrared), a change in their polarization (visible by Raman), or both, depending on the molecular symmetry of the studied material. These selection rules are the reason why infrared and Raman spectroscopies are considered complementary methods. In general, vibration of two bonded atoms A-B can be described as a harmonic oscillator. This approximation lets us define resonant frequency ν using Equation 3:

$$\nu = \frac{1}{2\pi}\sqrt{\frac{k}{\mu}} \tag{3}$$

where k is the spring constant of the bond and μ is the reduced mass (Equation 4) of the bonded atoms A and B.

$$\mu = \frac{m_A m_B}{m_A + m_B} \quad (4)$$

The harmonic oscillator approximation can be used for the description of the relation between resonance frequency and mass of atoms. But for describing real spectra, anharmonic oscillator model is needed.[54]

Because the vibration frequency of any bonded atoms or group of atoms depends on their mass and the strength of the bond, the wavenumbers of the characteristic absorption bands are used in qualitative analysis. Although infrared spectra can be measured using either the absorbance or transmittance mode, the absorbance mode has a simple advantage for quantitative analysis since absorbance (Equation 5) is linearly proportional to concentration according to the Beer–Lambert law[55]:

$$A = \varepsilon l c \quad (5)$$

where A is absorbance, ε is molar absorption (extinction) coefficient, l is sample thickness, and c is concentration.

In turn, the absorbance of infrared radiation by a sample is defined by Equation 6:[56]

$$A = log\left(\frac{I_0}{I}\right) \quad (6)$$

where A is absorbance, I_0 is the intensity of emitted radiation, and I is the intensity of light transmitted by the sample.

The key element of the modern infrared spectrometers is Michelson's interferometer. Michelson's interferometer consists of three active parts: moving reflector, fixed reference reflector and beam splitter (Figure 15). Light from the source is initially split into two beams on the beam splitter. The first beam is directed to the fixed reflector, and the other one towards the reflector moving at a constant velocity over a set distance. This distance plays a key role in the spectrometer's resolution. The velocity of the moving mirror is controlled by the laser wavelength in the system, which also acts as an internal wavelength calibration. These two reflected beams are then recombined at the beam splitter, and an interference pattern is created since the distances the two beams travelled are different. The interfered beam then goes through the sample and into the detector. The signal is then recorded as an interferogram and is then processed by a technique called Fourier transformation to transform the raw data into the final spectrum.[55]

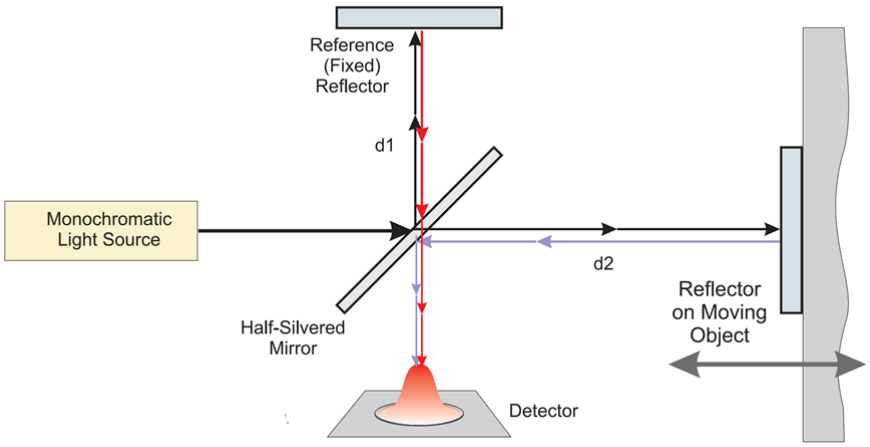

Figure 15: Scheme of the infrared spectrometer with Michelson's interferometer. Reprinted from Ref.[57]

FTIR spectroscopy is used to analyse the properties of zeolites both qualitatively, and quantitatively. This includes the structural features and the characteristics of acid sites.

2.2.5.1. Framework structure and composition

The stretching and bending vibrations of the T-O bonds in zeolites can be observed in the wavenumber range of 1500 – 200 cm^{-1}. There are two types of bands observed in the spectra of the zeolite framework, the intra-tetrahedral and the inter-tetrahedral bands assigned to the respective bonds in the lattice (Table 1). Intra-tetrahedral bands are observed in the spectra independently of the topology of the framework, meaning that they are structurally insensitive. They include the symmetric (720 – 650 cm^{-1}) and asymmetric (1250 – 950 cm^{-1}) stretching vibrations and bending (500 – 420 cm^{-1}) vibrations of T-O bonds in the TO_4 tetrahedra. The inter-tetrahedra vibrations are instead structurally sensitive, and thus different bands can be observed in the spectra for each zeolite structure.

Table 1: Intra-tetrahedral and inter-tetrahedral bands[60]

Intra tetrahedral	Wavenumber cm^{-1}	Inter tetrahedral	Wavenumber cm^{-1}
Asymmetrical stretching	1250-950	Double ring	650-500
Symmetrical stretching	720-650	Symmetrical stretching	820-750
T-O bending	500-420	Asymmetrical stretching	1150-1050

For example, the **MFI** zeolite shows two specific bands attributed to its framework. The first one is observed at 550 cm^{-1}, and it is assigned to the vibration of 5-member rings in its structure, and the second one is observed at 450 cm^{-1}, and it corresponds to the internal

vibration of alumina and silica tetrahedra.[56, 58] These bands can also be used for investigating the synthesis of zeolites, in particular formation of its nuclei containing specific structural units during hydrothermal template-assisted crystallization.[59]

The region of zeolite framework vibrations in IR spectra is also frequently used to confirm an incorporation of elements such as B (the appearance of characteristic bands at 1380 and 920-890 cm^{-1}), Fe (1010 cm^{-1}), Ti (960 cm^{-1}) into the zeolite lattice. [61]

2.2.5.2. Concentration, strength, nature, and accessibility of acid sites

BAS in zeolites, that is, Si-(OH)-Al groups, can be studied directly by analysing the FTIR spectra in the region of O-H group vibrations. (3800 – 3200 cm^{-1}). The bands of BAS are detected in the region between 3680 and 3550 cm^{-1} (Figure 16). The exact frequency of the band depends on the zeolite topology, chemical composition, and location of BAS. Three other slightly acidic types of silanol groups can be observed in zeolites; these groups are linked to structural defects. The frequency of stretching vibration of external surface silanol groups, the terminal silanol groups, can be observed at around 3745 cm^{-1}. The bands associated with isolated silanol groups are shifted to a frequency of around 3720 cm^{-1}. Hydrogen bonding leads to perturbed silanol groups; the respective band can be observed at frequency around 3500 cm^{-1} (Figure 16).[56]

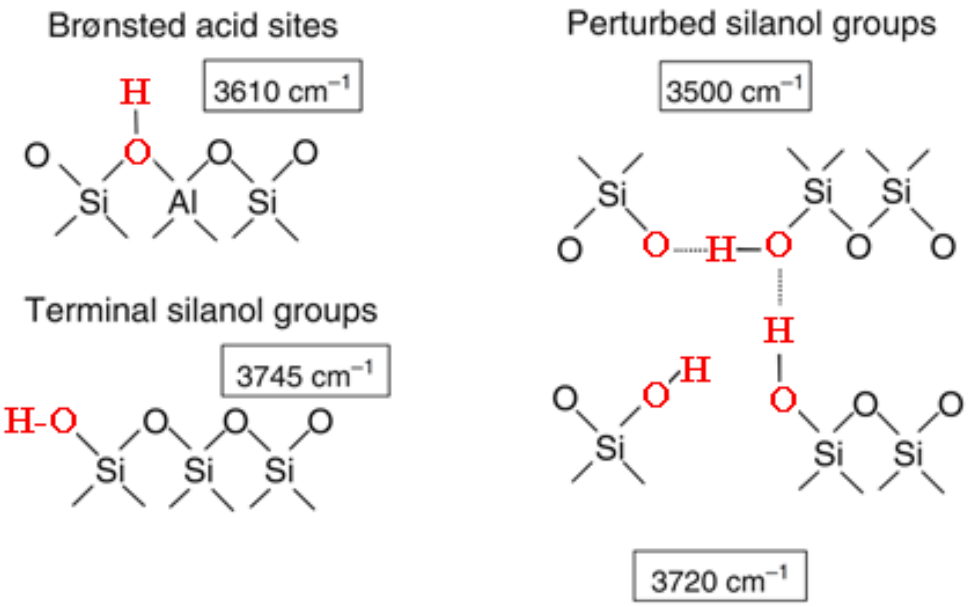

Figure 16: Different hydroxyl groups observed in zeolites. Adapted from Ref.[56]

External silanol group vibrations are always observed in zeolites, but their relative intensity depends on the size of zeolite particles. Zeolites with smaller particle sizes show

higher intensity of the Si-OH groups vibration.[56] Because the frequency of bridging OH groups is dependent on zeolite topology, aside from acid site strength, it is impossible to compare the acid site strength of zeolites with different topologies. However, the strength of BAS can be compared by measuring the spectra of adsorbed probe molecules.

When choosing a probe molecule to study the acidic properties of zeolites, one should keep in mind these criteria:[56]

1. The probe molecule should interact with the solid only through its base electron pair donor function, not by the acidic electron pair acceptor function. This condition is fulfilled by strong Lewis bases, for example, ammonia and pyridine.
2. The bands of characteristic vibration in the probe molecule adsorbed on LAS and BAS should allow one to distinguish between them. For example, pyridine adsorbed on BAS in the form of pyridinium ion gives rise to the characteristic absorption band at 1545 cm^{-1}, while pyridine adsorbed at LAS shows the band at 1455 cm^{-1}. These two bands do not overlap and, therefore, allow for a quantitative and qualitative analysis of the nature of acid sites (Figure 17).
3. The sizes of probe molecule and reactant (for reaction relevant to the studied material) should be comparable.
4. The probe molecule should interact with the acid site without a chemical reaction.

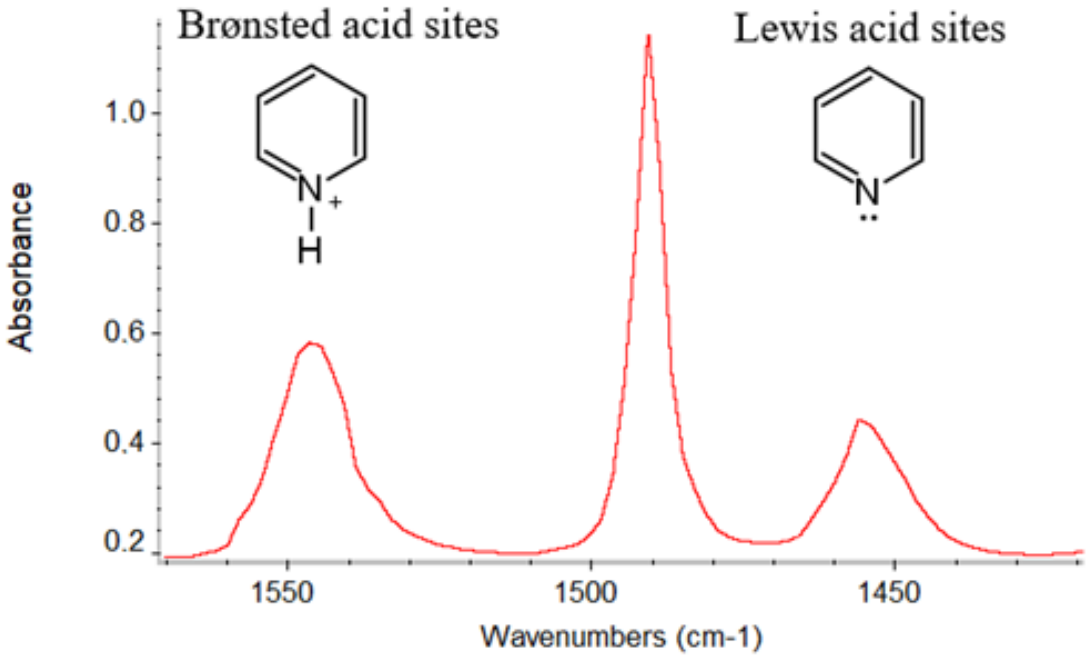

Figure 17: FTIR spectra of adsorbed pyridine, showing a clear distinction between acid sites with different nature.

The strength of zeolites acid sites is measured by FTIR-monitored thermodesorption of a chosen probe molecule. With increasing temperature, the probe molecule starts to desorb from the solid. This can be observed as a decrease in intensity of the corresponding band in the IR spectra. The relative concentrations of the acid sites holding pyridine at high temperature (350 °C for aluminosilicate zeolite) can be considered a measure of the acid site strength of a zeolitic material.

Because the catalytic efficiency of the zeolites strongly depends on the concentration of active sites accessible for reagents, FTIR methods were developed to measure the concentration of acid sites with different accessibility. One of these methods is the adsorption of alkyl pyridines with different kinetic diameters (e.g., pyridine: 0.54 nm, lutidine: 0.67 nm, collidine: 0.74 nm, and 2,6-di-tert-butylpyridine: 0.79 nm). From these examples, pyridine and 2,6-di-tert-butylpyridine seem to be the most suitable probes to distinguish external acid sites in 10-ring channel zeolites, such as **MFI** and **MWW**. Although pyridine can interact with acid centres both in zeolites micropores and on the external surface of its crystals, 2,6-di-tert-butylpyridine is unable to enter the micropores of these 10-ring zeolites, but it can interact with the acid sites located on the external surface.[32]

2.2.6. Gas Chromatography

After complete characterization of the zeolite sample, it is important to measure its activity in a catalytic reaction. The most common way of this measurement is taking samples periodically from a catalytic reaction in progress, and then separating and analysing the mixture with chromatography. Principally, the chromatographic methods separate individual reagents from a mixture based on their interaction with a stationary phase. The mixture is carried through the stationary phase by a mobile phase. The individual compounds of the mixture are then retarded by their interaction with the stationary phase.

A common method for separating organic compounds is gas chromatography, but there are other chromatographic methods with different uses, such as thin-layer chromatography, liquid chromatography, or ion exchange chromatography. In gas chromatography, the mobile phase is a gas, and the stationary phase is a solid. For instrumentation, each gas chromatograph is composed of a sample introduction device, often referred to as an injector, a source of gas, which acts as a mobile phase, a column with stationary phase, and a detector (Figure 18).

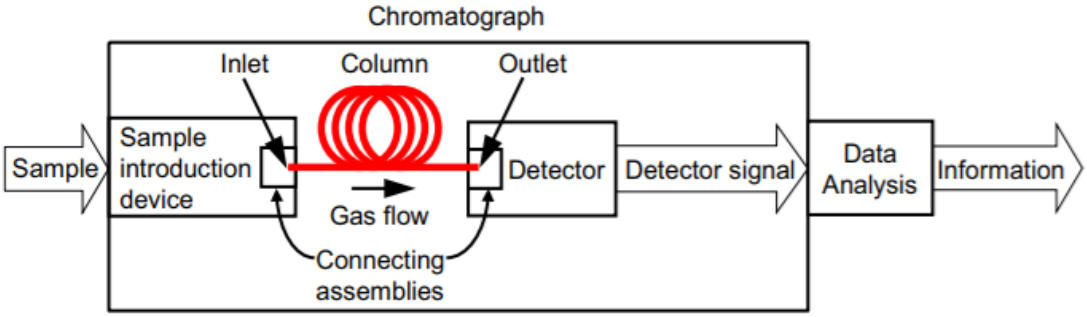

Figure 18: Gas chromatograph instrumentation.[62]

Firstly, the sample is injected and vaporized into the mobile phase, which is the carrier gas. The usually used carrier gases are helium or nitrogen. After the injected sample is vaporized, it is carried by the mobile phase through a column containing a stationary phase. The column can be either a packed column or a capillary column of variable polarity, with the length of the column ranging from 1 to 200 m with inner diameter of 0.1 to 4 mm, depending on the column type. During measurement, the column is heated to a set temperature to ease the separation of mixture components. After the sample passes through the column, it enters the detector. The detector monitors the output gas and reacts to the presence of each individual compound as it passes through. This passing can be seen as a signal (a peak) in the chromatogram, whose intensity is directly proportional to the concentration of a compound in the mobile phase. The flame ionization detector (FID) is the most widely used detector for the detection of organic compounds. FID uses a hydrogen-oxygen flame to combust organic compounds, resulting in the formation of ions. The signal created by the ions is detected as a current by two electrodes used to provide a potential difference. The detected current corresponds to the proportion of reduced carbon number atoms in the flame. The response of the detector increases linearly for hydrocarbons; however, for molecules with unsaturated bonds and heteroatoms, the situation is more complex. In these cases, it is necessary to determine the response factor experimentally by calibration or by using the effective carbon number concept.[63-65]

2.3. Prins-Friedel-Crafts (PFC) reaction

The Prins-Friedel-Crafts reaction of homoallylic alcohol (**HA** in Figure 19), aldehyde (**ALD**), and aromatic compound (**ArC**) that yields valuable pyran derivatives (**1** and **2**) is an example of one-pot multicomponent cascade processes.[66-69]

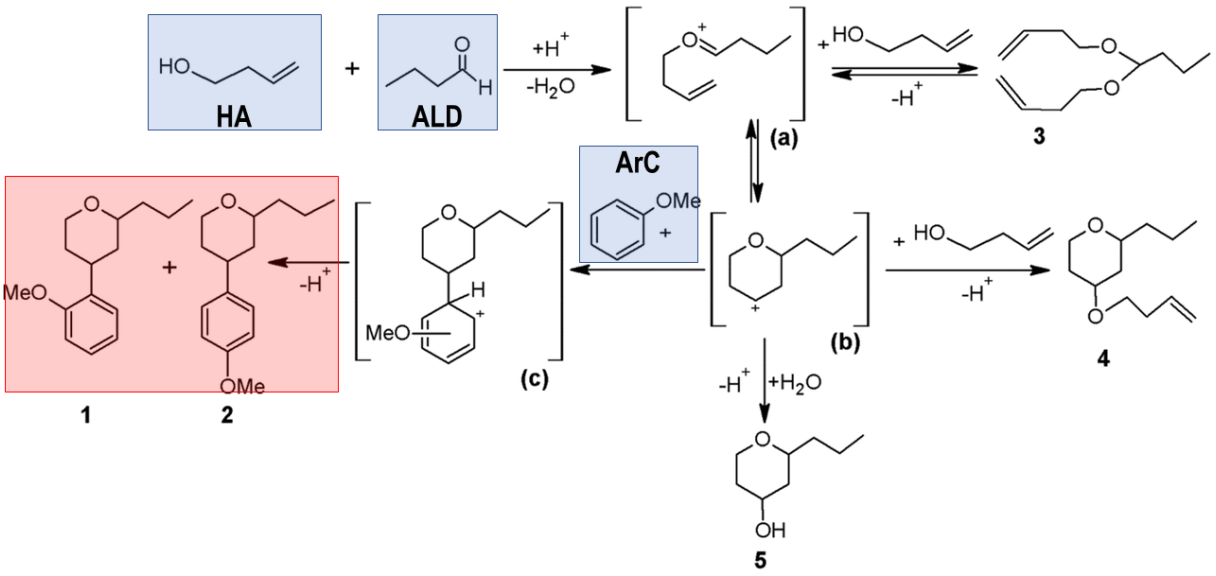

Figure 19: PFC reaction scheme, using 3-buten-1-ol, butyraldehyde and anisole as substrates. **a)** carbocation, **b)** cyclic carbenium ion, **c)** product intermediate, *o*- and *p*-isomers **1)** 4-(2-methoxyphenyl)-2-propyl tetrahydropyran, **2)** (4-methoxyphenyl)-2-propyl tetrahydropyran, **3)** butyraldehyde di-3-butenyl acetal, **4)** 4-(3-buten-1-oxy)-2-propyl tetrahydropyran, **5)** 2-propyloxan-4-ol. Adapted from Ref.[70]

The first step of the PFC cascade, the Prins reaction was first reported by Hendrik Jacobus Prins in 1919,[71] as an acid-mediated addition of an alkene to an aldehyde. This results in the formation of a carbocation (such as **a**) that might lose a proton to form a homoallylic alcohol (such as **3**), or it can undergo cyclisation (cyclic cation **b**) and react with a nucleophile (such as **ArC**) to form a substitution product (such as **1** and **2**) from a product intermediate (**c**). The scope of Prins reactions has increased since their discovery. Different variants of the Prins reaction were reported,[72] such as aza-Prins (addition of alkene to iminium ions) or thia-Prins (addition of alkene to thiocarbenium ions) reactions. The Prins cyclization reactions are essential for modern heterocycle synthesis, mainly because of their well-defined transition states and highly predictable stereocontrol, used, for example, for the synthesis of neopeltolides.[72]

The second step of the PFC cascade, Friedel-Crafts alkylation reaction was first described by Charles Friedel and James Mason Crafts in the year 1877.[73] Friedel-Crafts alkylation is a typical reaction of electrophilic aromatic substitution, usually involving alkyl halides as alkylating agents. It is generally accepted that this reaction can be catalysed by both LAS and BAS.[70, 74] The role of the catalyst consists in the generation of an attacking electrophilic species, that is, alkyl cation. In the case of the PFC cascade process, a

carbocation **a** (formed by the reaction of aldehyde **ALD** and a homoallylic alcohol **HA**) acts as an electrophile attacking the aromatic hydrocarbon **ArC**.

The combined PFC reaction is used for efficient synthesis of molecules containing different functional groups, such as 4-arylpiperidine, indeno-tetrahydropyridine, isoquinolines, isothiochromenes, isochromenes and 4-aryl tetrahydropyrans.[75] The 4-aryl tetrahydropyran group of substances commonly occur in biologically important compounds, such as pheromones, polyether antibiotics and various pharmaceutical agents.[76-77] Synthesis of molecules containing the 4-aryl tetrahydropyran group *via* acid-catalysed one-pot three-component cascade PFC reaction has been performed using different homogeneous Brønsted (e.g., boron trifluoride etherate, scandium and indium triflate) and Lewis (e.g., p-toluene sulfonic acid, trifluoromethanesulfonic acid and camphor sulfonic acid) acid catalysts and their combination.[78-82]

The use of these homogeneous Brønsted and Lewis acid catalysts is advantageous for the high efficiency and selectivity of the reaction but at the same time aggravated due to environmental unfriendliness of such types of catalysts, their toxicity, and economic issues connected with the separation of the catalyst after reaction. Thus, the application of a heterogeneous catalyst is an alternative way to facilitate this reaction with avoiding abovementioned issues. Examples of heterogeneous catalysts used for the PFC reaction are montmorillonite K10 clay, zeolites **MWW** and **BEA**.[70, 74, 83-84] Particularly, the use of zeolites seems to be an effective way to achieve good efficiency and selectivity towards products containing 4-aryl tetrahydropyran containing products. Zeolites are non-toxic, easy to separate, non-corrosive, and they catalyse the targeted reaction at mild temperatures (60 °C).[70, 74]

Recent progress in synthesis in hierarchical zeolites gives new possibilities to zeolite use, namely in conversion of bulky reagents for the synthesis of different complex molecules. This work studied hierarchical zeolites of different chemical composition and structure in the PFC reaction to address a notable features of active and selective acid heterogeneous catalysts towards designing this attractive one-pot multicomponent cascade reaction and its subsequent implementation. There are not many studies concerning the usage of zeolites in PFC reaction[70, 74, 83-84] and therefore, the effect of zeolites' characteristics on the reaction is not well understood yet.

3. Experimental part

3.1. List of Chemicals

The chemicals used for the synthesis and post-synthesis modifications of zeolites, FTIR measurements, and catalytic experiments are listed in Table 2.

Table 2: List of chemicals

Chemical	Purity	Manufacturer
2,6-Di-tert-butylpyridine	97%	Sigma Aldrich
3-buten-1-ol	≥98%	Sigma Aldrich
Aluminium nitrate nonahydrate	≥98%	Sigma Aldrich
Ammonium nitrate	≥99%	Sigma Aldrich
Anisole	99%	Sigma Aldrich
Butyraldehyde	≥96.0%	Sigma Aldrich
CAB-O-SIL M-5		Acros Organics
Dodecane anhydrous	≥99%	Sigma Aldrich
Fumed silica powder		Sigma Aldrich
Gallium (III) oxide	≥99.99%	Sigma Aldrich
Gallium trinitrate hydrate	99.90%	Sigma Aldrich
HMI	99%	Sigma Aldrich
Hydrochloric acid	37%	Sigma Aldrich
Pyridine anhydrous	≥99.8%	VWR Chemicals
Sodium aluminate		Sigma Aldrich
Sodium hydroxide	G.R.*	Lach:ner
Tetraethyl orthosilicate	98%	Sigma Aldrich
TPAOH, 40% weight suspension in H_2O		Sigma Aldrich
CTAB	High purity	Sigma Aldrich

3.2. Synthesis of MWW zeolites

The MCM-22 zeolite was synthesized hydrothermally according to Ref.[85] The synthesis gel was composed of distilled water, sodium aluminate (cation traces 50 – 55% Al_2O_3, and 40 – 45% Na_2O), sodium hydroxide, HMI and fumed silica. The gel was prepared with a composition of:

0.49 HMI : 0.09 Na_2O : SiO_2 : 0.033 Al_2O_3 : 43.9 H_2O

Sodium aluminate and sodium hydroxide were first dissolved in distilled water. Then, under continuous stirring, fumed silica was slowly added to the mixture followed by adding HMI. The crystallization was then conducted in a Teflon-lined steel autoclave at 150 °C for 7

days with rotation at 60 rpm. The product of this procedure, the layered precursor of **MWW** zeolite denoted Al-MCM-22P, was then recovered by filtration, washed well with distilled water and dried at 60 °C overnight. The dried product was then calcined at 550 °C for 6 hours, with a temperature ramp of 2 °C min^{-1}, under air flow to acquire an Al-MCM-22 zeolite. Finally, the product was ion-exchanged into NH_4^+ form by treating it four times with a solution of 1 M NH_4NO_3 (1 g of zeolite per 100 ml of a solution) for 4 hours at room temperature, followed by conversion into a proton form by calcination at 550 °C for 6 hours with a temperature increase of 2 °C min^{-1}. The obtained catalyst showing micron-size crystals was designated as Al-MWW (microcrystalline Al-substituted **MWW** zeolite).

The MCM-56 zeolite was synthesized hydrothermally according to Ref.[74] The synthesis gel was composed of distilled water, sodium aluminate (cation traces 50 – 55% Al_2O_3, and 40 – 45% Na_2O), sodium hydroxide, HMI and fumed silica. The gel was prepared with a composition of:

0.32 HMI : 0.096 Na_2O : SiO_2 : 0.038 Al_2O_3 : 16.9 H_2O

Crystallization was conducted in Teflon-lined steel autoclave at 143 °C for 33 hours under agitation and autogenous pressure. The product of this procedure was recovered by filtration, washed well with distilled water, and dried at 60 °C overnight. The dried product was heated in nitrogen at 482 °C for 3 hours, with a temperature ramp of 3 °C min^{-1}, then cooled to about 130 °C, and subsequently calcined under air flow at 540 °C for 6 hours with a temperature ramp of 2 °C min^{-1} to acquire an Al-MCM-56 zeolite. Finally, the product was ion-exchanged into NH_4^+ form by treating it four times with a solution of 1 M NH_4NO_3 (1 g of zeolite per 100 ml of a solution) for 4 hours at room temperature, followed by conversion into a proton form by calcination at 550 °C for 6 hours with a temperature increase of 2 °C min^{-1}. The obtained catalyst was designated as NL-Al-MWW (nanolayered Al-substituted **MWW** zeolite).

3.3. Synthesis of MFI zeolites

Al-containing microcrystalline **MFI** zeolite (Al-MFI) was synthesized according to Ref.[86] with Si/Al in reaction mixture 40 using tetrapropylammonium hydroxide as SDA. Nanosponge **MFI** (NS-Al-MFI) was prepared using $C_{22}H_{45}$-$N^+(CH_3)_2$-C_6H_{12}-$N^+(CH_3)_2$-C_6H_{13}]$(Br^-)_2$ as SDA, as described in Ref.[87], while Al-containing nanolayer **MFI** (NL-Al-MFI) was synthesized using the same SDA according to Ref.[28] Finally, two pillared **MFI** (PI-Al-MFI-550 and PI-Al-MFI-800) were synthesized according to Ref.[28] with the same SDA,

followed by a pillaring procedure using TEOS. These two pillared samples were calcined at two different temperatures, 550 °C for PI-Al-MFI-550 and 800 °C for PI-Al-MFI-800.

All Ga-containing analogues (e.g., Ga-MFI, NS-Ga-MFI, NL-Ga-MFI) were synthesized according to the same synthesis protocols as Al-containing samples, albeit replacing a source of Al with equivalent amount of the source of Ga (gallium nitrate, Sigma Aldrich). Mesoporous Al- and Ga-MFI (Meso-Al-MFI and Meso-Ga-MFI) were prepared by desilication of corresponding **MFI** samples according to Ref.[88]

3.4. Characterization of zeolite catalysts

Structure and phase purity were confirmed by X-ray diffraction measurement, using a Bruker D8 Advanced Diffractometer, equipped with a Linxeye XE-T detector and CuKα (1.5406 Å) radiation. Analysed samples were gently grinded and placed into a holder to prevent preferential orientation of individual crystals.

The textural properties were measured by nitrogen adsorption and desorption. Adsorption / desorption isotherm measurements were performed on a Micrometrics 3Flex volumetric surface area analyser at -195.85 °C. The specific surface area (S_{BET}) was calculated using the BET method[89] from adsorption data in the range of relative pressure p/p_0 = 0.05 – 0.20. The micropore volume (V_{mic}), the mesopore volume (V_{meso}), and the external surface area (S_{ext}) were calculated by the t-plot method.[90] The total volume (V_{tot}) of the adsorbed amount was determined at a high relative pressure p/p_0 = 0.95.

The Ga/Si and Al/Si ratios of the zeolites were determined using ICP-MS analysis (Agilent 7900 ICP-MS, Agilent technologies, Inc., USA). Approximately 50 mg of the sample was mixed with 1.8 ml of HNO_3, 5.4 ml of HCl and 1.8 ml of HF and then transferred to a closed Teflon vessel, placed in a microwave (Speedwave® XPERT, Berghof) and heated at 210 °C (5 °C/min) for 25 min. After cooling, the complexation of the surplus HF was performed by adding 12 ml of H_3BO_3 and further treatment heating in the microwave at 190 °C (5 °C/min) for 10 min. The resulting solutions were cooled and diluted for analysis.

The morphology of zeolite crystals was imaged using a JSM-5500LV (JEOL) SEM microscope.

Scanning transmission electron microscopy (STEM) measurements were performed using a JEOL JEM NEOARM-200F microscope with a Schottky-type field emission gun at an accelerating voltage of 200 kV. The samples were prepared by direct deposition on a

copper holey carbon TEM grid. Images were collected in scanning mode using JEOL annular dark-field and bright-field detectors.

3.5. FTIR experiment

FTIR spectroscopic experiments were conducted to investigate the strength, nature, and accessibility of acid sites in zeolite catalysts.

Set-up

Measurements were made at room temperatures using Nicolet 6700 FT-IR spectrometer with DTGS detector and potassium bromide interferometer (**1**, Figure 20). The measurement quartz cell is composed of two parts: 1) nonheated part with 2 KBr IR transparent windows, which is where the sample is placed during the measurement (**2**, Figure 20), and 2) a heated part (**3**, Figure 20) used for thermal treatment of the sample (activation, thermal desorption). The measurement cell was connected to a vacuum line (**4**, Figure 20). An oil vacuum pump (Pfeiffer Vacuum) was used to reach the pressure >13 Pa in the set-up, while turbomolecular pump (Pfeiffer vacuum) allowed us to outgas the cell to the pressure of around 0.013 Pa. The pressure achieved in distinct parts of the apparatus was monitored by three pressure meters (**5a-c**, Figure 20) connected to the Maxi Gauge station (all Pfeiffer Vacuum CMR with measurement range from 1×10^{-3} hPa to 11 hPa with precision of 0.2%).

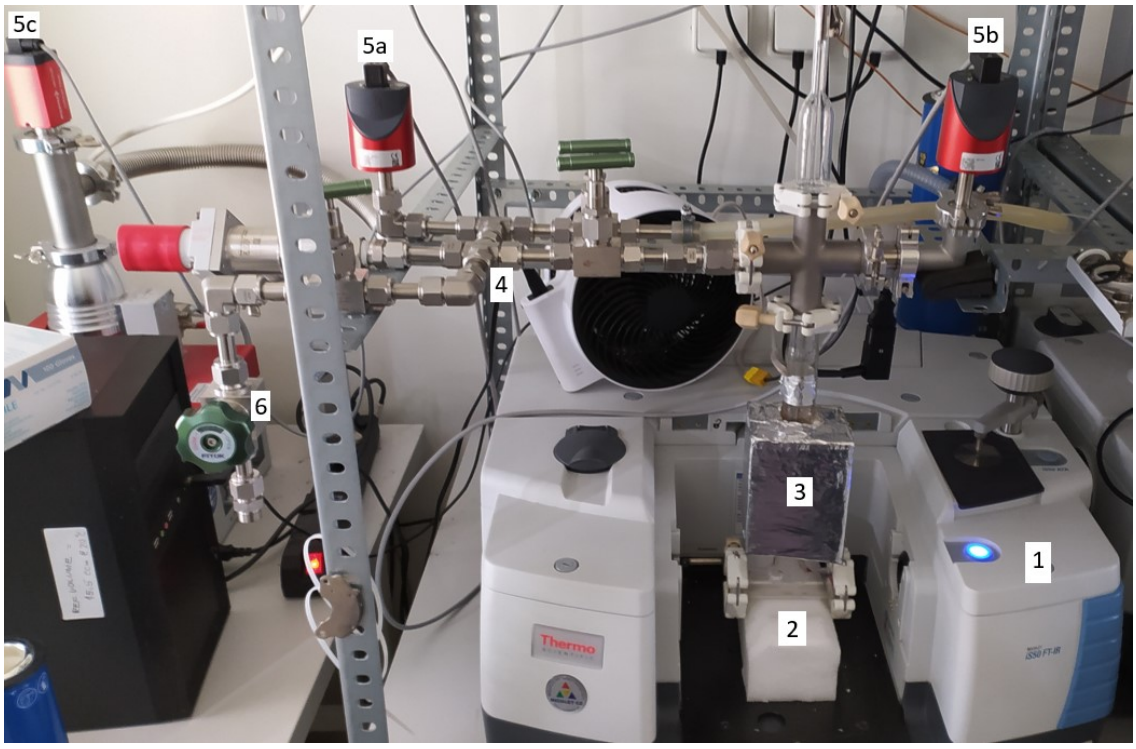

Figure 20: FTIR setup, 1) FTIR spectrometer; 2) measurement cell; 3) heated part of the measurement cell connected to the oven and a thermocontroller 4) vacuum line; 5a, 5b, 5c) pressure meters; 6) inlet for probe molecules.

Sample preparation

All samples were prepared as self-supporting wafers. 20 – 40 mg of the zeolite sample was first homogenized by grinding and then uniformly distributed on a rectangular metal base of the press-form (3×1 cm). The sample was pressed for at least 1 minute with a maximum force of 30 kN. After that, the press form was disassembled, and the sample was taken as a self-supporting wafer. A razor blade is then used to cut any part of the wafer that has cracks in it. The minimum area of the wafer usable for measurement was 1.2 cm^2.

Before each measurement, all wafers were activated in the heated part of a measurement cell (**3**, Figure 20). Activation of all zeolite samples was performed under high vacuum (pressure less than 0.0133 Pa), temperature 450 °C for 4 hours with a ramp of 5 °C per minute. After cooling down, the background was measured (done before each measurement) and the sample was moved to the bottom part of the measuring cell to gain its spectra. All measurements were done in the range of 4000 to 400 cm^{-1} with the resolution of 4 cm^{-1} by collecting 128 scans.

Adsorption of probe molecules, monitored by FTIR spectroscopy

For my measurements, two different probe molecules were used. Pyridine with a kinetic diameter of 0.54 nm was used to identify the nature, strength, and total concentration of the acid sites in zeolites. 2,6-Di-tert-butylpyridine with a kinetic diameter of 0.79 nm was used to measure the accessibility of acid sites.[32, 91]

All measurements were performed using this procedure: The wafer was prepared, placed in the holder, and activated according to the chosen activation program. The probe molecule (pyridine or 2,6-Di-tert-butylpyridine) in a round flask was degassed by freezing, pump, and thaw cycles using liquid nitrogen. Spectra were taken before any adsorption. Then, the probe molecule was adsorbed for 20 minutes at 150 °C at 466 or 13 Pa for pyridine and 2,6-Di-tert-butylpyridine, respectively. This was followed by desorption steps at 150, 250, 350, and 450 °C for 20 minutes, where after each desorption step, the spectra were measured.

The nature of the acid sites was identified by adsorbing pyridine and locating their characteristic bands in the spectra, 1545 cm^{-1} for BAS and 1455 cm^{-1} for LAS.[61] The concentration of both BAS and LAS was determined by integrating their IR band areas using Beer-Lambert law. The molar absorption coefficients used for the calculation of the acid site concentration were 1.67 cm/μmol for BAS and 2.22 cm/μmol for LAS.[92] The acid site strength was determined by thermodesorption of pyridine. The relative intensity of the bands

for BAS and LAS at 350 °C with respect to those at 150 °C was used as a measure of acid strength. Then, the concentration of BAS accessible for 2,6-di-tert-butylpyridine was determined according to Ref.[91] The characteristic band of BAS with adsorbed 2,6-di-tert-butylpyridine has a wavenumber of 1615 cm^{-1} and its molar absorption coefficient used for concentration calculation was 5.3 cm/μmol.[91] The ratio of acid sites accessible to 2,6-di-tert-butylpyridine and pyridine was used as a measure of acid site accessibility.

3.6. Catalytic experiment

The catalytic performance of **MFI** and **MWW** zeolite catalysts was studied in the PFC reaction. According to previous studies[70], all reactions were performed in a multi-experiment workstation Starfish (Radleys Discovery Technologies) under mild conditions at the temperature 60 °C. Before the reaction, the zeolites were activated at 450 °C for 5 hours with a ramp of 2 °C/min. All reactions were conducted in a 25 ml glass flask by weighing in 50 mg of activated catalyst, adding 10 ml of anisole (solvent + reactant), 0.2 g of dodecane (internal standard), and 2.5 mmol of butyraldehyde. The three-necked flask containing this mixture was put into the Starfish workstation and then connected to a condenser and a thermometer. After the solution reached 60 °C sample 0 was taken and then 5 mmol of 3-buten-1-ol of butyraldehyde was added to start the reaction. Samples of this reaction mixture were taken periodically after 10, 20, 30, 40 minutes, 1, 2, 4, 6, and 24 hours, and then analysed using Agilent 8860 GC equipped with Agilent HP-5 column (length 30 m, diameter 0.32 mm, and film thickness 0.25 μm). The conditions used for the measurements were as follows: V_{H2} = 40 ml/min, V_{air} = 450 ml/min, V_{N2} = 25 ml/min, $T_{detector}$ = 250 °C, $T_{injector}$ = 250 °C. Program of the oven: 4 minutes at T = 60 °C, then temperature increases until T = 300 °C on a ramp of 30 °C/min, and this temperature was held for 5 minutes. Analysis of a single sample took 17 minutes and volume taken for a single sample was 1 μl. The butyraldehyde response factor (R_f = 1.787) was determined by calibration with the internal standard and then used to calculate the amount of substrate (Equation 7).

$$n_{ald} = \frac{n_{is} A_{ald}}{R_f A_{is}} \quad (7)$$

Where n_{ald} is the molar amount of butyraldehyde [mol]; n_{is} is the molar amount of dodecane [mol]; A_{ald} is the GC measured peak area of aldehyde; and A_{is} is the GC measured peak area of dodecane; R_f is the response factor of butyraldehyde.

Conversion of butyraldehyde (Equation 8) and selectivity to the targeted products (Equation 9) was calculated by the following formulas:

$$Conversion\ [\%] = \frac{n_0 - n_t}{n_0} \cdot 100 \tag{8}$$

$$Selectivity\ [\%] = \frac{n(product)_\tau}{n_0 - n_t} \cdot 100 \tag{9}$$

Where n_0 is the initial molar amount of butyraldehyde [mol]; n_t is the molar amount of butyraldehyde remaining at a chosen time [mol]; $n(product)_\tau$ is an amount of a product formed in reaction mixture after time τ [mol].

The activity of zeolite catalyst was assessed by their initial reaction rate per acid site. The initial reaction rate was calculated as a slope to the graph of products **1**+**2** (Figure 19) concentration against the reaction time at t = 0 (Figure 21) and then normalized to the total concentration of BAS and LAS determined using FTIR spectroscopy of adsorbed pyridine.

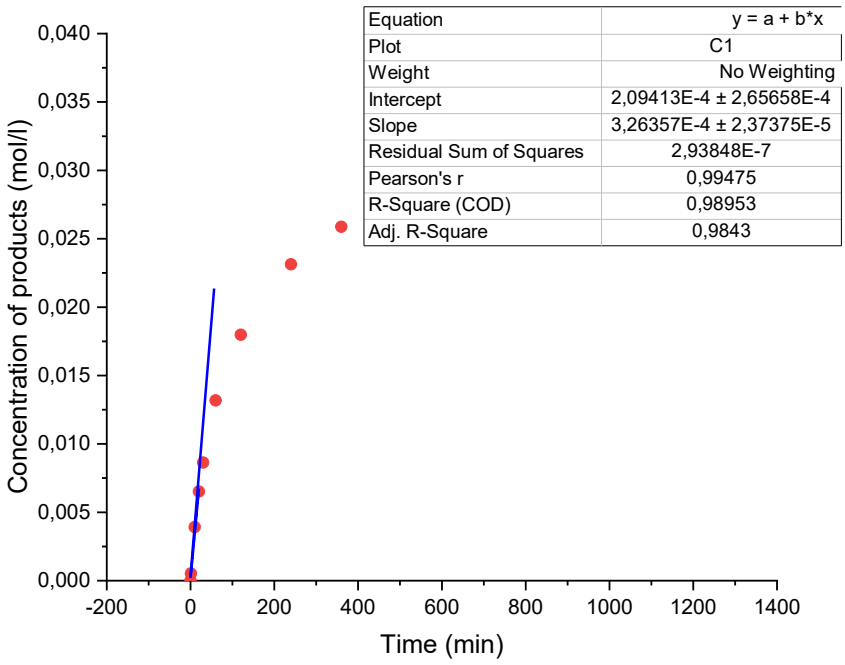

Figure 21: Dependence of product concentration on time for the NL-Al-MFI catalyst. Calculation of the initial reaction rate as a slope to the *c vs. t* graph.

4. Results and discussion

4.1. Characteristics of MFI and MWW zeolites

4.1.1. Structural and textural properties

The structural and textural properties of **MFI** and **MWW** zeolites prepared using different synthesis protocols were analysed by X-ray diffraction (Figures 22a-c), electron microscopy (Figures 23 and 24), and N_2 physisorption (Figures 25a-c). The XRD patterns of the **MFI** zeolites (Figures 22a-b) contain characteristic peaks at 2θ = 7.9° (011), 8.8° (020), 8.9° (200), 9.14° (111), 23.06° (051), 23.98° (033), 24.62° (313), and others, corresponding to the reference pattern of Ref.[5], while showing no additional diffraction lines. This proves the **MFI** structure of the zeolites and their phase purity. For the PI-Al-MFI samples (Figure 22a), an additional peak can be observed at 1.5°. This low-angle diffraction line is attributed to the long-range ordering of **MFI** zeolite crystalline layers in pillared materials with d-spacing at 5.9 nm, as reported in Ref.[28]

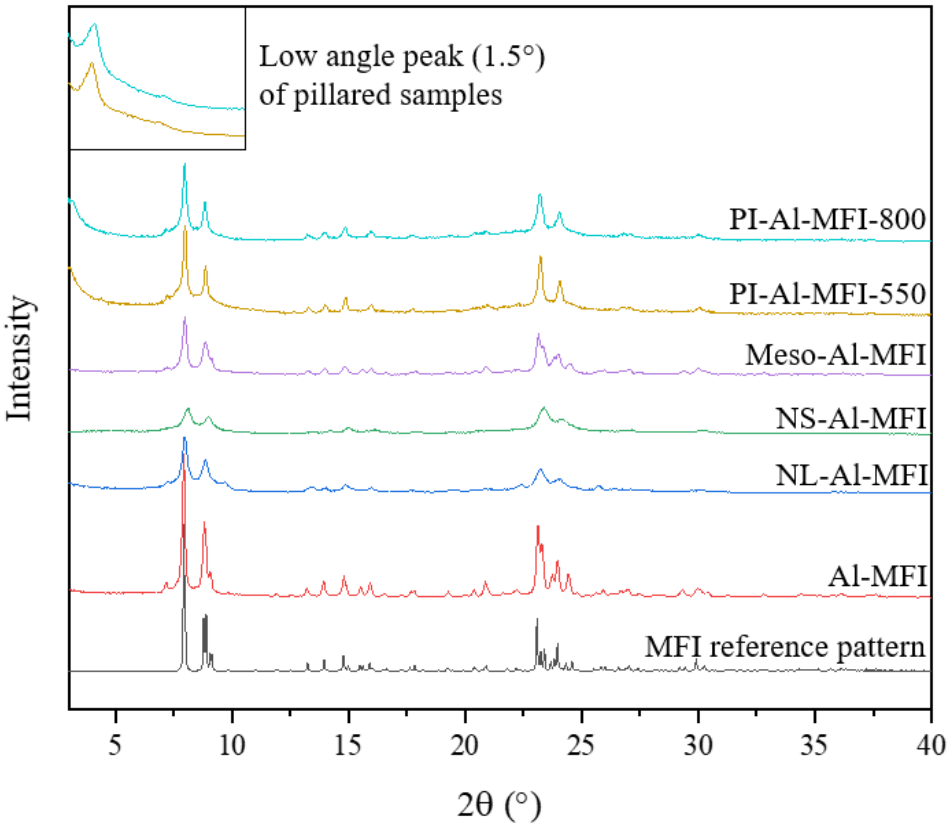

Figure 22a: Powder X-ray diffraction patterns of Al- containing **MFI** zeolites with different crystal morphologies.

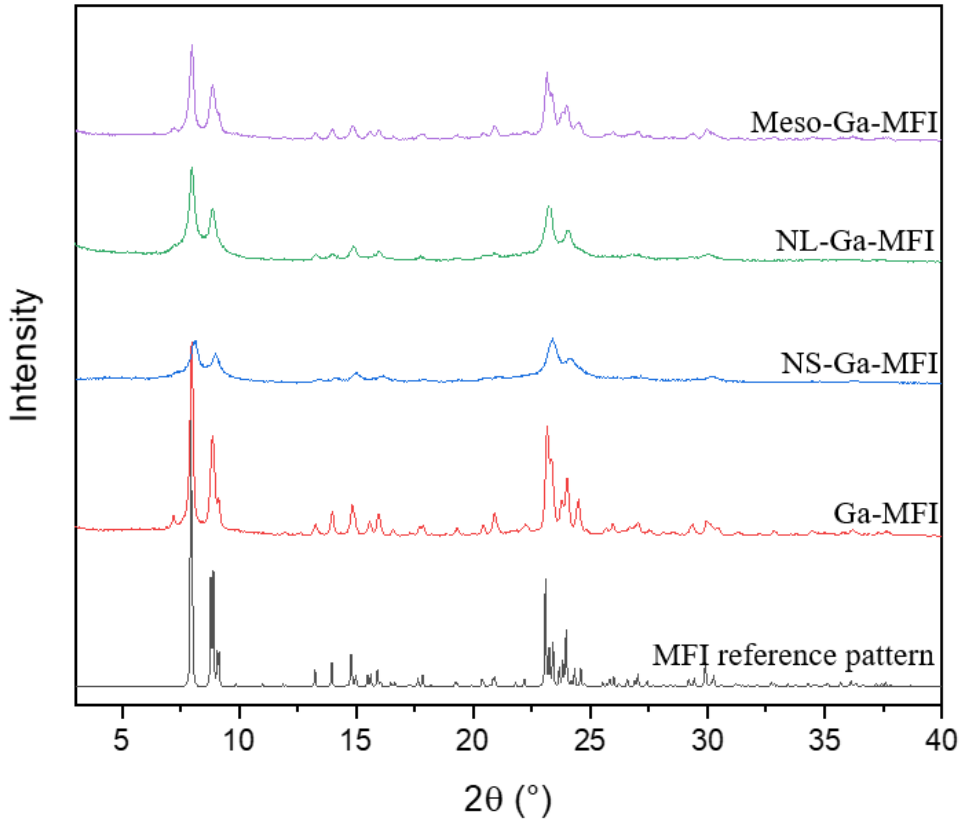

Figure 22b: Powder X-ray diffraction patterns of Ga- containing **MFI** zeolites with different crystal morphologies.

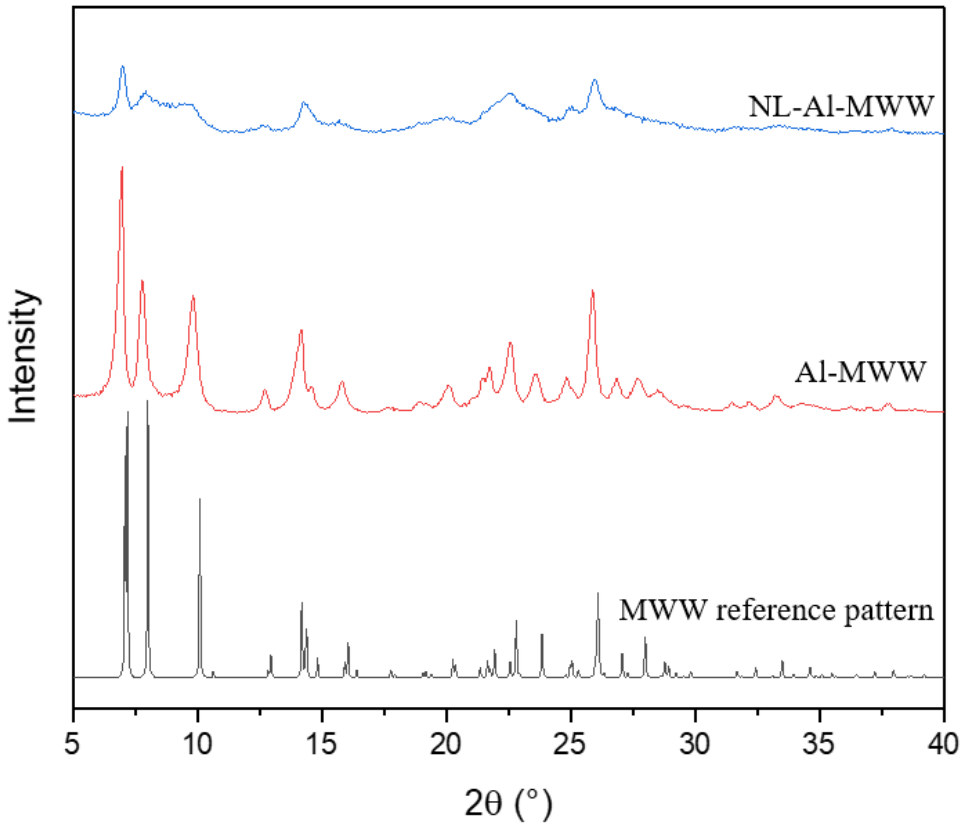

Figure 22c: Powder X-ray diffraction patterns of Al- containing **MWW** zeolites with different crystal morphologies.

A broadening of the diffraction lines observed for nanolayered NL-MFI, mesoporous Meso-MFI, and nanosponge NS-MFI zeolites reveals a decrease in the crystallite sizes in the sequence MFI > Meso-MFI > NL-MFI > NS-MFI, as suggested by the Scherrer equation[93] (Equation 10)

$$FWHM = \frac{(k \cdot \lambda)}{(D \cdot \cos\theta)} \quad (10)$$

where *FWHM* is the full width at half-maximum of the diffraction peak, k is a shape constant, λ is the wavelength, D is the crystallite size and θ is the Bragg angle.

The XRD pattern of Al-MWW zeolite (Figure 22c) is in accordance with the reference diffractogram from the IZA database.[5] The diffraction pattern of Al-MWW shows characteristic peaks at 2θ = 7.1° (100), 8.00° (101), 10.12° (102), 14.18° (004), 22.78° (302), 26.02° (107) and others. For MCM-56 (abbreviated in this work as NL-Al-MWW to stress the nanolayered morphology of the crystals), the characteristic broad diffraction lines in the range of 7.4 –11° can be observed, while other peaks become broader and show a lower intensity compared to Al-MWW. This is caused by the distortion of long-range order between the **MWW** layers in NL-Al-MWW, as reported in Ref.[74] The absence of additional peaks confirms the phase purity of **MWW** samples.

The morphology of the zeolite catalysts was analysed using scanning electron microscopy (Figures 23a-c). Samples of conventional **MFI** and Meso-MFI zeolites, both Al- and Ga-containing, form micrometre-sized crystals. The nanolayered NL-Al-MFI forms plate-like particles of around 50 nm thickness (Figure 24). The nanosponge NS-Al-MFI is made up of randomly connected zeolite layers (Figure 24). SEM images of Al-MWW and NL-Al-MWW show thin plate-like particles intergrown to form large aggregates of the size of several microns (Figure 23c).

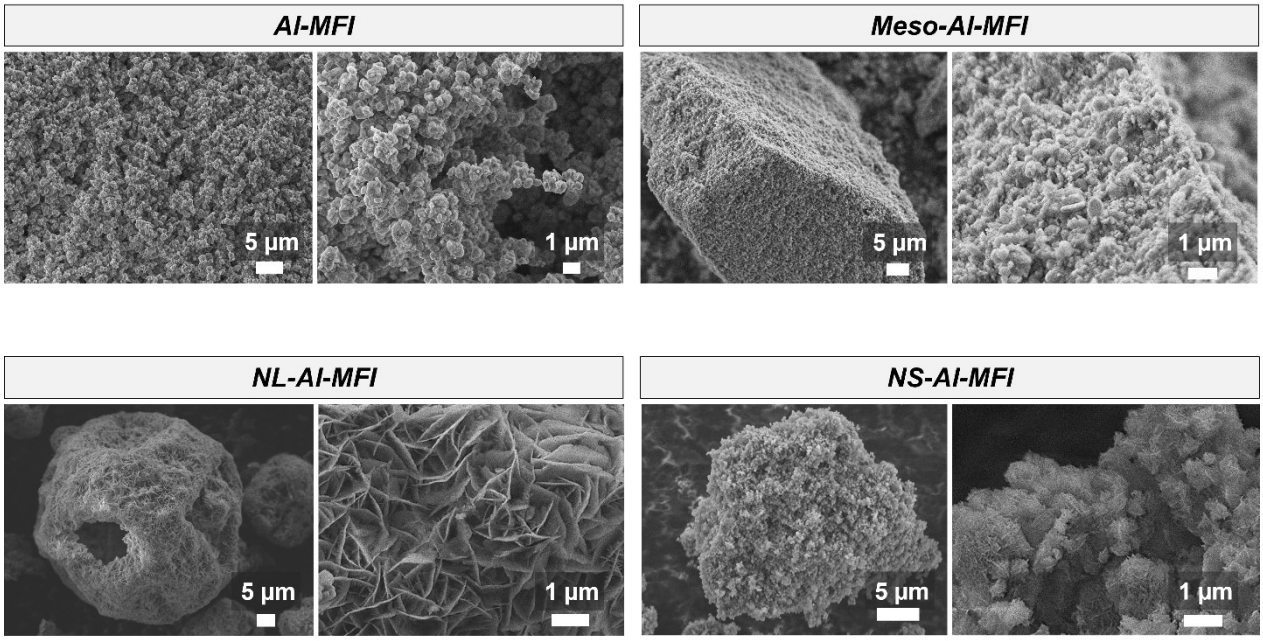

Figure 23a: SEM images of Al-containing **MFI** zeolites.

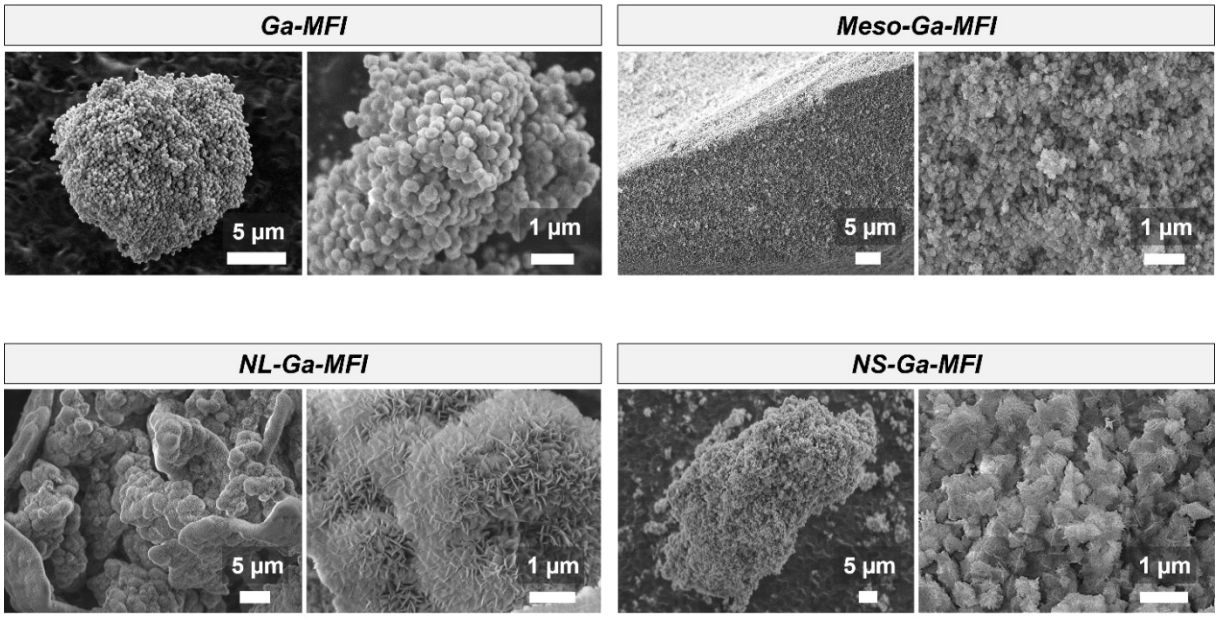

Figure 23b: SEM images of Ga-containing **MFI** zeolites

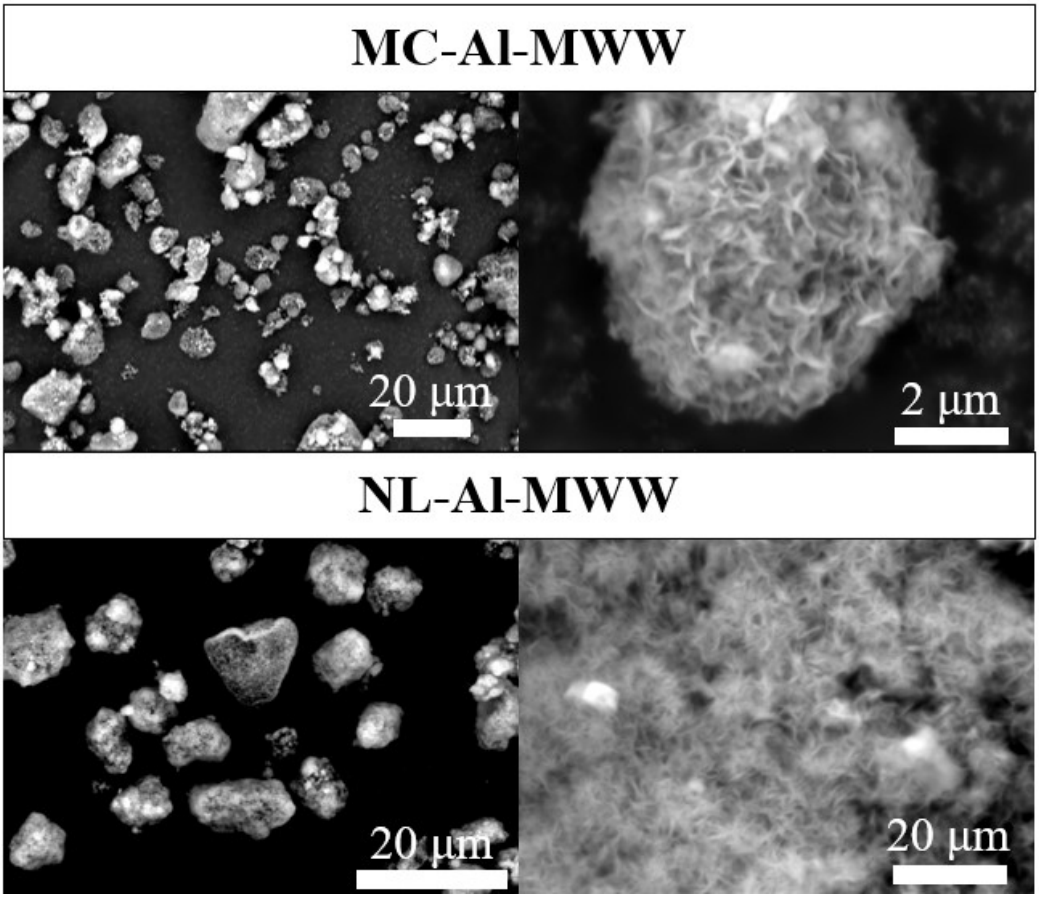

Figure 23c: SEM images of Al-containing **MWW** zeolites.

The TEM images of mesoporous Meso-Al-MFI show multiple intracrystalline mesopores in the zeolite crystal. The images also verify the microcrystalline, nanolayered, and nanosponge morphologies of Al-MFI, NL- and NS-Al-MFI, respectively (Figure 24).

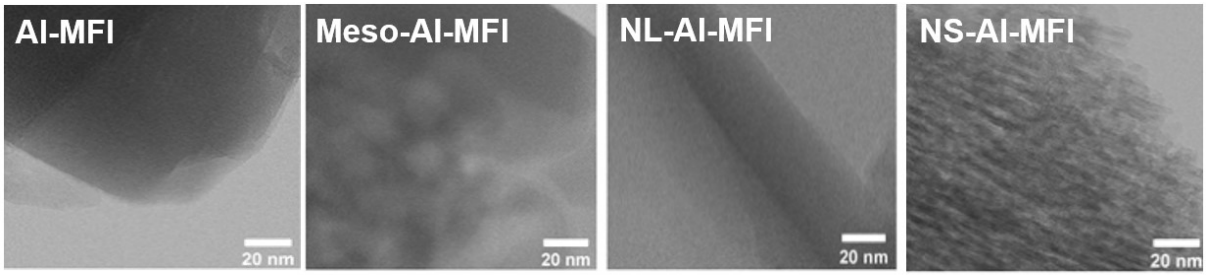

Figure 24: TEM images of the Al-MFI zeolites under study.

Textural properties of the zeolites were investigated by nitrogen adsorption (Figure 25a-c). A steep increase in the volume of adsorbed nitrogen was observed at low pressure $p/p_0 < 0.01$ for all the samples. This refers to the filling of the zeolites micropores. With an increase in $p/p_0 > 0.01$, the adsorbed volume remains almost constant for the microcrystalline Al-MFI and Ga-MFI zeolites but increases for other zeolites studied. Thus, both Al- and Ga-containing conventional MFI zeolites show a type I isotherm, as expected for a purely

microporous material. The NL-, NS- and Meso- zeolites show a combined I+IV type isotherm, which is characteristic of hierarchical micro-mesoporous materials. The isotherms of hierarchical zeolites have a pronounced hysteresis loop (Figure 25), which is related to the different mechanisms of adsorption and desorption in mesopores. Based on the pore size distribution curves, NL- and Meso-MFI zeolites contained pores that are up to 30 nm wide, while the pore size of NS-MFI reaches up to 20 nm. The micropore volumes of the **MFI** and **MWW** zeolites varied in the ranges 0.06 – 0.14 cm^3/g and 0.10 – 0.16 cm^3/g, respectively (Table 3). The mesopore volume increased in the following sequence of MFI samples: MFI < Meso-MFI (0.16 – 0.26 cm^3/g) < NL-MFI (0.22 – 0.33 cm^3/g) < NS-MFI (0.56 – 0.63 cm^3/g). An important feature of the NS-MFI zeolites, both Al- and Ga-containing ones, is the developed external surface of ~300 m^2/g, which is 1.5 – 2 times higher when compared to other MFI samples (Table 3). NL-Al-MWW zeolite showed a two-fold higher mesopore volume than conventional Al-MWW (0.38 *vs.* 0.19 cm^3/g, Table 3), while the differences in the external surface of both samples were less pronounced (175 *vs.* 110 m^2/g). Relatively high external surface of conventional Al-MWW can be attributed to morphology of its crystals composed of thin platelets, similarly to NL-Al-MWW (Figure 23c).

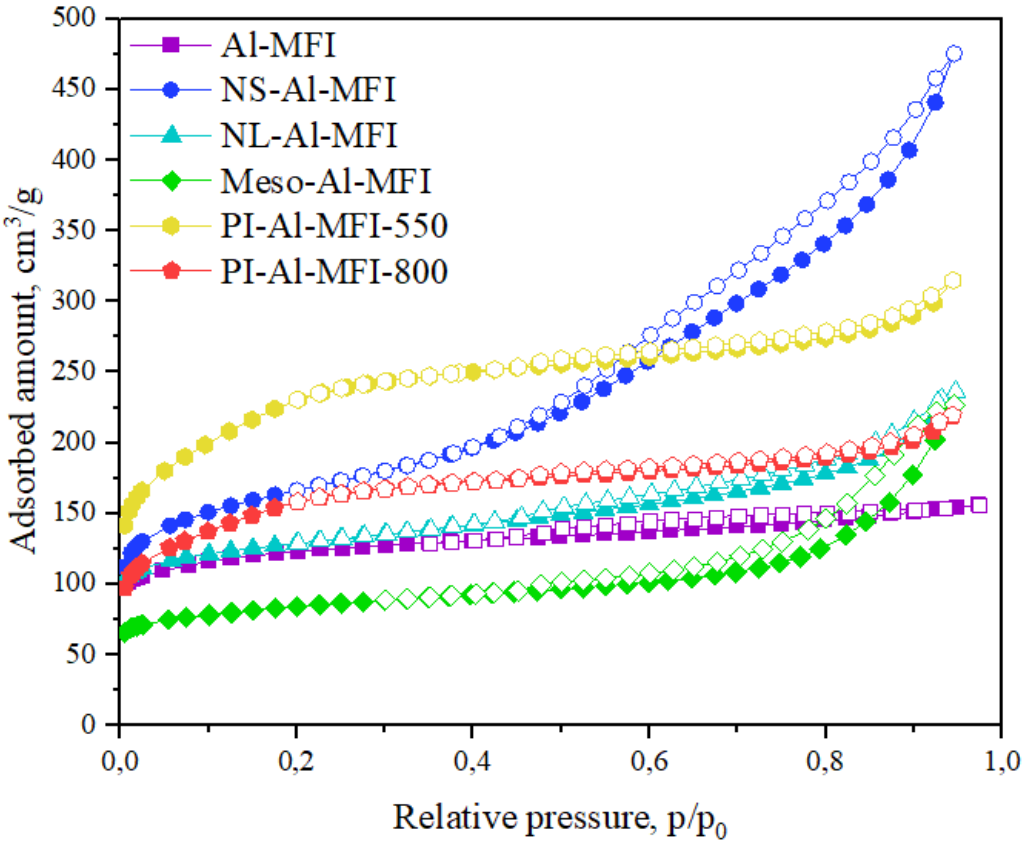

Figure 25a: Ad-/desorption isotherms of Al-containing **MFI** zeolites with different textural properties.

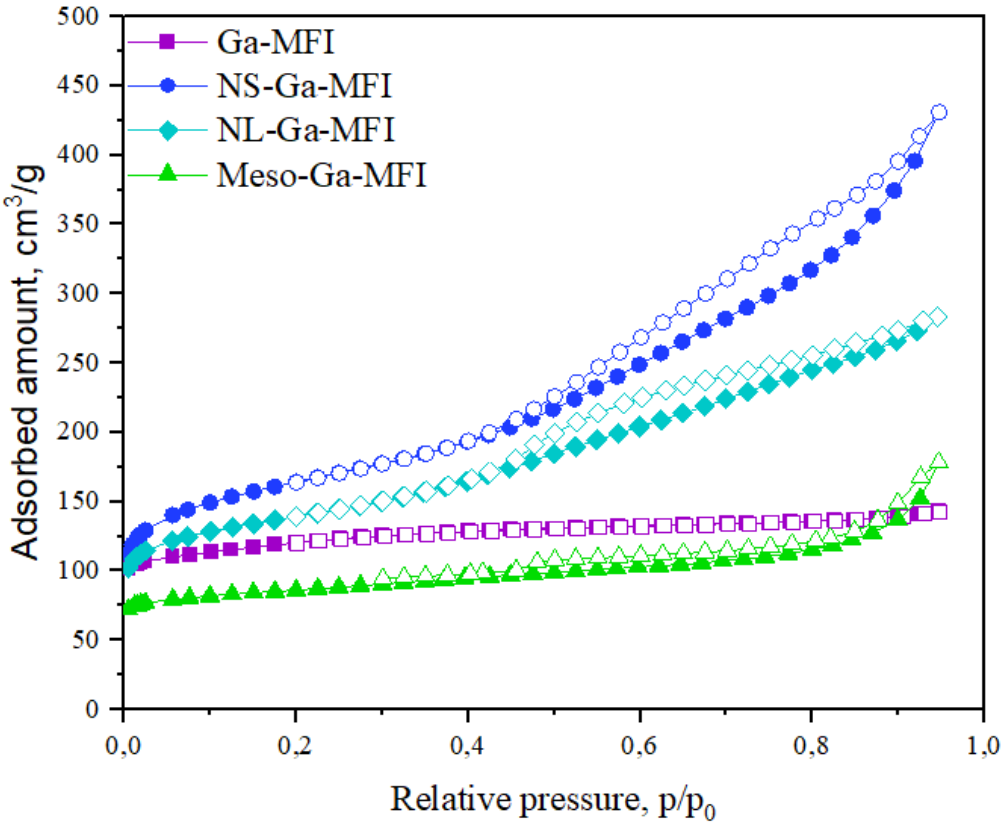

Figure 25b: Ad-/desorption isotherms of Ga-containing **MFI** zeolites with different textural properties.

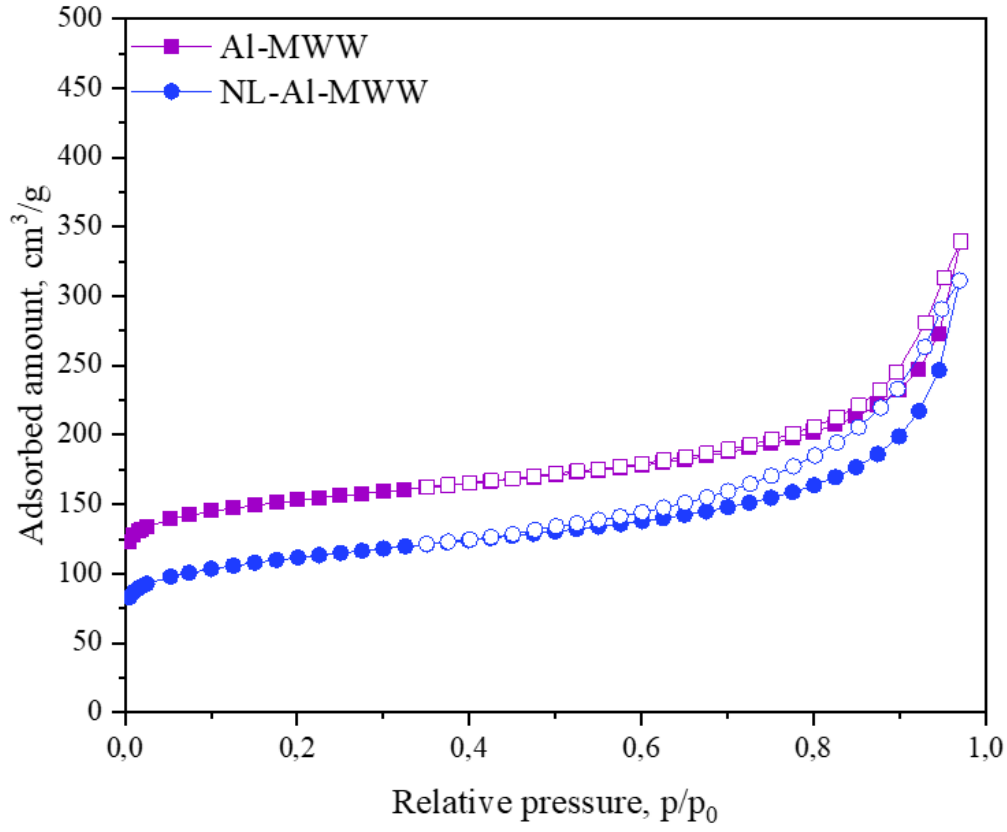

Figure 25c: Ad-/desorption isotherms of Al-containing **MWW** zeolites with different textural properties.

Table 3: Textural properties of **MFI** and **MWW** zeolites measured by nitrogen adsorption.

Zeolite	Si/T	Average mesopore diameter [nm]	S_{ext} [m^2/g]	V_{mic} [cm^3/g]	V_{meso} [cm^3/g]
Al-MFI	37	–	115	0.14	--
NS-Al-MFI	38	6.2	337	0.11	0.63
NL-Al-MFI	23	6.5	159	0.13	0.22
Meso-Al-MFI	24	10.2	121	0.08	0.26
Al-MWW	24	14.4	110	0.16	0.19
NL-Al-MWW	9	11.4	175	0.10	0.38
Ga-MFI	70	–	144	0.12	--
NS-Ga-MFI	40	6.7	323	0.11	0.56
NL-Ga-MFI	25	4.8	246	0.11	0.33
Meso-Ga-MFI	39	9.2	99	0.09	0.16
PI-Al-MFI-550	120	4.7	77	0.06	0.19
PI-Al-MFI-800	117	4.7	85	0.10	0.14

Chemical analysis revealed Si/Al ratios in Al-substituted MFI zeolites and Al-MWW were in the ranges 24 – 38 (Table 3), while the Ga-substituted MFI catalysts showed Si/Ga ratios 25 – 70. NL-Al-MWW with the lowest Si/Al ratio at 9 is an intermediate-silica zeolite and all other used zeolites are classified as high-silica zeolites.

4.1.2. Acidic properties

The acidic properties of all zeolite samples were analysed by FTIR spectroscopy. The spectra of activated zeolites showed the characteristic bands of the terminal silanol groups (3745 cm^{-1}) and of the -Si-OH-T^{3+} bridging groups (3610 cm^{-1} or 3625 cm^{-1} for zeolites containing Al or Ga, respectively, Figure 26a-b). The band of terminal silanols had the highest intensity for NS-MFI zeolites with the largest external surface (Table 3). Noticeably, the intensity of the band of bridging OH groups in Ga-containing MFI zeolites was remarkably lower compared with Al-containing zeolites of the same morphology. This result reveals the lower number of BAS in Ga-containing *vs.* Al-containing MFI zeolites.

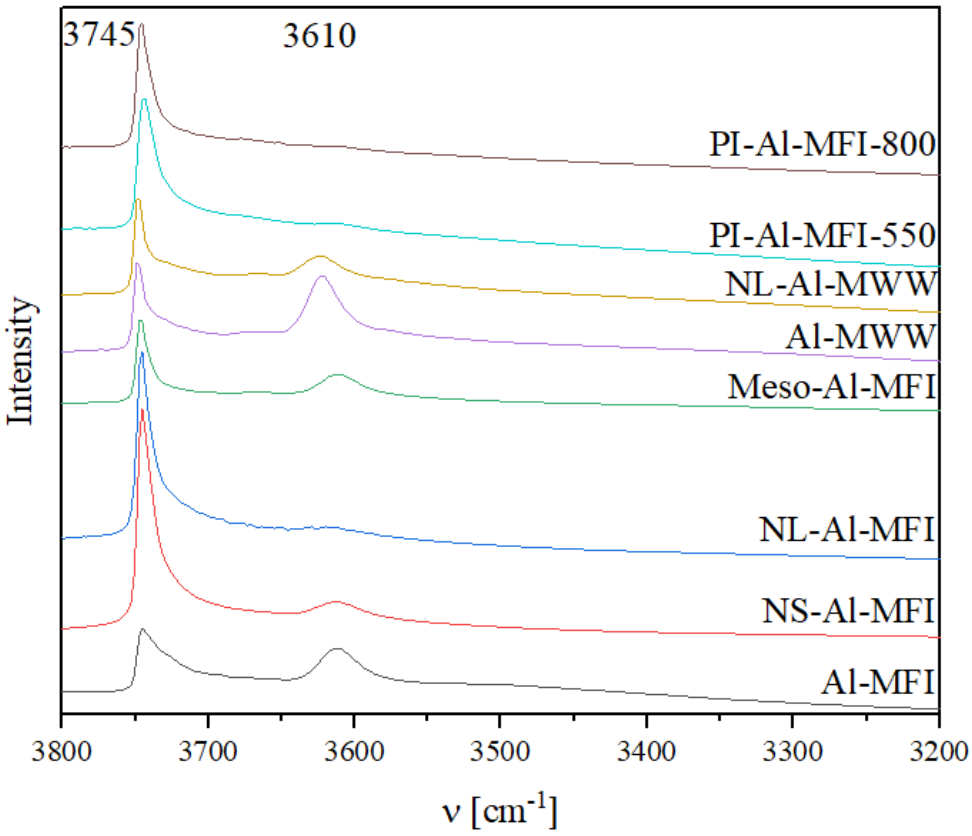

Figure 26a: FTIR spectra of activated Al-containing zeolite catalysts in the vibration region of OH groups.

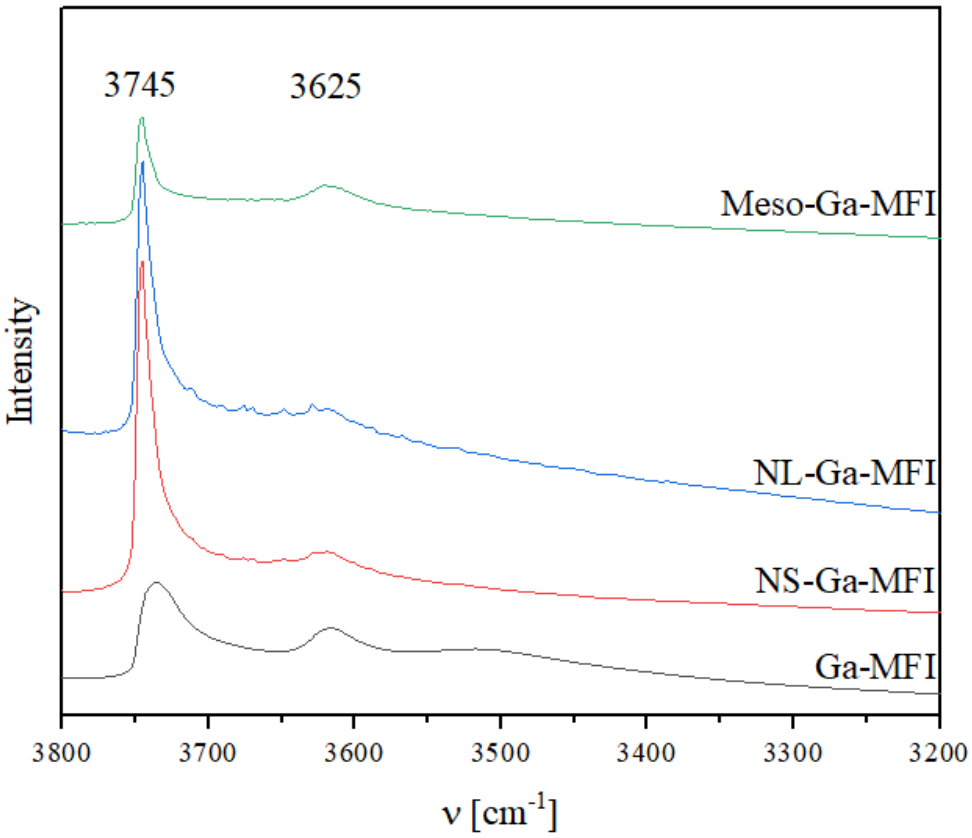

Figure 26b: FTIR spectra of activated Ga-containing zeolite catalysts in the vibration region of OH groups.

The nature and strength of the acid sites were determined using FTIR-monitored thermodesorption of adsorbed pyridine (Figure 27a-d). In the OH region of the spectra, it is important to note the disappearance of the BAS band (3610 cm^{-1} for Al- and 3625 cm^{-1} for Ga-containing zeolites) after the adsorption of pyridine (Figure 27a-b). This result proves the accessibility of all BAS for pyridine in both hierarchical and conventional zeolites. In the vibration region of the pyridine ring (Figure 27c-d), the appearance of the characteristic bands at 1545 cm^{-1} and 1455 cm^{-1} was associated with pyridine adsorbed on BAS and LAS, respectively.

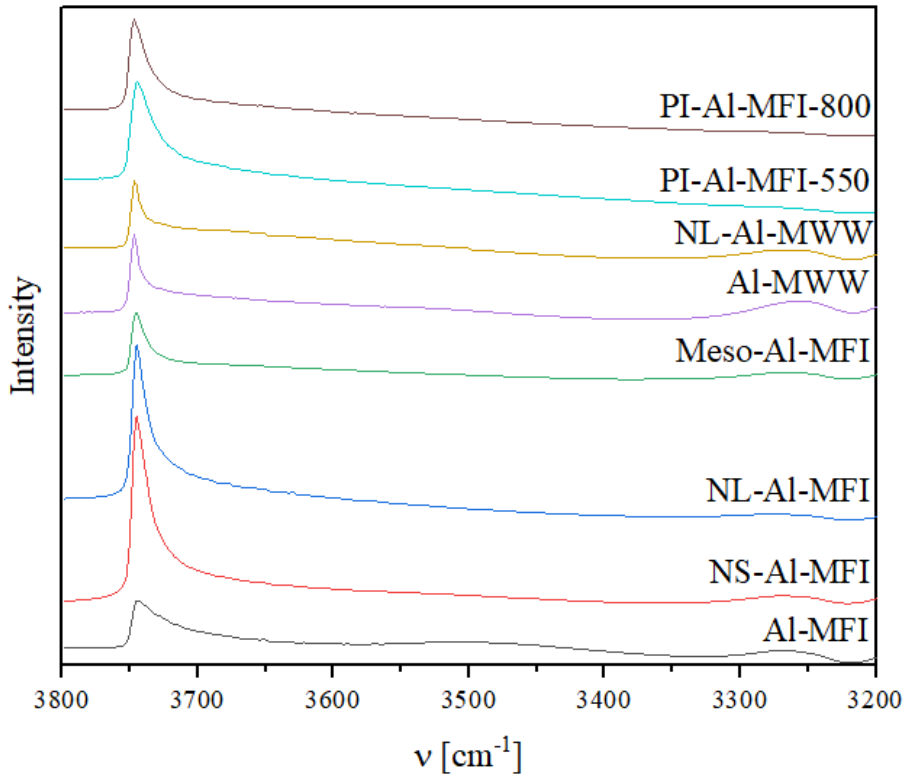

Figure 27a: FTIR spectra of Al-containing zeolites in the vibration region of OH groups after adsorption of pyridine at 150 °C.

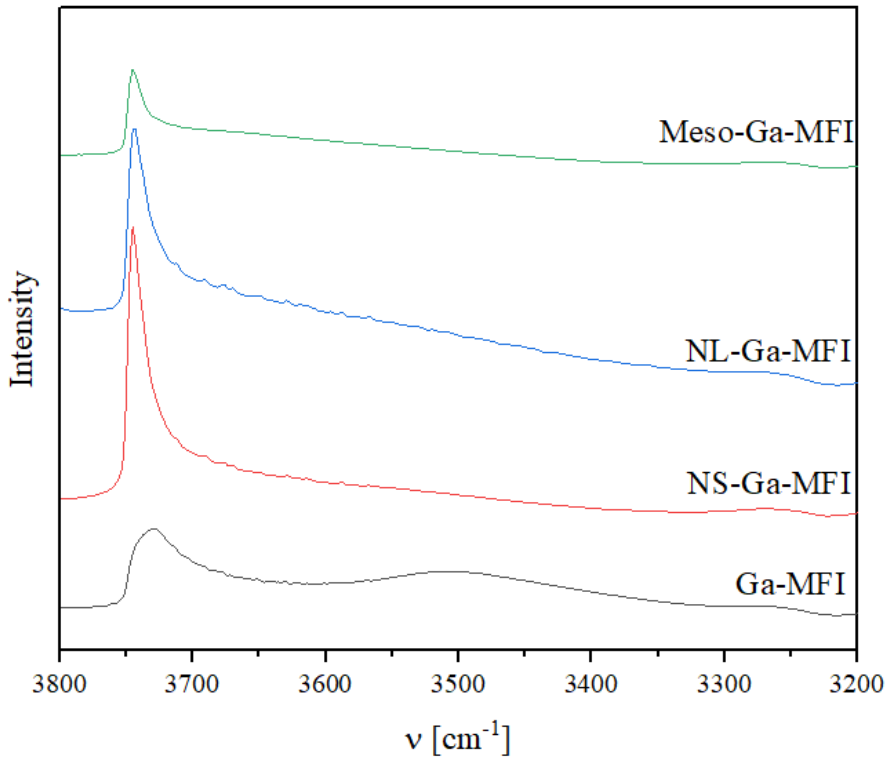

Figure 27b: FTIR spectra of the Ga-containing zeolites in the vibration region of OH groups after adsorption of pyridine at 150 °C.

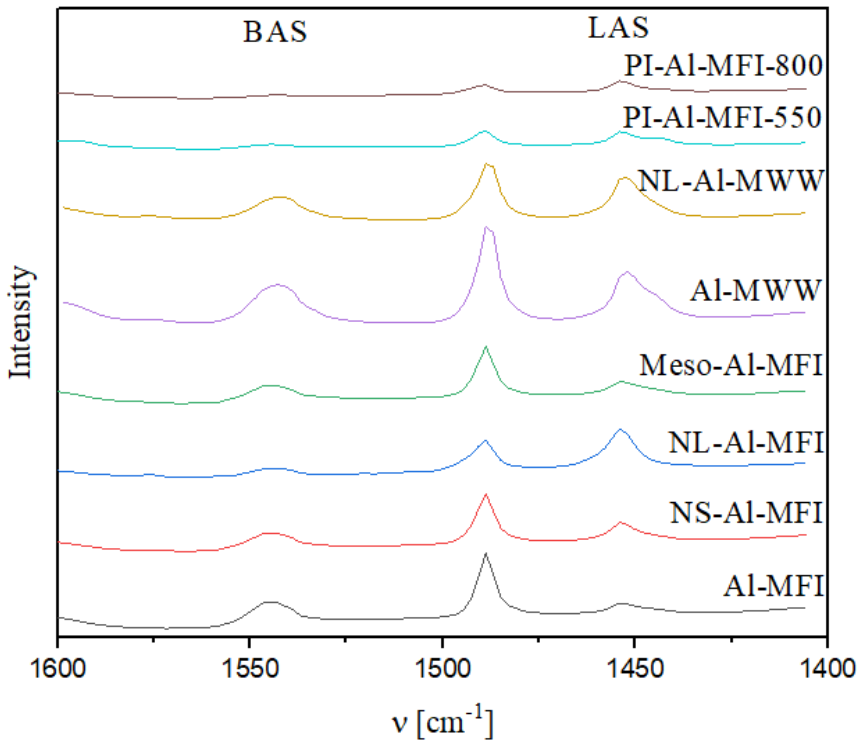

Figure 27c: FTIR spectra of Al-containing zeolites in the vibration region of the pyridine ring after adsorption of pyridine at 150 °C.

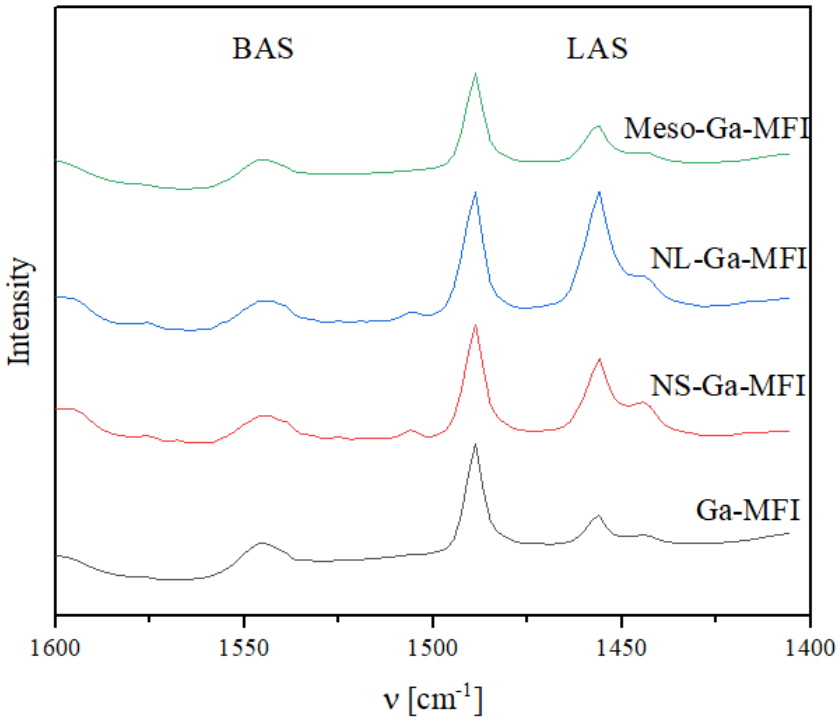

Figure 27d: FTIR spectra of the Ga-containing zeolites in the pyridine ring vibration region after adsorption of pyridine at 150 °C.

Table 4 and Figure 28 compare the concentrations of BAS and LAS evaluated based on the intensities of the diagnostic bands after ad-/desorption of pyridine in the catalysts at 150 °C. The fraction of strong acid sites in different zeolites is shown as the fraction of acid centres that keep adsorbed pyridine at 350 °C.

Table 4: Concentrations of LAS and BAS in zeolites determined by FTIR-monitored thermodesorption of pyridine.

	LAS		BAS		BAS+LAS	
Zeolite	concentration [mmol/g]	Fraction of strong sites [%]	concentration [mmol/g]	Fraction of strong sites [%]	c_L+c_B [mmol/g]	Fraction of strong sites [%]
Al-MFI	0.04	75	0.17	76	0.21	76
NS-Al-MFI	0.07	71	0.13	69	0.20	70
NL-Al-MFI	0.09	56	0.11	64	0.20	60
Meso-Al-MFI	0.06	50	0.13	69	0.19	63
PI-Al-MFI-550	0.04	71	0.04	62	0.08	68
PI-Al-MFI-800	0.05	65	0.03	-	0.08	41
Al-MWW	0.17	41	0.24	83	0.41	66
NL-Al-MWW	0.18	56	0.19	74	0.37	65
Ga-MFI	0.04	75	0.07	71	0.11	73
NS-Ga-MFI	0.12	42	0.07	57	0.19	47
NL-Ga-MFI	0.17	53	0.08	50	0.25	52
Meso-Ga-MFI	0.05	60	0.07	57	0.12	58

The notable trends are: 1) Ga- containing zeolites have a lower fraction of strong acid sites (47 – 73%) compared to their Al-containing counterparts (60 – 76%) (in agreement with the results reported in Ref.[12]); 2) Ga-containing zeolites have a lower fraction of BAS (32 – 63%) compared to Al-containing zeolites (55 – 81%); 3) for PI-Al-MFI, the calcination at higher temperature (800 °C) does not noticeably affected the total concentration of acid centres, but increased the LAS / BAS ratio (from 1 to 2).

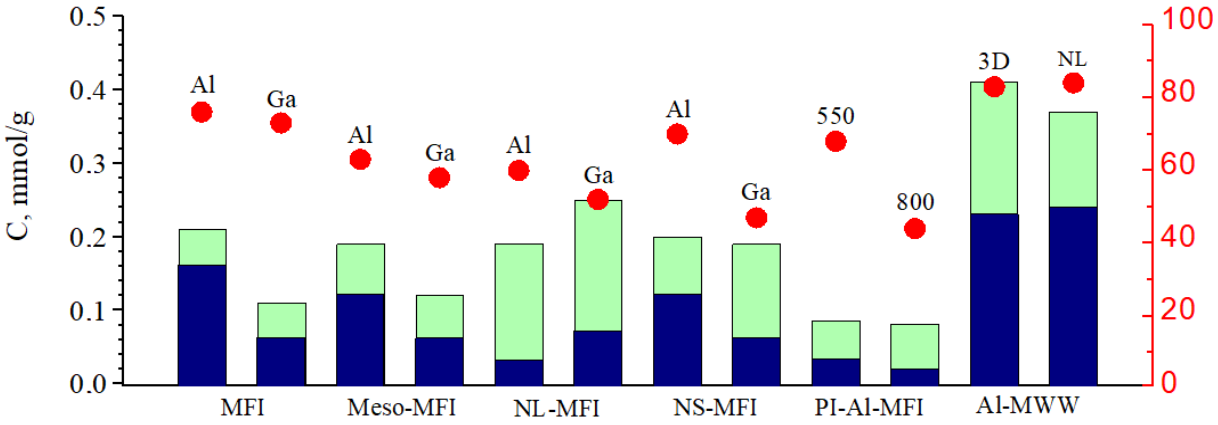

Figure 28: Concentration and strength of acid sites determined by FTIR-monitored thermodesorption of pyridine. The blue part of the column indicates the concentration of BAS. The light green part of the column shows the concentration of LAS. The red dots indicate the percentage of strong acid sites, shown on the right red axis.

The accessibility of Brønsted acid sites for the bulky molecules was evaluated using an FTIR-monitored adsorption of 2,6-di-tert-butylpyridine (Figure 29a-d). DTBP adsorption decreased but did not remove the characteristic absorption bands of the OH bridging groups (3610 cm^{-1} for Al- and 3625 cm^{-1} for Ga-containing zeolites) in the spectra of the studied zeolites (Figure 29a-b). This result revealed that only a part of BAS in zeolite catalysts was accessible for DTBP. In the region of DTBP ring vibrations, microcrystalline MFI zeolites show no bands, which revealed a lack of acid sites capable of interaction with the bulky base probe. In contrast to Ga- and Al-MFI, the spectra of hierarchical zeolites and of Al-MWW showed the characteristic band at 1615 cm^{-1}, assigned to $DTBP^{+}$ cation formed on BAS (Figure 29c-d).

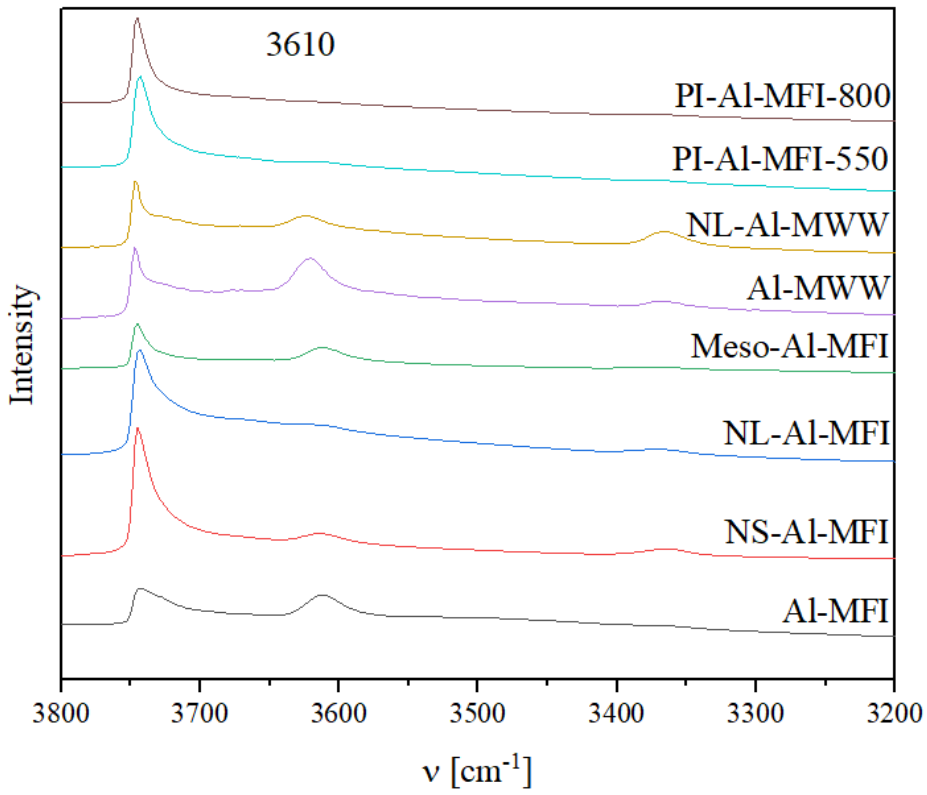

Figure 29a: FTIR spectra of Al-containing zeolites in the OH region after adsorption of 2,6-di-tert-butylpyridine at 150 °C. The BAS band at 3610 cm^{-1} is still present.

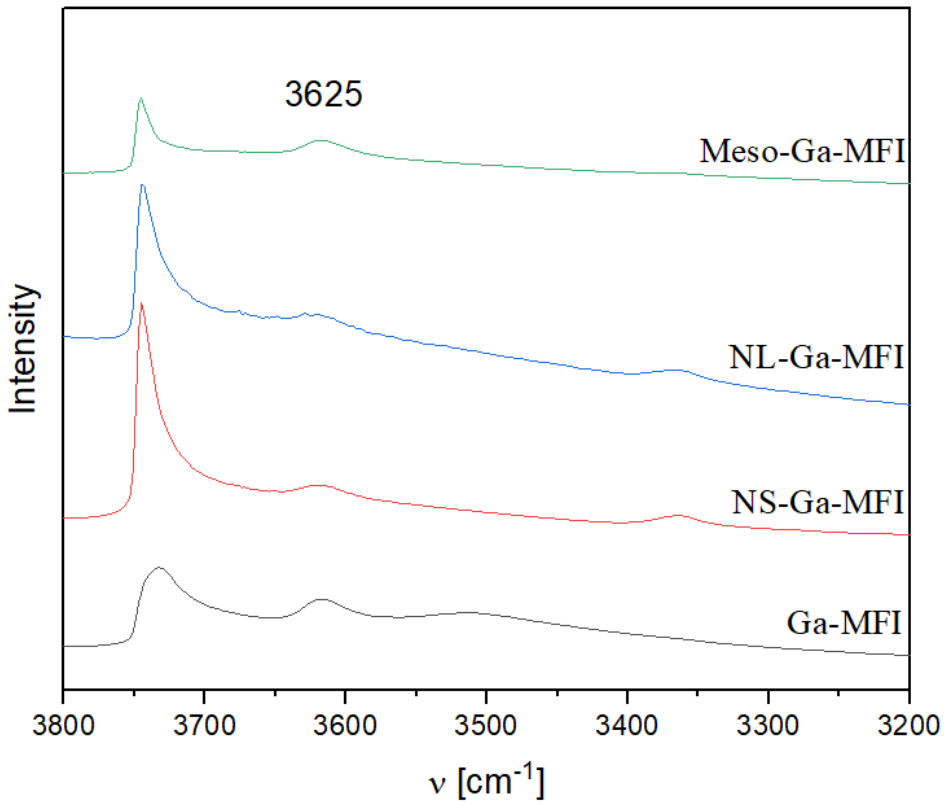

Figure 29b: FTIR spectra of Ga-containing zeolites in the OH region after adsorption of 2,6-di-tert-butylpyridine at 150 °C. The BAS band at 3625 cm^{-1} is still present.

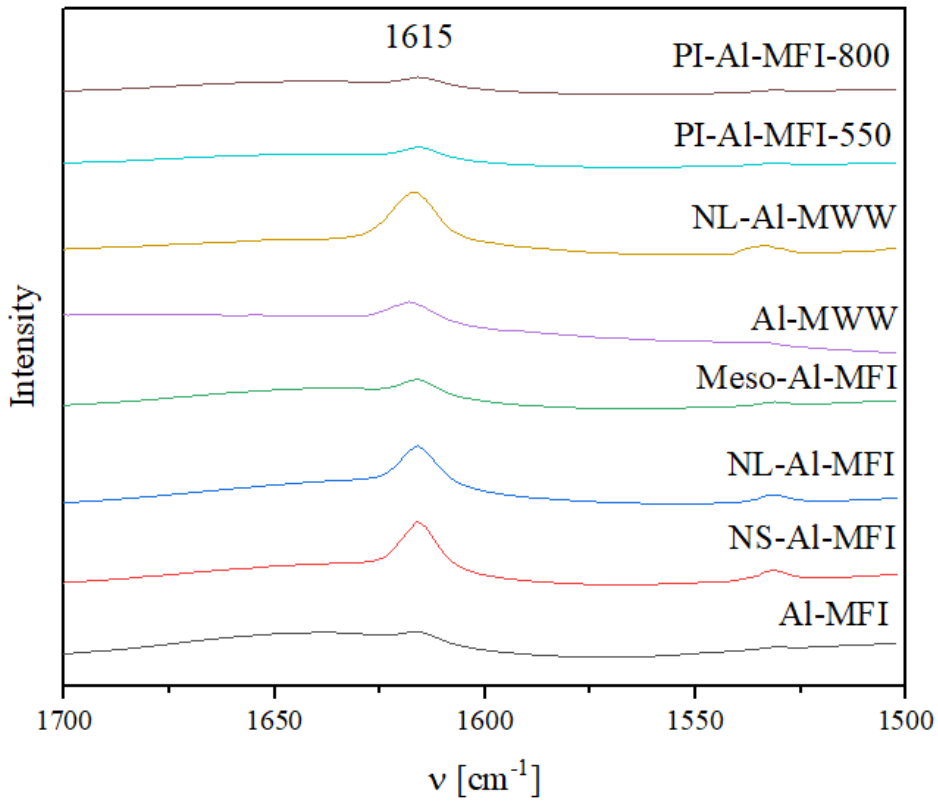

Figure 29c: FTIR spectra of Al-containing zeolites in the vibration region of the DTBP ring after adsorption of 2,6-di-tert-butylpyridine at 150 °C.

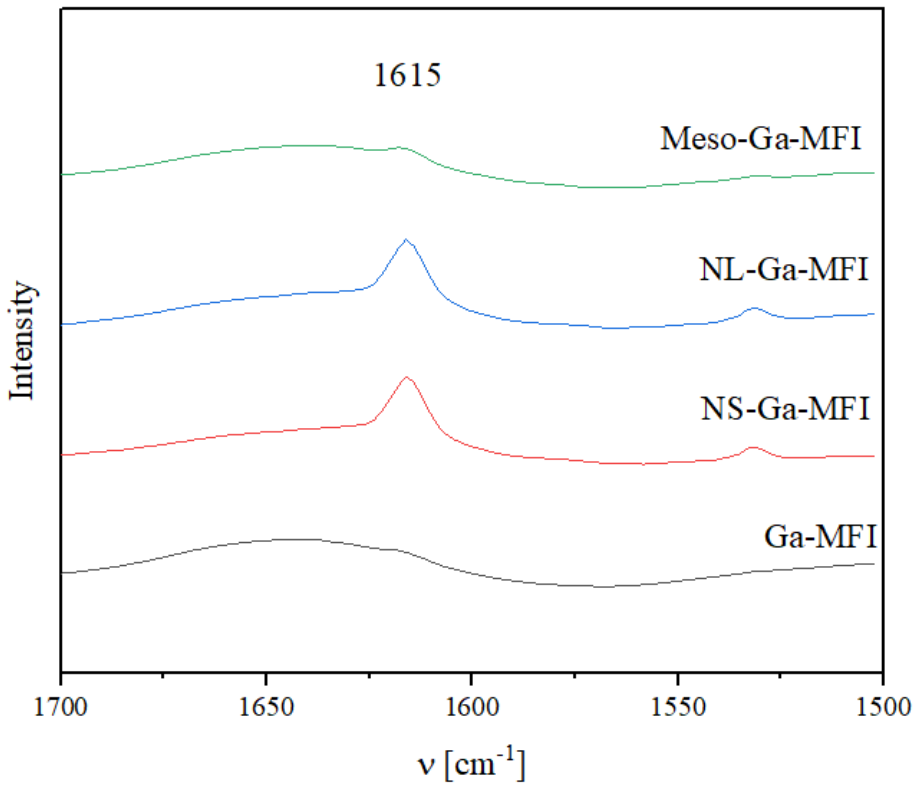

Figure 29d: FTIR spectra of Ga-containing zeolites in the vibration region of the DTBP ring after adsorption of 2,6-di-tert-butylpyridine at 150 °C.

The fraction of BAS accessible for the interaction with DTBP increased in the following sequence of **MFI** catalysts: MFI (0 – 10%) < Meso-MFI (14 – 15%) << NL-MFI (62 – 73%); NS-MFI (62 – 71%) for both Al- and Ga-containing series (Figure 30). 25% of the BAS were accessible for DTBP in conventional Al-MWW, while the hierarchical NL-Al-MWW showed 47% of the BAS interacting with DTBP. Noticeably, NL- and NS-MFI zeolites feature the highest BAS fraction accessible for DTBP, which agrees with the advanced external surface of these materials (Table 3). The experiments show that Al-MFI possesses small amount of accessible acid sites, which might be due to some structural defects.

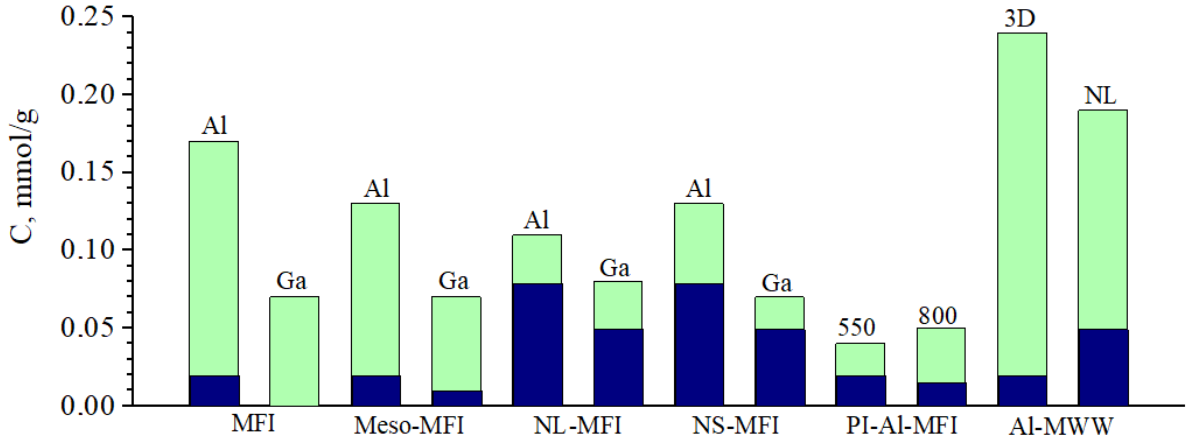

Figure 30: Concentration of BAS as determined by FTIR-monitored adsorption of pyridine (a sum of light green and blue parts of the bars) and 2,6-di-tert-butylpyridine (blue part of the bars).

4.2. Properties-function relationships of zeolite catalysts in the PFC reaction

The catalytic performance of **MFI** and **MWW** zeolites with variable textural and acidic properties and chemical composition (Al, Ga) was evaluated in a one-pot three-component cascade PFC reaction between butyraldehyde, 3-buten-1-ol and anisole. In addition to the targeted products of this reaction, isomeric 4-(2-methoxyphenyl)-2-propyl tetrahydropyran **1** and 4-(4-methoxyphenyl)-2-propyl tetrahydropyran **2** (Figures 19 and 31), the observed by-products included butyraldehyde di-3-butenyl acetal (product **3**), 4-(3-buten-1-oxy)-2-propyl tetrahydropyran (product **4**), 2-propyloxan-4-ol (product **5)** and 2-ethyl-2-hexenal (product **6**).

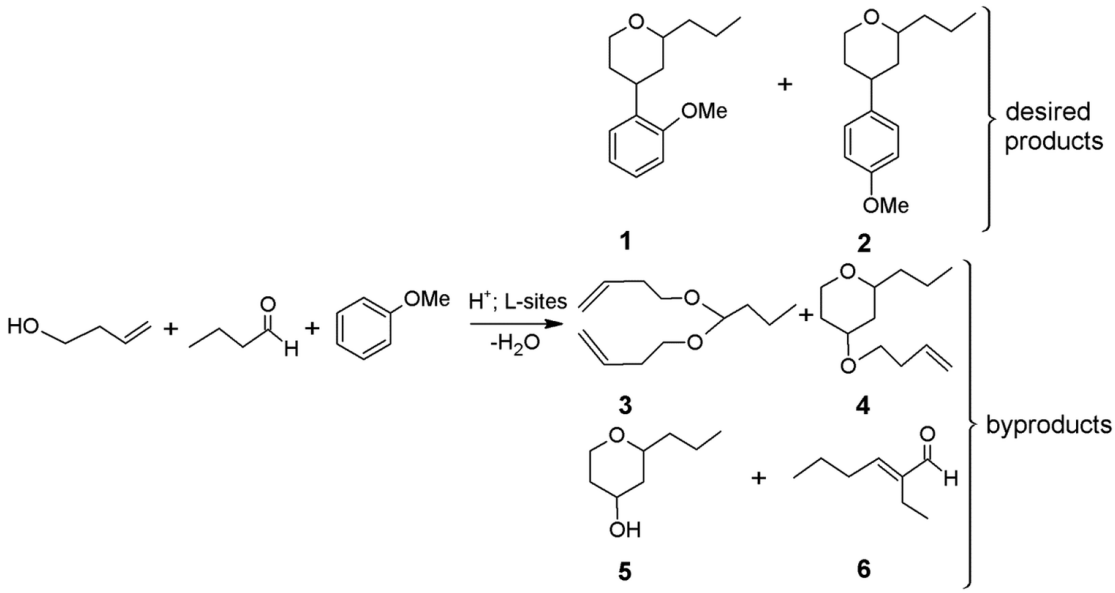

Figure 31: Products of the PFC reaction over zeolite catalysts. **1)** 4-(2-methoxyphenyl)-2-propyl tetrahydropyran, **2)** 4-(4-methoxyphenyl)-2-propyl tetrahydropyran, **3)** butyraldehyde di-3-butenyl acetal, **4)** 4-(3-buten-1-oxy)-2-propyl tetrahydropyran, **5)** 2-propyloxan-4-ol, **6)** 2-ethyl-2-hexenal.[70]

The formation of bulky side products **3-5** was only detected for NS-, NL-MFI, Al-MWW and NL-Al-MWW zeolites with developed mesoporosity, although the selectivity to **3-5** was lower (<15%) than the selectivity towards the targeted products **1+2** (50 – 75% at butyraldehyde conversion of 75%) reached with these zeolites. In turn, products **3-5** were not detected for reactions catalysed by microcrystalline and Meso-MFI zeolites. Noticeably, most of the studied zeolites showed a high selectivity toward 2-ethyl-2-hexanal (**6** on Figure 31), which is a product of aldol condensation of butyraldehyde molecules. Selectivity towards product **6** decreased with increasing butyraldehyde conversion for all catalysts studied (Figure 32a-b). This result is in line with the reversibility of the aldol condensation reaction and the partial consumption of **6** over time. In particular, the NS- and NL-Al-MFI zeolites showed 30% selectivity toward **6**, while MWW zeolites exhibit negligible selectivity towards this side product (2% for Al-MWW, 10% for NL-Al-MWW) after 24 h of reaction. On the contrary, for conventional and Meso-MFI zeolites, **6** remained the main product of the reaction, even after 24 hours of reaction time. All Ga-containing zeolites irrespectively of the structure show a high selectivity towards **6** (72% for NS-Ga-MFI after 24 hours of reaction time). Both PI-Al-MFI zeolites perform comparably to Ga-containing MFI zeolites, reaching around 65% selectivity toward **6**.

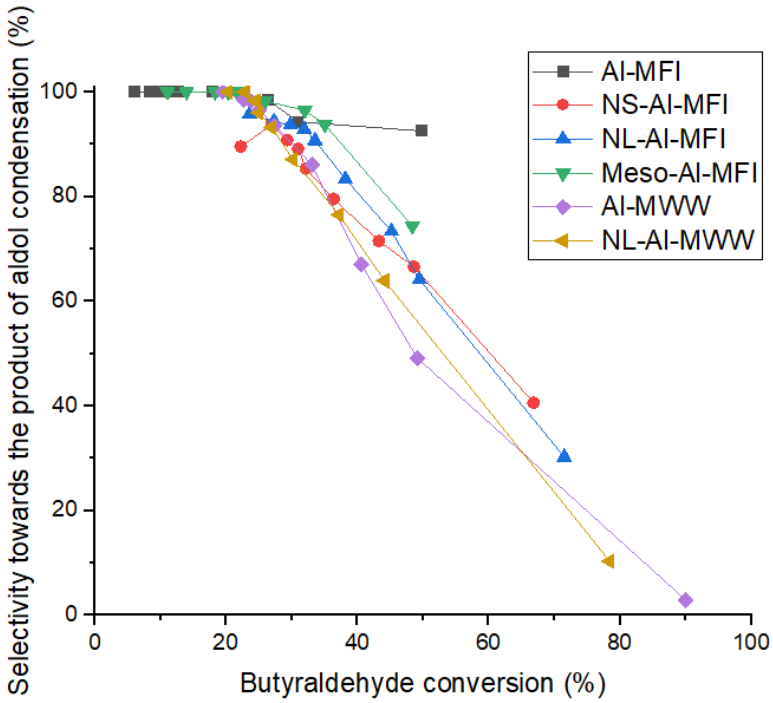

Figure 32a: Dependence of selectivity towards **6** on butyraldehyde conversion.

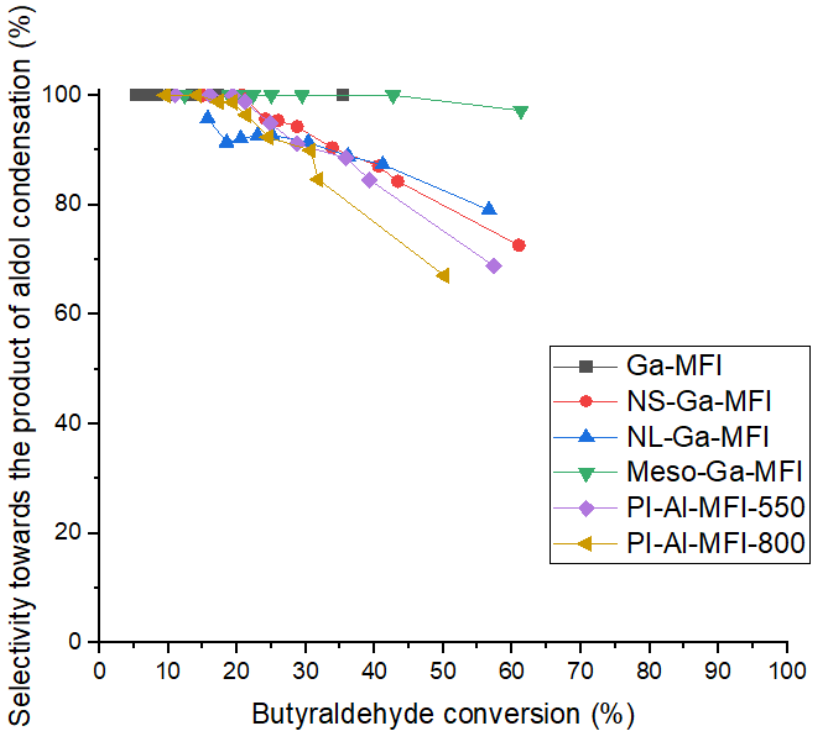

Figure 32b: Dependence of selectivity towards **6** on butyraldehyde conversion.

Table 5 summarizes the butyraldehyde conversions and selectivities towards targeted products **1**+**2** (Figures 19 and 31) reached over studied catalysts, while the effect of specific

properties of the catalysts on their performance is discussed in detail in the following Sections of the thesis.

Table 5: An overview of butyraldehyde conversions and selectivities to products **1**+**2** at a conversion of 50% over the studied zeolites.

Catalyst	Conversion [%]		Selectivity [%]
	6 h	24 h	
Al-MFI	31	50	4
NS-Al-MFI	49	67	15
NL-Al-MFI	49	72	24
Meso-Al-MFI	35	50	22
Al-MWW	49	90	37
NL-Al-MWW	44	78	34
Ga-MFI	17	35	0
NS-Ga-MFI	43	61	8
NL-Ga-MFI	41	57	6
Meso-Ga-MFI	43	61	1
PI-Al-MFI-550	32	50	15
PI-Al-MFI-800	39	57	25

4.2.1. The effect of the nature of acid sites

To study the influence of the nature of the acid sites on the catalyst's performance in the PFC reaction, two pillared Al-containing zeolites with different LAS/BAS ratio were assessed. Calcination at high (800 °C) temperatures causes partial transformation of a BAS into a LAS by dehydroxylation. With this procedure, the LAS/BAS ratio changed from 1 (PI-Al-MFI-550) to 2 (PI-Al-MFI-800). The results of the following catalytic tests (Figure 33) showed that the increase in the LAS/BAS ratio had a negative effect on conversion, but it increased the selectivity towards the targeted substituted tetrahydropyrans **1**+**2** (from 15 to 25% at 50% conversion). These results show that a higher fraction of LAS in zeolite catalyst might be beneficial for the selective production of substituted tetrahydropyrans *via* the PFC reaction.

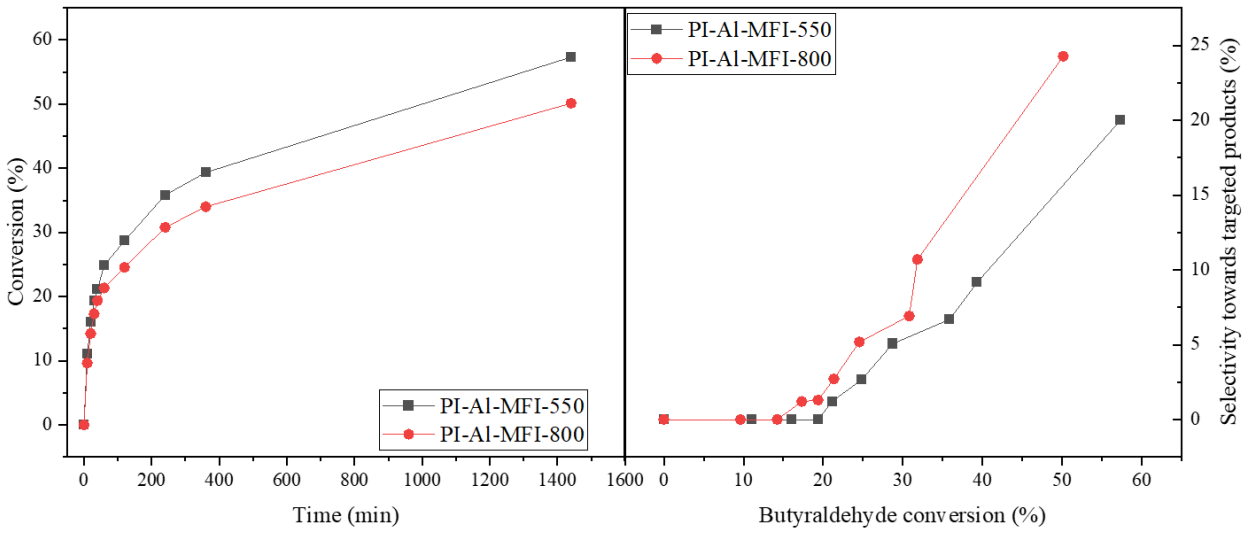

Figure 33: Butyraldehyde conversion *vs.* time (left) and selectivity of products **1**+**2** of the PFC reaction *vs.* butyraldehyde conversion (right) over hierarchical Al-containing **MFI** zeolite catalysts with different BAS/LAS ratios.

4.2.2. The effect of the chemical compositions

To address the effect of the chemical composition on the catalytic performance of a zeolite in the PFC reaction, Al- and Ga-containing **MFI** catalysts were evaluated (Figure 34). As stated in Section 4.1.2., Ga-containing zeolites have a higher fraction of weak acid sites and a higher fraction of LAS when compared to Al-containing ones. A comparison of the catalytic performance of NS-Ga-MFI and NS-Al-MFI zeolites with similar (i) textural characteristics (Table 3); (ii) total concentration of acid sites (0.19 mmol/g, Table 4) and (iii) number of highly accessible BAS (Figure 30) reveals a slight effect of the chemical composition on butyraldehyde conversion (43% *vs.* 49% after 6h for Ga- and Al, respectively, Table 5). The lower conversion of butyraldehyde over NS-Ga-MFI can be related to its higher LAS/BAS ratio compared with NS-Al-MFI, although the role of weaker strength of acid sites cannot be completely ruled out. The main difference in the catalytic behaviour between the Ga- and Al- containing zeolites is the lower selectivity of the targeted products **1**+**2** observed for the former catalysts. As the results presented in Section 4.2.1 evidence a positive effect of increase in LAS/BAS ratio on catalyst selectivity, the decrease in acid site strength is considered the main factor deteriorating the selectivity of Ga-containing zeolite catalysts in comparison to Al-substituted ones.

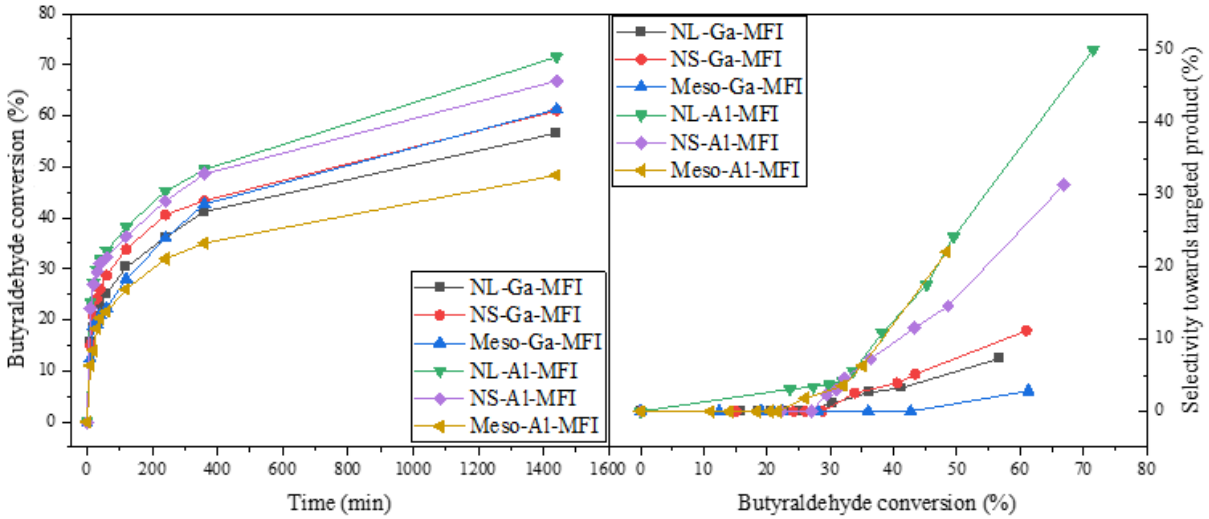

Figure 34: Butyraldehyde conversion *vs.* time (left) and selectivity of products **1**+**2** of the PFC reaction *vs.* butyraldehyde conversion (right) over Al- and Ga-containing hierarchical **MFI** zeolite catalysts.

4.2.3. The effect of textural properties

Comparative analysis of the catalytic performance of conventional and hierarchical (NS-, NL-, Meso-) Al-containing **MFI** zeolites in the PFC reaction revealed that the textural properties of zeolites have a clear effect on both the conversion of butyraldehyde and the selectivity towards the targeted products (Figure 35). NS- and NL-type zeolites reach conversions much higher (67% and 72% after 24 h for NS- and NL-Al-MFI, respectively) than conventional Al-MFI (50%) and Meso-Al-MFI (48%). Since the total concentration of acid sites for the studied zeolites is comparable and the most active NS- and NL-Al-MFI samples show lower acid site strength and higher LAS/BAS ratio (Table 4), the textural properties and hence the accessibility of these sites are crucial. The reaction in the case of microcrystalline Al-MFI zeolite is probably limited by diffusion of the reactants and the products because of the small size of the micropores. Therefore, despite having the lowest fraction of LAS and the highest strength of acid centres, Al-MFI was characterized by the lowest conversion value. The low butyraldehyde conversion over Meso-MFI compared to NL-MFI with a similar fraction of strong acid centres may be associated with the significantly lower concentration of external acid sites in Meso-MFI catalyst (Table 4, Figure 30). Such external acid sites are required for facilitation of aromatic electrophilic substitution of bulky reagents.

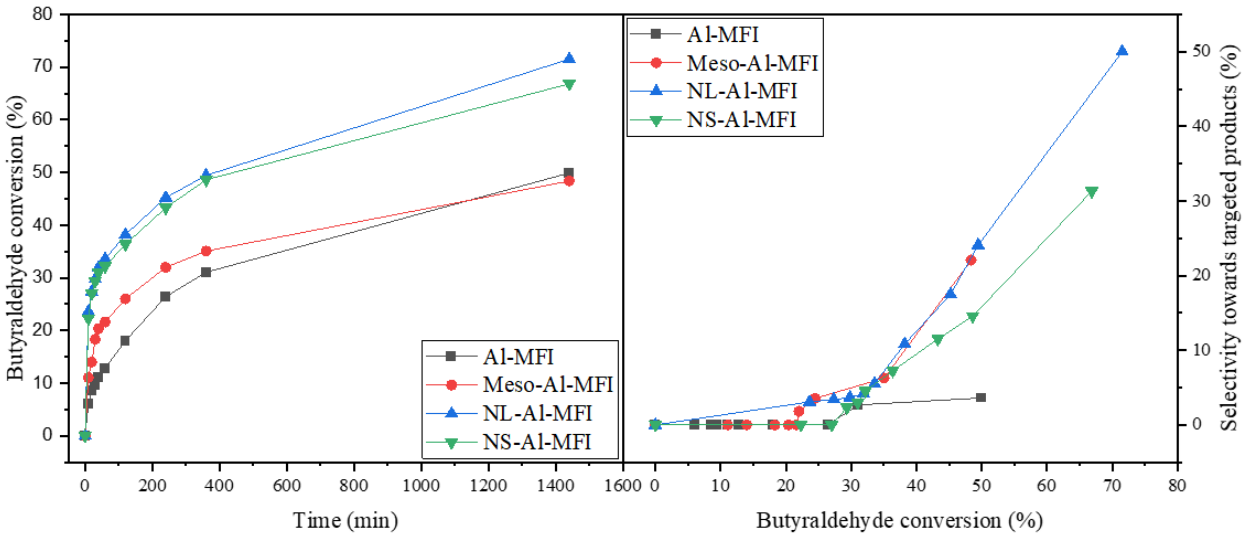

Figure 35: Butyraldehyde conversion *vs.* time (left) and selectivity of products **1**+**2** of the PFC reaction *vs.* butyraldehyde conversion (right) over Al-containing **MFI** zeolite catalysts.

The selectivity towards the targeted products **1+2** does not exceed 5% for microcrystalline Al-MFI zeolite, which may be explained by the negligible amount of accessible acid sites in this purely microporous catalyst. Higher selectivity of **1+2** for Meso- (22%), NS- (15%) and NL-zeolites (24%) is likely related to the presence of active sites on the well-developed external surface providing sufficient reaction space for the formation of bulky targeted products. However, the selectivity of **1+2** cannot be univocally correlated with the number of highly accessible BAS, considering that 1) the concentration of highly accessible BAS in Meso-zeolite is significantly lower than that of NS- and NL-zeolites (Table 4), and 2) Meso- zeolite still shows similar or even higher selectivity towards **1**+**2** compared to NS- and NL-zeolites. Therefore, highly accessible LAS, whose concentration cannot be measured by FTIR of adsorbed 2,6-di-tert-butylpyridine, seem also play a role in the PFC reaction by affecting the selectivity of zeolite catalysts.

4.2.4. The effect of the zeolite framework structure

Al-substituted **MFI** and **MWW** zeolites were assessed in the PFC reaction to investigate the effect of zeolite structure in the PFC reaction (Figure 36). Both conventional and nanolayered **MWW** zeolites showed higher conversion values (78 and 90% after 24 h for NL-Al-MWW and Al-MWW, respectively) and selectivity (34 – 37% at 50% conversion) compared with the most active hierarchical NL- (72% conversion, 24% selectivity) and NS-MFI (67% conversion, 15% selectivity) zeolites.

The higher conversion of the studied **MWW** zeolites may be related to the much higher total concentration of acid sites (0.37 – 0.41 mmol/g) compared to that of hierarchical

Al-MFI catalysts (0.20 mmol/g). In turn, advanced selectivity of **MWW** zeolites can hardly be explained by their specific acidic characteristics, as both Al-MWW and the studied hierarchical Al-MFI zeolites showed similar strength of acid sites (60 – 70%, Table 4) and comparable LAS/BAS ratio (0.8 and 0.9 for NL-Al-MFI and NL-Al-MWW, respectively, Table 4), while the concentration of accessible Brønsted acid sites in the **MWW** zeolites was even lower than that of NL- or NS-Al-MFI zeolites (Figure 30). As mentioned in a previous Section 4.2.3, the accessibility of BAS does not seem to be the core factor behind the high selectivity in PFC. Assumedly, high selectivity of Al-MWW catalysts could originate from (i) accessible LAS, which could not be measured with the methods used in this work or (ii) the presence of the external semi-cups on the external surface of **MWW** zeolites, providing the confined space for the formation of products **1**+**2**.

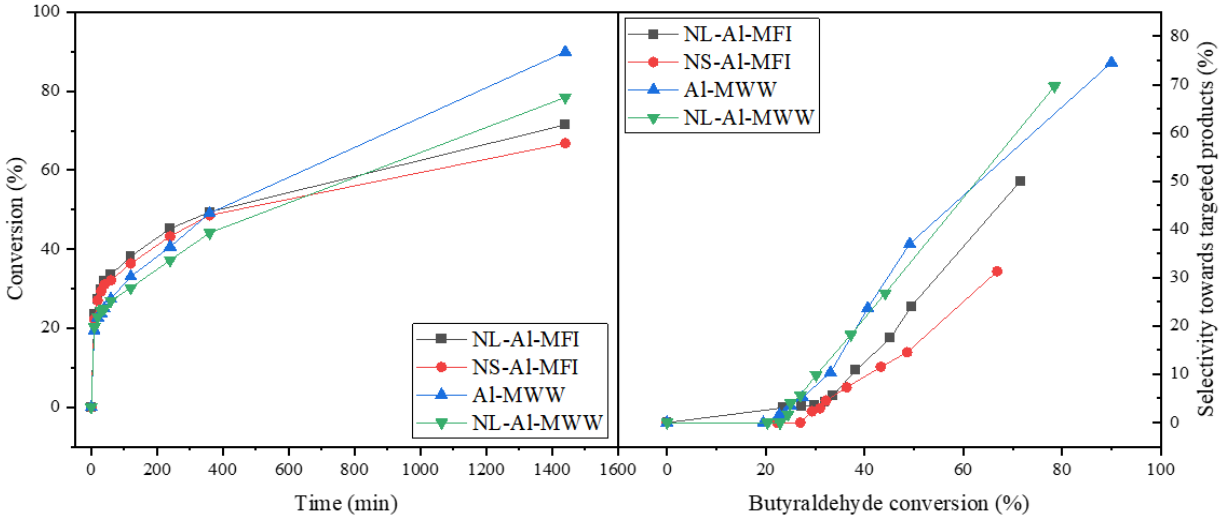

Figure 36: Butyraldehyde conversion *vs.* time (left) and selectivity of products **1**+**2** of the PFC reaction *vs.* butyraldehyde conversion (right) over Al-containing **MFI** and **MWW** zeolite catalysts.

4.2.5. Catalytic activity of zeolite catalysts in the PFC reaction

The activity of the studied zeolites was compared in terms of the initial reaction rate normalized per total concentration of BAS and LAS (Figure 37). The rate of the PFC reactions catalysed by Ga-containing zeolites did not exceed 60 h^{-1}, while Al-substituted catalysts showed values ranging from 11 to 485 h^{-1} depending on textural properties and structure of the zeolite framework. Thus, the initial reaction rate increased in the following sequence of Al-containing zeolite catalysts: Al-MFI (11 h^{-1}) < Meso-Al-MFI (41 h^{-1}) < NL-Al-MWW (78 h^{-1}) < Al-MWW (126 h^{-1}) << NS-Al-MFI (242 h^{-1}) << NL-Al-MFI (485 h^{-1}). Notably, NL- and NS-Al-MFI zeolites show higher reaction rate than Meso-MFI zeolite, which means that hierarchical zeolites with advanced external surface may be more favourable for catalysing the PFC cascade reaction than micro-mesoporous catalysts with

intracrystalline mesoporosity. While showing higher conversion and selectivity values (Table 5), both Al-MWW and NL-Al-MWW catalysts demonstrated 3-5 times lower values of the normalized reaction rate compared to NL- and NS-Al-MFI catalysts. The obtained result reflects the increase in turnover frequency of a zeolite catalyst in the PFC reaction with increasing accessibility of active sites in a catalyst.

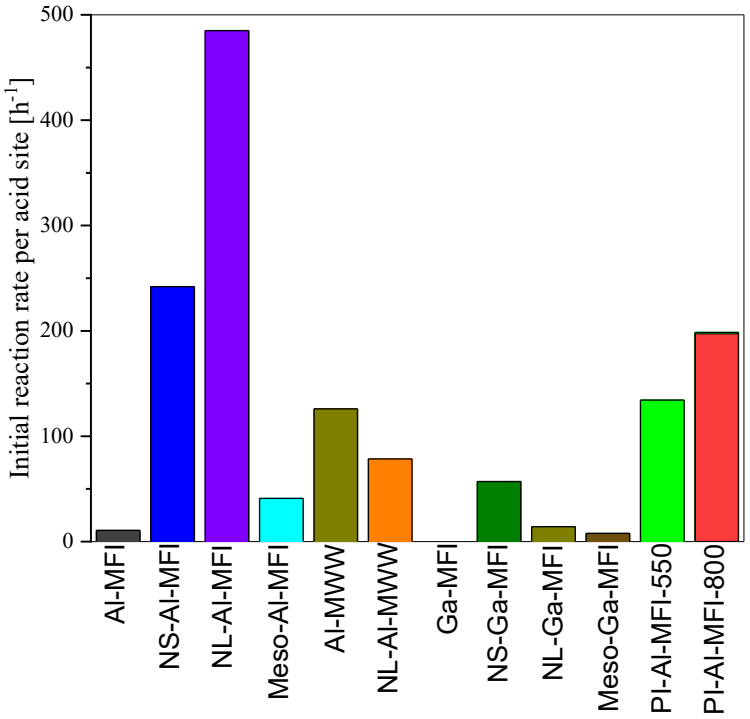

Figure 37: Initial reaction rate of the PFC reaction catalysed by different zeolites.

5. Conclusions

Recent research in zeolite science is focused on designing strategies for preparation of hierarchical micro-mesoporous or micro-macroporous zeolites, with the purpose of replacing toxic and environmentally unfriendly homogeneous catalysts used for different reactions, involving bulky reagents and/or products. A one-pot three-component Prins-Friedel-Crafts reaction of an aldehyde, homoallylic alcohol, and aromatic compound is one of the processes demanding such intensification for efficient production of valuable heterocyclic compounds containing the 4-aryltetrahydropyran moiety. This work provides a detailed catalytic evaluation of specially synthesized Al- and Ga- substituted zeolites with the same topology but variable crystal morphology to address the acidic and textural characteristics of a heterogeneous acid catalyst, which are crucial for attaining high activity and selectivity in the PFC reaction of butyraldehyde, 3-buten-1-ol and anisole.

Microcrystalline, nanolayered, nanosponge and mesoporous Al- and Ga-containing **MFI** zeolites, as well as microcrystalline and nanolayered Al-containing **MWW** zeolites, were prepared and characterized using a combination of characterization techniques. The structural and textural properties of zeolites were investigated by X-ray diffraction and nitrogen physisorption, respectively. Electron microscopy was used to provide information about their morphology, while ICP-OES was used to determine their Si/T ratio. FTIR spectroscopy of adsorbed probe molecules was used to assess the nature, strength, and accessibility of acid sites as potential catalytic centres in these zeolites. The catalytic activity of the designed materials was investigated in the PFC reaction of butyraldehyde, 3-buten-1-ol, and anisole under mild conditions (60 °C).

The results convincingly showed the crucial role of the nature, strength, and distribution of acid sites between the internal and external surfaces of the crystals, as well as the important impact of zeolite structure on the butyraldehyde conversion and selectivity toward targeted products of the PFC reaction. Butyraldehyde conversion in zeolite-catalysed PFC reaction was found to increase with

(i) *the strength of acid sites* (as shown for Al- *vs.* Ga-containing nanosponge **MFI** zeolites with similar total concentration of acid centres, their strength, and accessibility);

(ii) *number of highly accessible acid centres* located on the external surface of the crystals (as shown for hierarchical nanolayered *vs.* mesoporous Al-containing **MFI** zeolites with similar total concentration of acid centres and their strength);

(iii) *concentration of Brønsted acid sites* (as shown for pillared Al-containing **MFI** zeolites with a similar total concentration of acid sites and their accessibility, but different LAS/BAS ratios).

In turn, zeolites with (i) *a higher Lewis-to-Brønsted acid site ratio* and/or (ii) *higher strength of acid sites* provided better selectivity toward targeted tetrahydropyran-containing compounds.

Among the catalysts investigated, Al-containing **MWW** zeolites with plate-like crystal morphology, developed mesoporosity, high total concentration of acid sites, and remarkable fraction of external acid sites that can be located in the semi-cups on the outer surface of the crystals showed the highest values of butyraldehyde conversion (90% after 24 h) and selectivity toward the products of PFC reaction (37% at 50% conversion).

In terms of further perspectives, despite being challenging, the synthesis and following catalytic test on different three-valent element-substituted **MWW** zeolites, such as B-, Ga-, and Fe-containing materials, can help to generalize the conclusions made in this work.

6. References

1. Cronstedt, A. F., Observation and description of anunknown mineral species, called zeolite. *Journal of the Swedish Royal Academy of Sciences* **1756,** *17*.
2. Roque-Malherbe, R., Applications of Natural Zeolites in Pollution Abatement and Industry. In *Handbook of Surfaces and Interfaces of Materials*, Nalwa, H. S., Ed. Academic Press: 2001; Vol. 5, pp 495-522.
3. Přech, J.; Pizarro, P.; Serrano, D. P.; Čejka, J., From 3D to 2D zeolite catalytic materials. *Chem. Soc. Rev.* **2018,** *47* (22), 8263-8306.
4. Baerlocher, C.; McCusker, L. B.; Meier, W. M.; Olson, D. H. IZA Commission on Natural Zeolites. http://www.iza-online.org/natural/default.htm.
5. Baerlocher, C.; McCusker, L. B.; Meier, W. M.; Olson, D. H. Database of Zeolite Structures. https://europe.iza-structure.org/IZA-SC/ftc_table.php.
6. Rabo, J. A.; Schoonover, M. W., Early Discoveries in Zeolite Chemistry and Catalysis at Union Carbide, and Follow-Up in Industrial Catalysis. *Appl. Catal. A, Gen.* **2001,** *222*, 261-275.
7. Čejka, J.; Žilková, N., Synthesis and structure of zeolites. *Chem. Listy* **2000,** *94* (5), 278-287.
8. Weitkamp, J., Zeolites and catalysis. *Solid State Ion.* **2000,** *131* (1), 175-188.
9. Přech, J., Catalytic performance of advanced titanosilicate selective oxidation catalysts – a review. *Catal. Rev.* **2018,** *60* (1), 71-131.
10. Cristina, M.; Avelino, C., Inorganic molecular sieves: Preparation, modification and industrial application in catalytic processes. *Coord. Chem. Rev.* **2011,** *255* (13), 1558-1580.
11. Csicsery, S. M., Shape-selective catalysis in zeolites. *Zeolites* **1984,** *4* (3), 202-213.
12. Shamzhy, M.; Opanasenko, M.; Concepción, P.; Martínez, A., New trends in tailoring active sites in zeolite-based catalysts. *Chem. Soc. Rev.* **2019,** *48* (4), 1095-1149.
13. McCusker, L. B.; Baerlocher, C., Chapter 2 - Zeolite Structures. In *Stud. Surf. Sci. Catal.*, Čejka, J.; van Bekkum, H.; Corma, A.; Schüth, F., Eds. Elsevier: 2007; Vol. 168, pp 13-37.
14. Flanigen, E. M., Chapter 2 - Zeolites and molecular sieves: An historical perspective. In *Stud. Surf. Sci. Catal.*, van Bekkum, H.; Flanigen, E. M.; Jacobs, P. A.; Jansen, J. C., Eds. Elsevier: 2001; Vol. 137, pp 11-35.
15. Meeprasert, J.; Jungsuttiwong, S.; Namuangruk, S., Location and acidity of Brønsted acid sites in isomorphously substituted LTL zeolite: A periodic density functional study. *Microporous Mesoporous Mater.* **2013,** *175*, 99-106.
16. De, S.; Dutta, S.; Saha, B., Critical design of heterogeneous catalysts for biomass valorization: current thrust and emerging prospects. *Catal. Sci. Tech.* **2016,** *6* (20), 7364-7385.
17. Burton, A. W.; Zones, S. I., Chapter 5 - Organic Molecules in Zeolite Synthesis: Their Preparation and Structure-Directing Effects. In *Stud. Surf. Sci. Catal.*, Čejka, J.; van Bekkum, H.; Corma, A.; Schüth, F., Eds. Elsevier: 2007; Vol. 168, pp 137-179.
18. Bellussi, G.; Carati, A.; Millini, R., Industrial Potential of Zeolites. In *Zeolites and Catalysis*, Čejka, J.; Corma, A.; Zones, S., Eds. 2010; pp 449-491.
19. Pérez-Ramírez, J.; Christensen, C.; Egeblad, K.; Christensen, C.; Groen, J., ChemInform Abstract: Hierarchical Zeolites: Enhanced Utilization of Microporous Crystals in Catalysis by Advances in Materials Design. *Cheminform* **2009,** *40*.
20. Roth, W. J.; Nachtigall, P.; Morris, R. E.; Čejka, J., Two-Dimensional Zeolites: Current Status and Perspectives. *Chem. Rev. (Washington, DC, U. S.)* **2014,** *114* (9), 4807-4837.
21. Chlubná, P.; Roth, W. J.; Greer, H. F.; Zhou, W.; Shvets, O.; Zukal, A.; Čejka, J.; Morris, R. E., 3D to 2D Routes to Ultrathin and Expanded Zeolitic Materials. *Chem. Mater.* **2013,** *25* (4), 542-547.

22. Nakai, K.; Sonoda, J.; Yoshida, M.; Hakuman, M.; Naono, H., High resolution adsorption isotherms of N_2 and Ar for nonporous silicas and MFI zeolites. *Adsorption* **2007,** *13*, 351-356.
23. Chu, C. T. W.; Chang, C. D., Isomorphous substitution in zeolite frameworks. 1. Acidity of surface hydroxyls in [B]-, [Fe]-, [Ga]-, and [Al]-ZSM-5. *J. Phys. Chem.* **1985,** *89* (9), 1569-1571.
24. Janda, A.; Bell, A. T., Effects of Si/Al Ratio on the Distribution of Framework Al and on the Rates of Alkane Monomolecular Cracking and Dehydrogenation in H-MFI. *J. Am. Chem. Soc.* **2013,** *135* (51), 19193-19207.
25. Yabushita, M.; Yoshida, M.; Muto, F.; Horie, M.; Kunitake, Y.; Nishitoba, T.; Maki, S.; Kanie, K.; Yokoi, T.; Muramatsu, A., Hydrothermal synthesis of Ga-substituted MFI zeolites via a mechanochemical process and their catalytic activity for methane transformation. *Mol. Catal.* **2019,** *478*, 110579.
26. Satyarthi, J.; Saikia, L.; Darbha, S.; Ratnasamy, P., Regio-and stereoselective synthesis of β-amino alcohols over titanosilicate molecular sieves. *Appl. Catal. A, Gen.* **2007,** *330*, 145-151.
27. Choi, M.; Na, K.; Kim, J.; Sakamoto, Y.; Terasaki, O.; Ryoo, R., Stable single-unit-cell nanosheets of zeolite MFI as active and long-lived catalysts. *Nature* **2009,** *461* (7261), 246-249.
28. Na, K.; Choi, M.; Park, W.; Sakamoto, Y.; Terasaki, O.; Ryoo, R., Pillared MFI Zeolite Nanosheets of a Single-Unit-Cell Thickness. *J. Am. Chem. Soc.* **2010,** *132* (12), 4169-4177.
29. Na, K.; Jo, C.; Kim, J.; Cho, K.; Jung, J.; Seo, Y.; Messinger, R. J.; Chmelka, B. F.; Ryoo, R., Directing zeolite structures into hierarchically nanoporous architectures. *Science* **2011,** *333* (6040), 328-32.
30. Meng, L.; Mezari, B.; Goesten, M. G.; Wannapakdee, W.; Pestman, R.; Gao, L.; Wiesfeld, J.; Hensen, E. J. M., Direct synthesis of hierarchical ZSM-5 zeolite using cetyltrimethylammonium as structure directing agent for methanol-to-hydrocarbons conversion. *Catal. Sci. Tech.* **2017,** *7* (19), 4520-4533.
31. Xing, E.; Shi, Y.; Xie, W.; Zhang, F.; Mu, X.; Shu, X., Perspectives on the multi-functions of aniline: Cases from the temperature-controlled phase transfer hydrothermal synthesis of MWW zeolites. *Microporous Mesoporous Mater.* **2017,** *254*, 201-210.
32. Shamzhy, M.; Gil, B.; Opanasenko, M.; Roth, W. J.; Čejka, J., MWW and MFI Frameworks as Model Layered Zeolites: Structures, Transformations, Properties, and Activity. *ACS Catal.* **2021,** *11* (4), 2366-2396.
33. Korzeniowska, A.; Grzybek, J.; Kałahurska, K.; Kubů, M.; Roth, W.; Gil, B., The structure-catalytic activity relationship for the transient layered zeolite MCM-56 with MWW topology. *Catal. Today* **2019,** *345*, 116-124.
34. Wang, Y.; Liu, Y.; Wang, L.; Wu, H.; Li, X.; He, M.; Wu, P., Postsynthesis, Characterization, and Catalytic Properties of Aluminosilicates Analogous to MCM-56. *J. Phys. Chem. C* **2009,** *113* (43), 18753-18760.
35. Kałahurska, K.; Ziemiański, P. P.; Roth, W. J.; Gil, B., From Colloidal Dispersions of Zeolite Monolayers to Effective Solid Catalysts in Transformations of Bulky Organic Molecules: Role of Freeze-Drying and Dialysis. *Molecules* **2021,** *26* (7), 2076.
36. Xu, L.; Sun, J., Recent Advances in the Synthesis and Application of Two-Dimensional Zeolites. *Adv. Energy Mater.* **2016,** *6* (17), 1600441.
37. Stanjek, H.; Häusler, W., Basics of X-ray Diffraction. *Hyperfine Interact.* **2004,** *154* (1), 107-119.
38. Smyth, M. S.; Martin, J. H. J., X-Ray crystallography. *Mol. Pathol.* **2000,** *53* (1), 8-14.

39. Chatterjee, A. K., Chapter 8 - X-Ray Diffraction. In *Handbook of Analytical Techniques in Concrete Science and Technology*, Ramachandran, V. S.; Beaudoin, J. J., Eds. William Andrew Publishing: Norwich, NY, 2001; pp 275-332.
40. Seibt, S.; Timothy, R., Microfluidics for Time-Resolved Small-Angle X-Ray Scattering. In *Advances in Microfluidics and Nanofluids*, Murshed, S. M. S., Ed. IntechOpen: Rijeka, 2021.
41. Morris, R. E.; Allan, P. K., Zeolites in catalysis: properties and applications. Čejka, J.; Morris, R. E.; Nachtigall, P., Eds. Royal Society of Chemistry: 2017.
42. Harris, K. D. M., Powder diffraction crystallography of molecular solids. In *Top. Curr. Chem.*, Rissanen, K., Ed. 2012; Vol. 315, pp 133-77.
43. James, B. C., Chapter 1 - An overview and some uninteresting history of physisorption. In *Surface Area and Porosity Determinations by Physisorption (Second Edition)*, Second Edition ed.; James, B. C., Ed. Elsevier: 2020; pp 1-57.
44. Thommes, M., Chapter 15 - Textural Characterization of Zeolites and Ordered Mesoporous Materials by Physical Adsorption. In *Stud. Surf. Sci. Catal.*, Čejka, J.; Bekkum, v. H.; Corma, A.; Schüth, F., Eds. Elsevier: 2007; Vol. 168, pp 495-523.
45. Thommes, M.; Kaneko, K.; Neimark, A. V.; Olivier, J. P.; Rodriguez-Reinoso, F.; Rouquerol, J.; Sing, S. W. K., Physisorption of gases, with special reference to the evaluation of surface area and pore size distribution (IUPAC Technical Report). *Pure Appl. Chem.* **2015,** *87* (9-10), 1051-1069.
46. Kumar, K. V.; Gadipelli, S.; Wood, B.; Ramisetty, K. A.; Stewart, A. A.; Howard, C. A.; Brett, D. J. L.; Rodriguez-Reinoso, F., Characterization of the adsorption site energies and heterogeneous surfaces of porous materials. *J. Mater. Chem. A* **2019,** *7* (17), 10104-10137.
47. Kogure, T., Chapter 2.9 - Electron Microscopy. In *Handbook of Clay Science*, Bergaya, F.; Lagaly, G., Eds. Elsevier: 2013; Vol. 5, pp 275-317.
48. Thomas, J. M.; Terasaki, O.; Gai, P. L.; Zhou, W.; Gonzalez-Calbet, J., Structural elucidation of microporous and mesoporous catalysts and molecular sieves by high-resolution electron microscopy. *Acc. Chem. Res.* **2001,** *34* (7), 583-94.
49. Inkson, B. J., 2 - Scanning electron microscopy (SEM) and transmission electron microscopy (TEM) for materials characterization. In *Materials Characterization Using Nondestructive Evaluation (NDE) Methods*, Hübschen, G.; Altpeter, I.; Tschuncky, R.; Herrmann, H.-G., Eds. Woodhead Publishing: 2016; pp 17-43.
50. Olesik, J. W., 10.9 - ICP-OES: Inductively Coupled Plasma-Optical Emission Spectroscopy. In *Encyclopedia of Materials Characterization*, Brundle, C. R.; Evans, C. A.; Wilson, S., Eds. Butterworth-Heinemann: Boston, 1992; pp 633-644.
51. Zamechek, W.; Pankhurst, R. G. In *ICP proceeding*, International ICP Winter Conference, San Juan, Puerto Rico, San Juan, Puerto Rico, 1980; p 121.
52. Cherevko, S.; Mayrhofer, K. J. J., On-Line Inductively Coupled Plasma Spectrometry in Electrochemistry: Basic Principles and Applications. In *Encyclopedia of Interfacial Chemistry*, Wandelt, K., Ed. Elsevier: Oxford, 2018; pp 326-335.
53. Lorenzo Mino and Luisa Mandrile and Luca Iannarelli and Chiara Portesi and Gianmario Martra and Andrea Mario, R., Chapter 4.6 - Vibrational spectroscopy. In *Characterization of Nanoparticles*, Vasile-Dan Hodoroaba and Wolfgang, E. S. U. a. A. G. S., Ed. Elsevier: 2020; pp 457-480.
54. Stuart, B. H., *Infrared Spectroscopy: Fundamentals and Applications*. 2004; p 248.
55. Smith, B. C., *Fundamentals of Fourier transform infrared spectroscopy*. CRC press: 2011.
56. Lercher, J. A.; Jentys, A., Chapter 13 - Infrared and Raman Spectroscopy for Characterizing Zeolites. In *Stud. Surf. Sci. Catal.*, Čejka, J.; van Bekkum, H.; Corma, A.; Schüth, F., Eds. Elsevier: 2007; Vol. 168, pp 435-476.

57. Loughridge, R.; Abramovitch, D., A tutorial on laser interferometry for precision measurements. In *Proceedings of the American Control Conference*, 2013; pp 3686-3703.
58. Ahmed, S.; El-Faer, M. Z.; Abdillahi, M. M.; Shirokoff, J.; Siddiqui, M. A. B.; Barri, S. A. I., Production of methyl tert-butyl ether (MTBE) over MFI-type zeolites synthesized by the rapid crystallization method and modified by varying Si/Ai ratio and steaming. *Appl. Catal. A, Gen.* **1997,** *161* (1), 47-58.
59. Patis, A.; Dracopoulos, V.; Nikolakis, V., Investigation of Silicalite-1 Crystallization Using Attenuated Total Reflection/Fourier Transform Infrared Spectroscopy. *J. Phys. Chem. C* **2007,** *111* (47), 17478-17484.
60. Byrappa, K.; Kumar, B. S., Characterization of zeolites by infrared spectroscopy. *Asian J. Chem.* **2007,** *19* (6), 4933.
61. Bordiga, S.; Lamberti, C.; Bonino, F.; Travert, A.; Thibault-Starzyk, F., Probing zeolites by vibrational spectroscopies. *Chem. Soc. Rev.* **2015,** *44* (20), 7262-7341.
62. Blumberg, L. M., Chapter 2 - Theory of gas chromatography. In *Gas Chromatography (Second Edition)*, Poole, C. F., Ed. Elsevier: Amsterdam, 2021; pp 19-97.
63. Geiger, W. M.; McElmurry, B. A., Chapter 5 - Gas chromatography. In *Sample Introduction Systems in ICPMS and ICPOES*, Beauchemin, D., Ed. Elsevier: Amsterdam, 2020; pp 255-298.
64. Jones, F. W., Estimation of Flame-Ionization Detector Relative Response Factors for Oligomers of Alkyl and Aryl Ether Polyethoxylates using the Effective Carbon Number Concept. *J. Chromatogr. Sci.* **1998,** *36* (5), 223-226.
65. Katsanos, N. A.; Thede, R.; Roubani-Kalantzopoulou, F., Review. *Journal of Chromatography A* **1998,** *795* (2), 133-184.
66. Nicolaou, K. C.; Edmonds, D. J.; Bulger, P. G., Cascade reactions in total synthesis. *Angew Chem Int Ed Engl* **2006,** *45* (43), 7134-86.
67. Nicolaou, K. C.; Chen, J. S., The art of total synthesis through cascade reactions. *Chem. Soc. Rev.* **2009,** *38* (11), 2993-3009.
68. Grondal, C.; Jeanty, M.; Enders, D., Organocatalytic cascade reactions as a new tool in total synthesis. *Nat. Chem.* **2010,** *2* (3), 167-78.
69. Sakata, Y.; Yasui, E.; Takatori, K.; Suzuki, Y.; Mizukami, M.; Nagumo, S., Syntheses of Polycyclic Tetrahydrofurans by Cascade Reactions Consisting of Five-Membered Ring Selective Prins Cyclization and Friedel–Crafts Cyclization. *J. Org. Chem.* **2018,** *83* (16), 9103-9118.
70. Barakov, R.; Shcherban, N.; Yaremov, P.; Bezverkhyy, I.; Čejka, J.; Opanasenko, M., Hierarchical Beta zeolites as catalysts in a one-pot three-component cascade Prins–Friedel–Crafts reaction. *Green Chem.* **2020,** *22* (20), 6992-7002.
71. Prins, H. J., Prins reaction. *Chem. Weekblad* **1919,** *16*, 1072-1073.
72. Han, X.; Peh, G.; Floreancig, P. E., Prins-Type Cyclization Reactions in Natural Product Synthesis. *Eur. J. Org. Chem.* **2013,** *2013* (7), 1193-1208.
73. Friedel, C.; Crafts, J. M., PFC reaction *Compt. Rend.* **1877,** *84*, 1392– 1395.
74. Barakov, R.; Shcherban, N.; Petrov, O.; Lang, J.; Shamzhy, M.; Opanasenko, M.; Čejka, J., MWW-type zeolite nanostructures for a one-pot three-component Prins–Friedel–Crafts reaction. *Inorg. Chem. Front.* **2022,** *9* (6), 1244-1257.
75. Yadav, J. S.; Subba Reddy, B. V.; Ramesh, K.; Narayana Kumar, G. G. K. S.; Grée, R., A novel aza-Prins-Friedel–Crafts reaction for the synthesis of 4-arylpiperidines. *Tetrahedron Lett.* **2010,** *51* (5), 818-821.
76. Yang, X.-F.; Wang, M.; Zhang, Y.; Li, C.-J., 2,4-Diaryltetrahydropyran Formation by the Prins Cyclization and Its Application towards the Synthesis of Epicalyxin F and Calyxin I. *Synlett* **2005,** *2005* (12), 1912-1916.

77. Zheng, K.; Liu, X.; Qin, S.; Xie, M.; Lin, L.; Hu, C.; Feng, X., Completely OH-Selective FeCl3-Catalyzed Prins Cyclization: Highly Stereoselective Synthesis of 4-OH-Tetrahydropyrans. *J. Am. Chem. Soc.* **2012,** *134* (42), 17564-17573.
78. Reddy, B. V. S.; Borkar, P.; Yadav, J. S.; Sridhar, B.; Grée, R., Tandem Prins/Friedel–Crafts Cyclization for Stereoselective Synthesis of Heterotricyclic Systems. *J. Org. Chem.* **2011,** *76* (19), 7677-7690.
79. Subba Reddy, B. V.; Chaya, D. N.; Yadav, J. S.; Chatterjee, D.; Kunwar, A. C., BF3·OEt2-catalyzed tandem Prins Friedel–Crafts reaction: a novel synthesis of sugar fused diarylhexahydro-2H-furo[3,2-b]pyrans. *Tetrahedron Lett.* **2011,** *52* (23), 2961-2964.
80. Indukuri, K.; Bondalapati, S.; Kotipalli, T.; Gogoi, P.; Saikia, A. K., Stereoselective, One-Pot, Three-Component Synthesis of 4-Aryltetrahydropyrans from Epoxides via Prins Cyclization Reaction. *Synlett* **2012,** *2012* (02), 233-238.
81. Ghosh, A. K.; Keyes, C.; Veitschegger, A. M., FeCl3-catalyzed tandem Prins and Friedel–Crafts cyclization: a highly diastereoselective route to polycyclic ring structures. *Tetrahedron Lett.* **2014,** *55* (30), 4251-4254.
82. Reddy, B. V. S.; Reddy, G. N.; Reddy, M. R.; Lakshmi, J. K.; Jagadeesh, B.; Sridhar, B., Prins-Driven Friedel–Crafts Reaction for the Stereoselective Synthesis of Hexahydroindeno[2,1-c]pyran Derivatives. *Asian J. Org. Chem.* **2015,** *4* (11), 1266-1272.
83. Dintzner, M. R.; Maresh, J. J.; Kinzie, C. R.; Arena, A. F.; Speltz, T., A Research-Based Undergraduate Organic Laboratory Project: Investigation of a One-Pot, Multicomponent, Environmentally Friendly Prins–Friedel–Crafts-Type Reaction. *J. Chem. Educ.* **2012,** *89* (2), 265-267.
84. Dintzner, M. R., Montmorillonite K10 Clay Catalyzed Synthesis of 4-Aryltetrahydropyrans: A One-Pot, Multicomponent, Environmentally Friendly Prins–Friedel–Crafts-Type Reaction. *Synlett* **2013,** *24* (09), 1091-1092.
85. Zhou, Y.; Mu, Y.; Hsieh, M.-F.; Kabius, B.; Pacheco, C.; Bator, C.; Rioux, R. M.; Rimer, J. D., Enhanced Surface Activity of MWW Zeolite Nanosheets Prepared via a One-Step Synthesis. *J. Am. Chem. Soc.* **2020,** *142* (18), 8211-8222.
86. Baerlocher, C.; McCusker, L. B.; Meier, W. M.; Olson, D. H. IZA Synthesis Commission. http://www.iza-online.org/synthesis/default.htm.
87. Jo, C.; Cho, K.; Kim, J.; Ryoo, R., MFI zeolite nanosponges possessing uniform mesopores generated by bulk crystal seeding in the hierarchical surfactant-directed synthesis. *Chem. Commun. (Cambridge, U. K.)* **2014,** *50* (32), 4175-4177.
88. Gamliel, D. P.; Cho, H. J.; Fan, W.; Valla, J. A., On the effectiveness of tailored mesoporous MFI zeolites for biomass catalytic fast pyrolysis. *Appl. Catal. A, Gen.* **2016,** *522* (C), 109-119.
89. Sing, K., The use of nitrogen adsorption for the characterisation of porous materials. *Colloids Surf. A: Physicochem. Eng. Asp.* **2001,** *187-188*, 3-9.
90. Galarneau, A.; Villemot, F.; Rodriguez, J.; Fajula, F.; Coasne, B., Validity of the t-plot Method to Assess Microporosity in Hierarchical Micro/Mesoporous Materials. *Langmuir* **2014,** *30* (44), 13266-13274.
91. Góra-Marek, K.; Tarach, K.; Choi, M., 2,6-Di-tert-butylpyridine Sorption Approach to Quantify the External Acidity in Hierarchical Zeolites. *J. Phys. Chem. C* **2014,** *118* (23), 12266-12274.
92. Emeis, C. A., Determination of Integrated Molar Extinction Coefficients for Infrared Absorption Bands of Pyridine Adsorbed on Solid Acid Catalysts. *J. Catal.* **1993,** *141* (2), 347-354.
93. Muniz, F. T. L.; Miranda, M. A. R.; Morilla dos Santos, C.; Sasaki, J. M., The Scherrer equation and the dynamical theory of X-ray diffraction. *Acta Crystallogr. A* **2016,** *72* (3), 385-390.